NASA CONTRACTOR REPORT

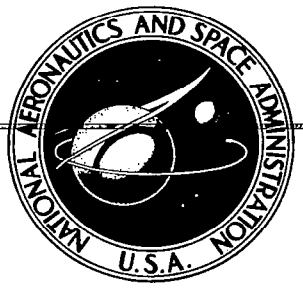

NASA CR-2908

FINITE ELEMENT ANALYSIS OF LOW SPEED VISCOUS AND INVISCID AERODYNAMIC FLOWS

A. J. Baker and P. D. Manhardt

Prepared by
COMPUTATIONAL MECHANICS CONSULTANTS, INC.
Knoxville, Tenn. 37920
for Langley Research Center

NATIONAL AERONAUTICS AND SPACE ADMINISTRATION • WASHINGTON, D. C. • OCTOBER 1977

1. Report No.	2. Government Accession No.	3. Recipient's Catalog No.
NASA CR- 2908		

4. Title and Subtitle	5. Report Date
Finite Element Analysis of Low Speed Viscous and Inviscid Aerodynamic Flows	October 1977
	6. Performing Organization Code

7. Author(s)	8. Performing Organization Report No.
A.J. Baker and P.D. Manhardt	CoMoC 77TR-2

9. Performing Organization Name and Address	10. Work Unit No.
Computational Mechanics Consultants, Inc. 3601A Chapman Highway Knoxville, TN 37920	11. Contract or Grant No. NAS1-14024 & 14307

12. Sponsoring Agency Name and Address	13. Type of Report and Period Covered
National Aeronautics & Space Administration Washington, D.C. 20546	Contractor Report
	14. Sponsoring Agency Code

15. Supplementary Notes

Langley Technical Monitor: Harry L. Morgan, Jr.
Final Report

16. Abstract

A weak-interaction solution algorithm is established for aerodynamic flow about an isolated airfoil. Finite element numerical methodology is applied to solution of each of differential equations governing potential flow, and viscous and turbulent boundary layer and wake flow downstream of the sharp trailing edge. The algorithm accounts for computed viscous displacement effects on the potential flow. These in turn alter the viscous flow through imposed pressure gradients. Closure for turbulence is accomplished using both first and second order models. The COMOC finite element fluid mechanics computer program was modified to solve the identified equation systems for two-dimensional flows. A numerical program was completed to determine factors affecting solution accuracy, convergence and stability for the combined potential, boundary layer, and parabolic Navier-Stokes equation systems. Good accuracy and convergence are demonstrated. Each solution is obtained within the identical finite element framework of COMOC.

17. Key Words (Selected by Author(s))	18. Distribution Statement
Aerodynamics Turbulent Flow Finite Element Method Numerical Solution	Unclassified - Unlimited Subject Category 02

19. Security Classif. (of this report)	20. Security Classif. (of this page)	21. No. of Pages	22. Price*
Unclassified	Unclassified	89	$5.00

* For sale by the National Technical Information Service, Springfield, Virginia 22161

TABLE OF CONTENTS

ILLUSTRATIONS

ILLUSTRATIONS (Continued)

TABLES

FINITE ELEMENT ANALYSIS OF LOW SPEED VISCOUS AND INVISCID AERODYNAMIC FLOWS

By

A.J. Baker and P.D. Manhardt

Computational Mechanics Consultants

Knoxville, TN 37920

SUMMARY

A weak-interaction solution algorithm is established for predicting aerodynamic flow about isolated elementary airfoils. The procedure employs finite element numerical methodology applied to solution of the partial differential equations governing isentropic potential flow, and the viscous and turbulent boundary layer and wake flows downstream of the sharp trailing edge, Iteration within the algorithm accounts for computed viscous displacement effects on the potential flow, the modifications to which in turn alter the viscous flow computations through imposed freestream pressure gradients. Closure for turbulence phenomena is accomplished using both first and second order models.

The COMOC finite element fluid mechanics computer program was modified to sequentially solve the identified equation systems for two-dimensional flows. A comprehensive numerical experimentation program was completed to determine factors affecting solution accuracy, convergence and stability for the combined potential, boundary layer, and parabolic Navier-Stokes equation systems. Good accuracy and convergence are demonstrated for potential flow prediction, including angle of attack and a curved wake trajectory. An economically accurate discretization procedure is identified for turbulent boundary layer computations which provides adequate sub-layer definition coupled with good solution speed. The parabolic Navier-Stokes equations, with turbulence kinetic energy closure are shown to accurately predict near-wake turbulent mixing processes for dissimilar turbulent boundary layer merging downstream of the trailing edge. Each of these solutions is obtained within the identical finite element framework of COMOC. In combination, with iteration through a sequential solution, the algorithm can establish an accurate and stable procedure for analytical characterization of complete flowfields about practical elementary airfoil configurations. The results of this evaluation, which document existence of a potentially viable supplement to wind tunnel testing, are presented in this report.

INTRODUCTION

Aerodynamics is a unique branch within engineering fluid mechanics. Elsewhere, the non-linearity introduced by the convective acceleration term in the Euler or Navier-Stokes equations precludes closed-form solutions in all but the most elementary cases. In aerodynamics however, for all low Mach number flight and slender bodies up to transonic Mach number, the differential equation governing isentropic flows is the familiar linear elliptic Laplacian. As a result, potential flow aerodynamics developed rapidly and became a classic study in engineering mechanics (cf., ref. 1). Concurrently, it was equally well recognized that potential flow analysis is only a first approximation, with the major limitation being primarily neglect of viscous and wake effects. Furthermore, accurate determinations for high performance lift systems, including leading edge slats and trailing edge slotted flaps, is well beyond the elementary analysis, with the result that the wind tunnel has been universally employed to accomplish design optimization.

The advent and ready accessibility of the large scale digital computer in the mid-1960's, and the phenomenal growth in its operating capabilities since then, initiated an entirely new approach to aerodynamics analysis. While the "computational wind tunnel" may still be a distant vision (cf., ref. 2), the use of numerical solution of the governing differential equations has emerged as a viable alternative to exhaustive experimentation in some cases. For example, a broad class in potential flow is now amenable to solution using numerical techniques to evaluate the singularity distributions imbedded within the Green's function analytical solution of the governing Laplacian equation. Specific elementary flow singularity functions, e.g., source, sink, vortex, doublet, etc., are combined to mathematically model thickness, lift, and the flow tangency boundary condition. Hess and Smith were among the pioneers in the development of the concept and its early reduction to practice (e.g., ref. 3). Refinements have extended applicability to supersonic flight as well. The proceedings of two recent conferences, held at NASA Langley Research Center (ref. 4,5), document the tremendous growth in this area and the versatility and utility of the concept.

However, as mentioned, potential flow determination is only a first approximation to the solution and must be corrected for viscous effects. The concept of the weak-interaction solution algorithm assumes that viscous (and turbulent) flow effects can be included by determination and use of an"effective" inviscid shape. These corrections are established by determination of the boundary layer character, and everywhere augmenting the airfoil thickness by the computed distribution of boundary layer displacement thickness. The elementary integral form of the boundary layer equation is typically utilized (ref. 6), with an experimental correlation function for shape factor. This concept has proven quite useful for elementary two-dimensional airfoils at modest angles of attack, and has been extended to analysis of high lift subsonic airfoil systems including an accounting for merged slot flows (ref. 7). However, since the viscous flow methods are elementary, at best, there exists ample area for improvement of the accuracy of the analysis. In particular,

as noted by Morgan (ref. 4, p. 730), the state-of-the-art, viscous-augmented potential flow solutions are amenable to improvement in determination of profile drag from downstream wake characteristics, flow characteristics after boundary layer separation, and pressure corrections in slot areas between overlapping elements of multi-element airfoils. In each case, the improvement required is in the handling of the viscous flows associated with practical airfoil configurations. Equally important is improving the stability of the potential flow algorithm when viscous corrections are included in an iterative analysis.

The mission of the present study was to examine the viability of the finite element numerical solution technique applied to the differential equation systems governing weak-interaction theory in low speed aerodynamics. Initial impetus was provided by the observation that the finite element algorithm is equally applicable to the potential flow and the turbulent boundary layer and wake flow governing differential equations. Furthermore, since finite element methodology is very flexible regarding discretization non-uniformity and gradient boundary condition specification on arbitrarily oriented (curved) surfaces, it appeared intrinsicly well suited to the aerodynamics problem class. In particular, since the flow tangency boundary condition can be applied directly on the "effective" inviscid contour, including the wake contour predicted by a complete viscous and turbulent flow solution, it appeared that iterative stability should be acceptable within the limits of validity of weak-interaction theory.

The results of this study, as generated using the COMOC finite element computer program, are reported herein. Although ample results on numerical experimentation have been reported on finite element solution for linear potential flows (ref. 8,9), including airfoil configurations (ref. 10-15), a detailed analysis of the aerodynamic accuracy has not been documented. Factors affecting solution accuracy, including use of highly non-uniform computational meshes, and reduction of finite element results to equivalent pressure distributions, have been thoroughly evaluated. The capability to automatically generate required discretizations and efficiently cycle through angle of attack are now documented. Finite element solution of the attached viscous and turbulent flows and the wake flow downstream of a sharp trailing edge of an airfoil have not been previously reported. This combination constitutes the weak-interaction problem and is sketched in Figure 1. The complete viscous flow equations governing these additional regimes in aerodynamics are developed, including models for both elementary and higher-order closure for turbulence phenomena. Numerical solutions as generated by COMOC, document an acceptable accuracy attainable with a minimum fineness discretization that is highly non-uniform for both boundary layer and elementary wake flows. The combination of these solution capabilities, existent within a single general purpose computer program, is then indicated to provide a convergent weak-interaction solution algorithm for a representative isolated two-dimensional airfoil configuration.

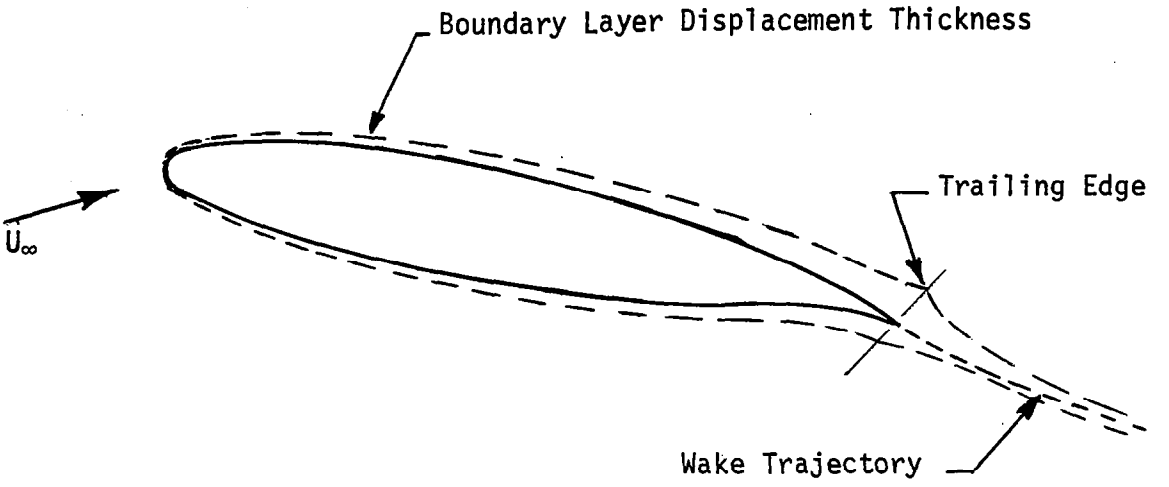

Fig. 1. Representation of the Weak-Interaction Solution Domain for Subsonic Flow

SYMBOLS

a	boundary condition coefficient
A	Van Driest damping function; constant
b	body force
c	isentropic sound speed
C	coefficient; chord
C_d	drag coefficient
C_f	skin friction coefficient
C_L	lift coefficient
d	differential
E	finite element solution energy
f	function of known argument
Fr	Froude Number

h	metric coefficient; mesh parameter
H	boundary layer shape factor
k	thermal conductivity; turbulence kinetic energy
K	generalized diffusion coefficient
ℓ	differential operator; length scale
L	differential operator; length
m	finite element index
M	Mach number; number of finite elements spanning R
n	unit normal vector; nodes per element; dimensionality
p	pressure; generalized parameter; convergence parameter
Pr	Prandtl number
q	generalized dependent variable
Q	generalized discretized dependent variable
R	universal gas constant; domain of elliptic differential operator
Re	Reynolds number
s	coordinate tangent to curve
S	finite element assembly operator
t	time
T	temperature
u_i	velocity vector
u,U	reference velocity
u_τ	friction velocity
v,V	scale velocity
W	molecular weight
x_i	Cartesian coordinate system

$y+$	friction velocity Reynolds number
α	angle of attack; parameter
γ	ratio of specific heats
Γ	circulation
∂R	closure of solution domain R
δ	Kronecker delta; boundary layer thickness
δ^*	boundary layer displacement thickness
Δ	increment
ε	turbulence dissipation function; thickness
θ	boundary layer momentum thickness
η	transformed coordinate
ξ	transformed coordinate
κ	Karman coefficient (MLT)
λ	multiplier; turbulence sublayer constant;
μ	dynamic viscosity
ν	kinematic viscosity
ρ	density
σ_{ij}	mean flow Stokes stress tensor
τ	Reynolds stress tensor; wall shear; integration kernel
ϕ	perturbation potential function; finite element functional
Φ	total potential function;
χ	generalized initial-value coordinate
ω	turbulence damping factor
Ω	global solution domain

Superscripts:

e	effective value
T	matrix transpose
+	turbulence correlation function
~	mass-weighted time-average
___	time averaged
^	unit vector
′	mass-weighted fluctuating component; ordinary derivative
*	approximation

Subscripts:

∞	global reference condition
e	freestream reference condition
i,j,k,ℓ	tensor indices
-	non-tensor index
m	finite element domain
n	normal
o	initial condition; stagnation reference
t	time derivative; turbulent; tangential
w	wall reference condition

Notation:

{ }	column matrix
[ ]	square matrix
∪	union
∩	intersection
ε	belongs to

THE FIELD EQUATIONS IN AERODYNAMICS

The description of a state point in multi-dimensional aerodynamics is contained within the solution of a coupled nonlinear partial differential equation system describing conservation of mass, momentum, and energy. Unique solutions are obtained upon closure of the system by specification of constitutive behavior and boundary conditions. In Cartesian tensor notation, the conservation form of the governing Navier-Stokes equation system is

$$L(\rho) = \frac{\partial \rho}{\partial t} + \frac{\partial}{\partial x_j}(\rho u_j) = 0 \tag{1}$$

$$L(\rho u_j) = \frac{\partial}{\partial t}(\rho u_j) + \frac{\partial}{\partial x_j}\left[\rho u_i u_j + p\delta_{ij} - \sigma_{ij}\right] + \rho b_i = 0 \tag{2}$$

$$L(\rho H) = \frac{\partial}{\partial t}(\rho H) + \frac{\partial}{\partial x_j}\left[\rho u_j H - \sigma_{ij} u_i + q_j\right] - \frac{\partial p}{\partial t} = 0 \tag{3}$$

The dependent variables in equations (1)-(3) have their usual interpretation in fluid mechanics where ρ is mass density, u_j is the velocity vector, p is the static pressure, b is the applicable body force, and H is the stagnation enthalpy. For a single species fluid,

$$H \equiv \int c_p dT + \frac{1}{2} u_j u_j \tag{4}$$

where c_p is specific heat and T is static temperature. Furthermore, q_j is the heat flux vector and σ_{ij} is the Stokes stress tensor, defined as

$$q_j \equiv -k \frac{\partial T}{\partial x_j} \tag{5}$$

$$\sigma_{ij} \equiv \mu\left[\frac{\partial u_i}{\partial x_j} + \frac{\partial u_j}{\partial x_i}\right] - \frac{2\mu}{3}\frac{\partial u_k}{\partial x_k}\delta_{ij} \tag{6}$$

In equations (5)-(6), k is the thermal conductivity and μ is the dynamic viscosity. An equation of state closes the definition; for example, for a perfect gas

$$p = \rho R W^{-1} T \tag{7}$$

where R is the universal gas constant and W is the molecular weight.

The important non-dimensional parameters in aerodynamics are:

$$\text{Reynolds Number:} \quad Re \equiv \frac{\rho_\infty U_\infty \ell}{\mu_\infty} \tag{8}$$

$$\text{Prandtl Number:} \quad Pr \equiv \frac{c_p \mu}{k} \tag{9}$$

$$\text{Mach Number:} \quad M_\infty \equiv \frac{U_\infty}{c} \tag{10}$$

$$\text{Froude Number:} \quad Fr \equiv \frac{U_\infty^2}{g\ell} \tag{11}$$

In equations (8) and (11), ℓ is a scale length of the problem and c is the isentropic sound speed. In non-dimensional form, the Navier-Stokes system becomes

$$L(\rho) \equiv \frac{\partial \rho}{\partial t} + \frac{\partial}{\partial x_j}(\rho u_j) = 0 \tag{12}$$

$$L(\rho u_i) \equiv \frac{\partial}{\partial t}(\rho u_i) + \frac{\partial}{\partial x_j}\left[\rho u_j u_i + p\delta_{ij} - Re^{-1}\sigma_{ij}\right] + Fr^{-1}\rho b_i = 0 \tag{13}$$

$$L(\rho H) \equiv \frac{\partial}{\partial t}(\rho H) + \frac{\partial}{\partial x_j}\left[\rho u_j H - (\gamma - 1)M_\infty^2 Re^{-1}\sigma_{ij}u_i - Re^{-1}Pr^{-1}\mu\frac{\partial H}{\partial x_j}\right] - (\gamma - 1)M_\infty^2\frac{\partial p}{\partial t} = 0 \tag{14}$$

Equations (12)-(14) form the basic system governing all classes of aerodynamic flows. Their straightforward solution represents a formidable task, and is not required for many flows of practical interest. The primary requirement is to determine the pressure distribution produced by flow about an aerodymanic shape, and to evaluate the resultant induced pressure and viscous drag forces. The concept of weak-interaction assumes existence of a convergent iteration procedure between a potential flow determination about the effective inviscid airfoil shape, and a viscous and turbulent flow solution in the immediate vicinity of the airfoil and in the wake. The weak-interaction hypothesis is usefully valid at modest angles of attack, wherein the viscous flow is parabolic, i.e., the governing equations obey a generalized boundary layer order-of-magnitude simplification. In this instance, the inviscid solution pressure distribution can be applied unaltered to the viscous flow solution. In turn, the displacement surface shape of the latter determines

the effective inviscid airfoil contour, and thus modifies the computed inviscid pressure distribution. For these flows, the iteration between inviscid and viscous flows should converge to a unique solution. The remainder of this section develops the various required governing differential equation systems including closure for turbulence.

Aerodynamic Potential Flow

The Navier-Stokes equations (12)-(14) are simplified to describe the steady, isentopic irrotational flow of an inviscid fluid. The Stokes stress tensor σ_{ij} vanishes identically, and H equal to a constant is the solution to equation (14). The potential flow description is then

$$L(\rho) = \frac{\partial}{\partial x_j}(\rho u_j) = 0 \tag{15}$$

$$L(\rho u_j) = \frac{\partial}{\partial x_j}\left[\rho u_i u_j + p\delta_{ij}\right] = 0 \tag{16}$$

These (four) equations can be usefully combined into a single equation using the definition of isentropic sound speed

$$c^2 \equiv \left(\frac{\partial p}{\partial \rho}\right)_s \tag{17}$$

Expanding equation (15) and replacing the resultant density derivative with equation (17) yields

$$L(u_j) = \left[\delta_{ij} - c^{-2} u_i u_j\right] \frac{\partial u_j}{\partial x_i} = 0 \tag{18}$$

For isoenergetic flow, where subscript zero indicates the stagnation reference state

$$c^2 = c_0^2 - \frac{\gamma - 1}{2} u_j u_j \tag{19}$$

Equation (18) is a highly non-linear, first-order partial differential equation valid for all Mach numbers. As a function of M, it can display elliptic, parabolic and/or hyperbolic differential character. The class of interest corresponds to an irrotational (or rotation preserving) velocity field. Since the curl thus vanishes to within an arbitrary constant

$$u_j \equiv -\frac{\partial \Phi}{\partial x_j} \tag{20}$$

where Φ is termed the velocity (total) potential function. By direct substitution, equation (18) becomes

$$L(\Phi) = \left[\delta_{ij} - c^{-2}\frac{\partial \Phi}{\partial x_i}\frac{\partial \Phi}{\partial x_j}\right]\frac{\partial^2 \Phi}{\partial x_i \partial x_j} = 0 \tag{21}$$

Equation (21), a second-order partial differential equation, preserves the mixed differential character cited previously. For subsonic flow at small Mach number, equation (21) simplifies to the elementary linear Laplacian

$$L(\Phi) \approx \frac{\partial^2 \Phi}{\partial x_i \partial x_i} = 0 \tag{22}$$

Boundary condition specification for equations (21) and (22) requires enforcement of flow tangency to given coordinate surfaces. Assuming $\hat{n}_j$ the unit outward pointing surface normal vector, this boundary constraint becomes (from equation (20))

$$u_j \hat{n}_j \equiv U_n = \frac{\partial \Phi}{\partial x_j}\hat{n}_j \tag{23}$$

Note that U_n vanishing identically enforces flow tangency. In the instance of small Mach number equations (22)-(23) represent the classic von Neumann specification for an elliptic differential equation. A unique solution is obtained by setting Φ equal to an arbitrary constant at one point in space.

While total potential has been evaluated in finite element literature, the alternative perturbation function definition is common to aerodynamics and has been determined preferable for the finite element approach as well. Herein, the velocity field is referenced to the undisturbed freestream as

$$u_j \equiv U_\infty\left[\hat{\varepsilon}_j - \frac{\partial \phi}{\partial x_j}\right] \tag{24}$$

where $\hat{\varepsilon}_j$ is the freestream flow unit vector related in an elementary manner to angle of attack. Substituting equation (24) into (18) and dividing by the freestream sound speed

$$L(\phi) \equiv \left[\delta_{ij} - M_\infty^2 \hat{\varepsilon}_i \hat{\varepsilon}_j + (\gamma - 1)M_\infty^2 \delta_{ij}\left(\hat{\varepsilon}_k \frac{\partial \phi}{\partial x_k} - \frac{1}{2}\frac{\partial \phi}{\partial x_k}\frac{\partial \phi}{\partial x_k}\right)\right.$$
$$\left. + M_\infty^2\left(\hat{\varepsilon}_i \frac{\partial \phi}{\partial x_j} + \hat{\varepsilon}_j \frac{\partial \phi}{\partial x_i} - \frac{\partial \phi}{\partial x_i}\frac{\partial \phi}{\partial x_j}\right)\right]\frac{\partial^2 \phi}{\partial x_i \partial x_j} = 0 \tag{25}$$

Equation (19) has been referenced to freestream.

$$c^2 = c_\infty^2 + \frac{(\gamma - 1)}{2} U_\infty^2 \left[2\hat{\varepsilon}_j \frac{\partial \phi}{\partial x_j} - \frac{\partial \phi}{\partial x_j} \frac{\partial \phi}{\partial x_j} \right] \tag{26}$$

Sufficiently remote from the airfoil, since $u_j = U_\infty \hat{\varepsilon}_j$, the appropriate freestream boundary condition is ϕ a constant. However, the Kutta condition for angle of attack modifies the interpretation to allow a jump in ϕ across the wake trajectory. Hence, the farfield constraint valid for all cases is

$$\frac{\partial \phi}{\partial x_i} \hat{n}_i = 0 \tag{27}$$

where $\hat{n}_i$ is the outward-pointing unit normal vector. At the effective inviscid-flow surface of the airfoil, since $u_j \hat{n}_j$ vanishes identically, the boundary condition on ϕ is

$$\frac{\partial \phi}{\partial x_j} \hat{n}_j = \hat{\varepsilon}_j \hat{n}_j \tag{28}$$

Hence, angle of attack and local airfoil contour (unit normal) are applied directly as a boundary condition.

Equations (25)-(28) are valid for all Mach number and display the mixed differential behavior. The slender body approximation can significantly simplify equation (25) by the neglect of all products in perturbation velocity and the assumption that $\hat{\varepsilon}_j$ is aligned with a principal coordinate, say x_1 i.e.,

$$\hat{\varepsilon}_j = \delta_{j1} \tag{29}$$

Equation (25) then takes the form

$$\begin{aligned} L(\phi) \approx & \left[\delta_{ij} - M_\infty^2 \delta_{i1} \delta_{j1} + (\gamma - 1) M_\infty^2 \frac{\partial \phi}{\partial x_1} \delta_{ij} \right. \\ & \left. + M_\infty^2 \left(\delta_{i1} \frac{\partial \phi}{\partial x_j} + \delta_{j1} \frac{\partial \phi}{\partial x_i} \right) \right] \frac{\partial^2 \phi}{\partial x_i \partial x_j} = 0 \end{aligned} \tag{30}$$

In expanded form for two-dimensional flow, equation (30) is

$$\begin{aligned} L(\phi) \approx & \left[1 - M_\infty^2 + (\gamma + 1) M_\infty^2 \frac{\partial \phi}{\partial x_1} \right] \frac{\partial^2 \phi}{\partial x_1^2} \\ & + 2 M_\infty^2 \frac{\partial \phi}{\partial x_2} \frac{\partial^2 \phi}{\partial x_1 \partial x_2} + \left[1 + (\gamma - 1) M_\infty^2 \frac{\partial \phi}{\partial x_1} \right] \frac{\partial^2 \phi}{\partial x_2^2} = 0 \end{aligned} \tag{31}$$

which is recognized as the complete small disturbance equation (cf., ref. 16). For most flow velocities below transonic, equation (30) or (31) can be linearized by retention of only $(1-M_\infty^2)$ on the lead term. The Prandtl-Glauert (ref. 1) coordinate transformation can then be employed to eliminate explicit appearance of M_∞. Hence, for all subsonic flows about slender bodies equation (30) becomes the Laplacian, i.e.,

$$L(\phi) \approx \frac{\partial^2 \phi}{\partial x_i \partial x_i} = 0 \tag{32}$$

As mentioned, the desired output from the potential flow solution is the pressure distribution over the effective airfoil surface and onto the viscous trailing edge wake. The pressure coefficient is

$$C_p \equiv 1 - \frac{\rho u_i u_i}{\rho_\infty U_\infty^2} \tag{33}$$

Substituting equation (24) yields

$$C_p = 2\frac{\partial \phi}{\partial x_j}\hat{\varepsilon}_j - \frac{\partial \phi}{\partial x_j}\frac{\partial \phi}{\partial x_j} \tag{34}$$

Evaluation of equation (34) is facilitated by resolution of the vector field into scalar components locally parallel and perpendicular to the effective airfoil surface. Letting $\hat{t}_j$ denote the unit tangent vector, and (n,s) the corresponding surface-oriented coordinate system,

$$\begin{aligned} \frac{\partial \phi}{\partial x_j} &= \frac{\partial \phi}{\partial n}\hat{n}_j + \frac{\partial \phi}{\partial s}\hat{t}_j \\ &= (\hat{\varepsilon}_k \hat{n}_k)\hat{n}_j + \frac{\partial \phi}{\partial s}\hat{t}_j \end{aligned} \tag{35}$$

The last form was obtained using equation (28). Substituting equation (35) into (34) yields

$$C_p = (\hat{\varepsilon}_j \hat{n}_j)^2 + 2\frac{\partial \phi}{\partial s}\hat{\varepsilon}_j \hat{t}_j - \frac{\partial \phi}{\partial s}\frac{\partial \phi}{\partial s} \tag{36}$$

Recall that $\hat{\varepsilon}_j$ is the constant unit vector for U_∞; the remaining terms in equation (26) are all a function of the surface coordinate s.

The decomposition in equation (35) has yielded C_p in a form directly dependent upon airfoil geometry. Hence, $\hat{n}_j$ and $\hat{t}_j$ are potentially available to any required degree of accuracy. As will evolve, the finite element solution for distribution of $\phi(s)$ is a direct computational result for the zero normal wash boundary condition equation (28). Only these surface values are required to evaluate equation (36), using for example, spline interpolation techniques to establish the required tangent slope distribution.

Aerodynamic Viscous Flows

The complete Navier-Stokes system equations (12)-(14), is required to adequately describe general viscous flowfields including regions of recirculation. For small angle of attack, such that the viscous flow remains attached to the airfoil surface, the considerable simplication of boundary layer theory (e.g., ref. **6**) is appropriate. These equations in general are an insufficient description for the viscous wake flow downstream of the trailing edge terminus however, wherein the parabolic Navier-Stokes equations are required (at least). The boundary layer equations are a sub-set of the parabolic system, the establishment of which is readily accomplished.

The three-dimensional "parabolic Navier-Stokes" (3DPNS) equations describe the steady time-averaged confined or unbounded viscous and turbulent flow of a compressible, nonisoenergetic fluid wherein:

(1) A predominant mean flow direction is uniformly discernible,

(2) In this direction (only) diffusion processes are negligible compared to convection, and,

(3) No significant flowfield disturbances are propagated upstream against the predominant flow direction.

To establish the system, assume the Reynolds decomposition of the instantaneous velocity vector u_i , equation (2), into a steady mean flow $\tilde{u}_i$ and velocity fluctuations u_i' as (cf., ref. 17)

$$u_i = \tilde{u}_i + u_i' \tag{37}$$

In equation (37), $\tilde{u}_i$ is interpreted as the mass-weighted, time-averaged steady flow, i.e.,

$$\tilde{u}_i \equiv \frac{\overline{\rho u_i}}{\bar{\rho}} \tag{38}$$

By definition, using the overbar to denote time-averaging,

$$\overline{\rho u_i'} = \lim_{T\to\infty} \frac{1}{T}\int_{t_o}^{t_o+T} (\rho u_i - \bar{\rho}\tilde{u}_i)dt = 0 \tag{39}$$

The concept of time-averaging yields the important relation

$$\overline{\rho u_i u_j} = \bar{\rho}\tilde{u}_i\tilde{u}_j + \overline{\rho u_i' u_j'} \tag{40}$$

For the isoenergetic steady flows of present interest, the time-averaged Navier-Stokes equations for the mean flow become

$$L(\bar{\rho}) = \frac{\partial(\bar{\rho}\tilde{u}_i)}{\partial x_i} = 0 \tag{41}$$

$$L(\bar{\rho}\tilde{u}_i) = \bar{\rho}\tilde{u}_j\frac{\partial\tilde{u}_i}{\partial x_j} + \frac{\partial\bar{p}}{\partial x_i} - \frac{\partial}{\partial x_j}\left[\bar{\sigma}_{ij} - \overline{\rho u_i' u_j'}\right] = 0 \tag{42}$$

In equation (42), $\bar{\sigma}_{ij}$ is the time-averaged mean flow Stokes stress tensor, equation (6). The second term in the divergence is called the Reynolds stress tensor, τ_{ij}

$$\tau_{ij} \equiv -\overline{\rho u_i' u_j'} \tag{43}$$

The parabolic approximation to equations (41)-(42) constrains appropriate summation limits. Assuming the x_1 coordinate aligned with the direction of predominant flow, this approximation becomes

$$\bar{\sigma}_{ij} = \frac{\bar{\mu}}{Re}(1 - \delta_{j1})\left[\frac{\partial\tilde{u}_i}{\partial x_j} + \frac{\partial\tilde{u}_j}{\partial x_i} - \frac{2}{3}\frac{\partial\tilde{u}_k}{\partial x_k}\delta_{ij}\right] \tag{44}$$

The mean flow unidirectionality also affects retained scalar components of the Reynolds stress, to be developed. The subscript bar notation denotes the index is not eligible for the summation convention, but merely takes on the value of the synonynous tensor index. In expanded form the 3DPNS system is

$$L(\bar{\rho}) = \frac{\partial}{\partial x_1}(\bar{\rho}\tilde{u}_1) + \frac{\partial}{\partial x_2}(\bar{\rho}\tilde{u}_2) + \frac{\partial}{\partial x_3}(\bar{\rho}\tilde{u}_3) = 0 \tag{45}$$

$$
\begin{aligned}
L(\rho\tilde{u}_i) = {} & \bar{\rho}\tilde{u}_1 \frac{\partial \tilde{u}_i}{\partial x_1} + \bar{\rho}\tilde{u}_2 \frac{\partial \tilde{u}_i}{\partial x_2} + \bar{\rho}\tilde{u}_3 \frac{\partial \tilde{u}_i}{\partial x_3} + \frac{\partial \bar{p}}{\partial x_i} \\
& - \frac{1}{Re}\left[\frac{\partial}{\partial x_2}\bar{\mu}\left(\frac{\partial \tilde{u}_i}{\partial x_2} + \frac{\partial \tilde{u}_2}{\partial x_i}\right) + \frac{\partial}{\partial x_3}\bar{\mu}\left(\frac{\partial \tilde{u}_i}{\partial x_3} + \frac{\partial \tilde{u}_3}{\partial x_i}\right)\right. \\
& \left. - \frac{2}{3}(1 - \delta_{i1})\frac{\partial}{\partial x_i}\left(\frac{\partial \tilde{u}_1}{\partial x_1} + \frac{\partial \tilde{u}_2}{\partial x_2} + \frac{\partial \tilde{u}_3}{\partial x_3}\right)\right] \\
& - \frac{\partial}{\partial x_1}\left[-\overline{\rho u_1' u_i'}\right] - \frac{\partial}{\partial x_2}\left[-\overline{\rho u_2' u_i'}\right] - \frac{\partial}{\partial x_3}\left[-\overline{\rho u_3' u_i'}\right] = 0
\end{aligned}
\tag{46}
$$

Note that equation (46) represents three scalar components. The two-dimensional system, i.e., 2DPNS, is obtained by deletion of all x_3 partial derivatives. The dependent variables of the 2D and 3DPNS equations are the steady-flow mean velocity vector $\tilde{u}_i$ and pressure $\bar{p}$. The presented system is not closed since the scalar components of the Reynolds stress tensor remain to be identified. This is accomplished in the following section.

Over the modest range of angle of attack in subsonic flow to which the present analysis is restricted, both the boundary layer and wake flow differential equation systems are subsets of the 3DPNS system. For the former, the first and third equations in (46) are solved for $\tilde{u}_1$ and $\tilde{u}_3$ respectively, as initial-boundary value statements. The mean velocity component normal to the surface, $\tilde{u}_2$ is determined from initial-value solution of equation (45) in terms of its prescribed value at the airfoil surface. Through an order of magnitude analysis (cf., Tennekes and Lumley, ref. 18), the $\tilde{u}_2$ momentum equation can be simplified to

$$
L(\bar{\rho}\tilde{u}_2) \approx \frac{\partial}{\partial x_2}\left[\bar{p} - \overline{\rho u_2' u_2'}\right] = 0 \tag{47}
$$

Therefore, pressure variation through the boundary layer remains a second-order phenomenon, and is linearly proportional to a scalar component of the turbulence kinetic energy. Hence, to first order, the inviscid pressure distribution determined from equation (36) is applied directly to solution of the viscous boundary layer flow. Equation (47) could be evaluated from freestream where the pressure is known to the airfoil surface to provide a second order correction. This same order of magnitude analysis identifies $-\overline{\rho u_i' u_\ell'}$, $2 \le \ell \le 3$, as the dominant components of the Reynolds stress tensor.

Determination of the viscous and turbulent flow in the wake downstream of the trailing edge using the boundary layer equations is inappropriate except for zero angle of attack and a symmetric airfoil with a cusped trailing edge. Solutions in the immediate vicinity of a blunt trailing edge would require the full Navier-Stokes equations. For a sharp trailing edge whereat

non-symmetric attached viscous-flows merge, the 2D or 3DPNS system can provide prediction of the ensuing wake. Guidance for the solution procedure comes from available boundary conditions; initial conditions for $\tilde{u}_i$ and $\bar{p}$ are provided by the individual boundary layer solutions at the trailing edge. Downstream, $\tilde{u}_1$, $\tilde{u}_3$ and $\bar{p}$ are known as a function of x_1 at both freestream boundaries of the wake flow. To first order and for an essentially straight trajectory, $\bar{p}$ is uniform across the entire wake. To the same order, from the continuity equation (45), the derivative of $\tilde{u}_2$ at each freestream boundary is equal to the downstream derivative of $\tilde{u}_1$. Therefore, solution for $\tilde{u}_2$ from its momentum equation (46), as a boundary value problem is required.

Therefore, for the cited restrictions, the developed 3DPNS differential equations (45)-(46) provide the required descriptions for the viscous aerodynamic flows of interest. It remains to close the system with a model for the Reynolds stress distribution.

Turbulence Closure and Modeling

The operation of time-averaging has introduced the Reynolds stress tensor, τ_{ij}, equation (43) into the 3DPNS equations. Using well established procedures, e.g., reference 17, the partial differential equation system governing the behavior of the Reynolds stress tensor can be derived. Assuming the cross-correlation of density fluctuations can be neglected, the exact partial differential equation governing the kinematic Reynolds stress tensor, $-\overline{u_i' u_j'}$, is (ref. 19)

$$
\begin{aligned}
L(u_i' u_j') \;=\; & \frac{\partial}{\partial x_k}\left(\tilde{u}_k \overline{u_i' u_j'}\right) + \left[\overline{u_j' u_k'}\,\frac{\partial \tilde{u}_i}{\partial x_k} + \overline{u_i' u_k'}\,\frac{\partial \tilde{u}_j}{\partial x_k}\right] \\
& + 2\nu\,\overline{\frac{\partial u_i'}{\partial x_k}\frac{\partial u_j'}{\partial x_k}} + \overline{\frac{p}{\rho}\left[\frac{\partial u_i'}{\partial x_j} + \frac{\partial u_j'}{\partial x_i}\right]} \\
& + \frac{\partial}{\partial x_k}\left[\overline{u_i' u_j' u_k'} - \nu\,\frac{\partial \overline{u_i' u_j'}}{\partial x_k} + \overline{\frac{p}{\rho}\left(\delta_{jk} u_i' + \delta_{ik} u_j'\right)}\right] = 0
\end{aligned}
\tag{48}
$$

An additional differential equation for turbulence dissipation rate, ε, is required; under the assumption the process is isotropic,

$$
2\nu\,\overline{\frac{\partial u_i'}{\partial x_k}\frac{\partial u_j'}{\partial x_k}} \equiv \frac{2}{3}\delta_{ij}\,\varepsilon \tag{49}
$$

The transport equation for dissipation function ε is (ref. 18)

$$L(\varepsilon) = \frac{\partial}{\partial x_k}(\tilde{u}_k \varepsilon) + 2\nu \overline{\frac{\partial u_i'}{\partial x_k} \frac{\partial u_i'}{\partial x_\ell} \frac{\partial u_k'}{\partial x_\ell}} + 2\overline{\left[\nu \frac{\partial^2 u_i'}{\partial x_k \partial x_\ell}\right]^2} \tag{50}$$

$$+ \frac{\partial}{\partial x_k}\left[\nu \overline{u_k' \frac{\partial u_i'}{\partial x_\ell} \frac{\partial u_i'}{\partial x_\ell}} + \overline{\frac{\nu}{\rho} \frac{\partial p}{\partial x_i} \frac{\partial u_k'}{\partial x_i}}\right] = 0 \quad .$$

Equations (48)-(50) represent seven additional partial differential equations describing turbulence transport phenomena. This system also is not closed, since the third order fluctuating velocity and pressure-velocity correlations remain undefined. While additional differential equations could be established, they in turn would involve fourth order terms. Hence, a modeling of third order correlations is typically invoked to close the presented system. This can be established at several levels of completeness, dependent upon dimensionality and geometrical complexity of the physical system.

Launder et.al., (ref.19) develop a closure in terms of all components of $-\overline{u_i' u_j'}$. They present results for several flow cases including isotropic turbulence, free shear flows, elementary duct flows and flat plate boundary layers. In earlier work, Hanjalic' and Launder (ref. 20) established a closure applicable to thin shear flows wherein one shear component, $-\overline{u_1' u_2'}$ of the Reynolds stress tensor is retained, and solved in combination with ε and the turbulence kinetic energy, k, defined as

$$k \equiv \frac{1}{2}\overline{u_i' u_i'} \tag{51}$$

The differential equation for k is established by contracting equation (48) with the Kronecker delta. For the shear dominated flows of interest, wherein $\tilde{u}_1 >> \tilde{u}_2$ and $\tilde{u}_1 >> \tilde{u}_3$,

$$L(k) = \frac{\partial}{\partial x_j}(\tilde{u}_j k) - C_k \frac{\partial}{\partial x_\ell}\left[k^2 \varepsilon^{-1} \frac{\partial k}{\partial x_\ell}\right]$$

$$- \overline{u_1' u_\ell'} \frac{\partial \tilde{u}_1}{\partial x_\ell} + \varepsilon = 0 \tag{52}$$

Equation (52) introduces the summation index convention $1 \leq i,j \leq 3$ and $2 \leq k,\ell \leq 3$. The corresponding form for dissipation function, equation (40) is

$$L(\varepsilon) = \frac{\partial}{\partial x_j}(\tilde{u}_j \varepsilon) - C_\varepsilon \frac{\partial}{\partial x_i}\left[k\,\varepsilon^{-1}\,\overline{u_i' u_j'}\,\frac{\partial \varepsilon}{\partial x_j}\right]$$

$$- C_\varepsilon^1 \overline{u_1' u_\ell'}\,\varepsilon\, k^{-1}\,\frac{\partial \tilde{u}_1}{\partial x_\ell} + C_\varepsilon^2 \varepsilon^2 k^{-1} = 0 \tag{53}$$

In equations (52)-(53), the various constants C_α are determined from approximate analyses and/or computer optimization (ref. 19).

The next level of simplification for turbulence closure involves specification of an effective kinematic turbulent diffusion coefficient, ν_t. From first principles (e.g., ref. 21), the form must be

$$\nu_t \equiv C\,V\,\ell \tag{54}$$

where C is a constant, V is a scale velocity and ℓ is a length. For the turbulence kinetic energy-dissipation function, two equation closure hypothesis (herein named TKE), V is taken as the square root of turbulence kinetic energy, equation (51). A dissipation length scale, ℓ_d, can be defined in terms of k and ε as (e.g., ref. 21).

$$\ell_d \equiv k^{3/2}\varepsilon^{-1} \tag{55}$$

The TKE closure then yields

$$\nu_t = C_\nu k^2 \varepsilon^{-1} \tag{56}$$

Note that this is precisely the diffusion coefficient for turbulent kinetic energy, equation (52). Furthermore, upon summing the diffusion terms in equation (53), using equation (51) and assuming isotropy, equation (56) also yields the diffusion coefficient for dissipation function.

To close the TKE system, it is required to model the correlation between the shear components of the Reynold's stress tensor and k, ε and the mean velocity field $\tilde{u}_i$. For two- and three-dimensional parabolic flows, the relation is typically of the form

$$-\overline{u_i' u_\ell'} \equiv C_{i\ell}\, k^2 \varepsilon^{-1}\left[\frac{\partial \tilde{u}_i}{\partial x_\ell} + \frac{\partial \tilde{u}_\ell}{\partial x_i}\right] \tag{57}$$

The subscript bar indicates the index is not eligible for summation. Under the assumption of isotropy, the elements of the correlation tensor $C_{i\ell}$ can be combined into C_ν , equation (56). For the unidirectional flows of interest, partial derivatives on x_2 dominate. Therefore, using equations (56)-(57), the final form of the two-equation TKE closure is

$$L(k) = \frac{\partial}{\partial x_j}(\tilde{u}_j k) - \frac{\partial}{\partial x_\ell}\left[\frac{\nu^e}{Pr_k}\frac{\partial k}{\partial x_\ell}\right] - \nu^e \frac{\partial \tilde{u}_1}{\partial x_\ell}\frac{\partial \tilde{u}_1}{\partial x_\ell} + \varepsilon = 0 \tag{58}$$

$$L(\varepsilon) = \frac{\partial}{\partial x_j}(\tilde{u}_j \varepsilon) - \frac{\partial}{\partial x_\ell}\left[\frac{\nu^e}{Pr_\varepsilon}\frac{\partial \varepsilon}{\partial x_\ell}\right] - C_\varepsilon^1 \varepsilon k^{-1} \nu^e \frac{\partial \tilde{u}_1}{\partial x_\ell}\frac{\partial \tilde{u}_1}{\partial x_\ell} + C_\varepsilon^2 \varepsilon^2 k^{-1} = 0 \tag{59}$$

In equations (58)-(59), for 3DPNS, the tensor indices range $1 \leq i,j \leq 3$ and $2 \leq \ell \leq 3$. For 2DPNS, correspondingly, $1 \leq i,j \leq 2$, $\ell = 2$ only. Hence, since $i = 1$ corresponds to the direction of predominant flow, diffusion is restricted to the plane transverse to the x_1 coordinate, as required by parabolic assumption (2). The various coefficients (C_k, C_ε , Pr_ε ,etc) have been determined from simplified analyses or computer optimization; recommended values for shear layer flows are given in Table 1 (e.g., ref.19, 21).

Table 1

Coefficients in TKE Closure Model

Variable	Equation No.	Coefficients
ν_t	(56)	$C_\nu = 0.09$
k	(58)	$Pr_k = 1.0$
ε	(59)	$Pr_\varepsilon = 1.3$, $C_\varepsilon^1 = 1.44$, $C_\varepsilon^2 = 1.92$

Boundary condition statements are required for the TKE equations, since they also represent initial-boundary value problems. In the freestream, the levels of k and ε must vanish by assumption of a non-turbulent free stream flow. Since validity of the Reynolds stress hypothesis is limited to regions where the turbulent Reynolds number is large, it is not feasible to enforce k and ε to vanish at a solid surface. The alternative is to express boundary conditions at some small distance from the aerodynamic surface. To accomplish this, Prandtl mixing length theory (MLT) can be employed adjacent to the aerodynamic surface to close the problem, in concert with the Van Driest damping function distribution (ref. 17). According to equation (54), the effective turbulent viscosity is determined by a velocity and length scale. MLT expresses the correlation in terms of the predominant mean flow gradient and a length scale ℓ (ref. 6).

$$\nu_t \equiv \omega^2 \ell^2 \left[\frac{\partial \tilde{u}_1}{\partial x_2}\right] \tag{60}$$

where ℓ is the mixing length

$$\ell \equiv \begin{cases} \kappa x_2 & 0 \le x_2 \le \lambda\delta\kappa^{-1} \\ \lambda\delta & x_2 > \lambda\delta\kappa^{-1} \end{cases} \tag{61}$$

The Van Driest damping function is defined as

$$\omega \equiv 1 - \exp(-x_2 A^{-1}) \tag{62}$$

In equation (61), x_2 is the coordinate normal to the surface, δ is the boundary layer thickness, and λ and k are constants (typically 0.09 and 0.435 respectively). In equation (62), A is a complex function of many factors influencing flow phenomena near the surface, including axial pressure gradient and normal mass flow. The form of Cebeci and Smith (ref. 17) serves to unify the many formulations as

$$A \equiv A^+ \nu N^{-1} \left(\frac{\tau_w}{\rho_w}\right)^{-\frac{1}{2}} \left(\frac{\rho}{\rho_w}\right)^{\frac{1}{2}} \tag{63}$$

where

$$N^2 \equiv \frac{\nu}{\nu_e}\left(\frac{\rho_e}{\rho_w}\right)^2 \frac{p^+}{v^+}\left[1 - \exp\left(11.8\frac{\nu_w}{\nu}v^+\right)\right] + \exp\left[11.8\left(\frac{\nu_w}{\nu}\right)v^+\right] \tag{64}$$

All variables are time-averaged steady components, subscripts e and w refer to freestream and wall values respectively, A^+ is a constant (25.3), τ_w is the skin friction. Pressure gradient and mass addition effects are accounted for accordingly as

$$p^+ \equiv \left[\frac{\nu_e \tilde{u}_{1e}}{\tilde{u}_\tau^3}\right] \frac{d\tilde{u}_{1e}}{dx_1} \tag{65}$$

$$v^+ \equiv u_\tau^{-1} V_w \tag{66}$$

where $\tilde{u}_{1e}$ is the freestream axial velocity, V_w is the specified velocity normal to the airfoil, if present, and u_τ is the shear velocity

$$u_\tau \equiv \left[\frac{\tau_w}{\rho}\right]^{\frac{1}{2}} \tag{67}$$

The shear stress τ_w is defined as

$$\tau_w \equiv \rho_w \nu_w \left.\frac{\partial \tilde{u}_1}{\partial x_2}\right|_w \tag{68}$$

It can be evaluated using a difference formulae from an empirical data-based equation, for example Patankar and Spalding (ref. 22), or for boundary layer-type flows, from the Ludwieg-Tillman formula (ref. 6). The latter form is

$$\tau_w = \frac{1}{2}\rho_e \tilde{u}_{1e}^2 \left[0.246(10)^{-0.678H} Re_\theta^{-0.268}\right] \tag{69}$$

where Re_θ is the Reynolds number based upon boundary layer momentum thickness and H is the boundary layer shape factor (e.g., ref. 6).

Equations (60)-(69) provide the formalisms necessary to determine boundary condition values for k and ε near the aerodynamic surface. Furthermore, through the dual definitions of turbulent effective viscosity, equations (56) and (60), and since the latter involves functions only of the mean axial velocity component $\tilde{u}_1$, which is either known or readily initialized, a means is established to initialize distributions of both k and ε at the node points of a discretization. Since the developed partial differential equations are initial value, this information is required to start a solution.

The closure for turbulence is now complete at the level of sophistication selected for these studies. The solutions of equations (58)-(59) provide closure for the 3DPNS equations (41)-(42) via equation (57). Define an effective diffusion coefficient as

$$\mu^e \equiv \frac{\bar{\mu}}{Re} + \bar{\rho}\nu_t \tag{70}$$

Then, using equations (70), (54) and (44), and neglecting fluid dilitation, the total stress tensor contribution for 3DPNS can be written as

$$\bar{\sigma}_{ij} - \overline{\rho u_i' u_j'} = \mu^e\left[1 - \delta_{j1}\right]\left[\frac{\partial \tilde{u}_i}{\partial x_j} + \frac{\partial \tilde{u}_j}{\partial x_i}\right] \tag{71}$$

Then, the 3DPNS system for isoenergetic flows equations (45)-(46) can be compactly written as

$$L(\bar{\rho}) = \frac{\partial}{\partial x_i}(\bar{\rho}\tilde{u}_i) = 0 \tag{72}$$

$$L(\rho\tilde{u}_i) = \bar{\rho}\tilde{u}_j\frac{\partial \tilde{u}_i}{\partial x_j} + \frac{\partial \bar{p}}{\partial x_i} - \frac{\partial}{\partial x_\ell}\left[\mu^e\left(\frac{\partial \tilde{u}_i}{\partial x_\ell} + \frac{\partial \tilde{u}_\ell}{\partial x_i}\right)\right] = 0 \tag{73}$$

where $1 \leq i,j \leq 3$ and $2 \leq \ell \leq 3$.

The viscous flowfield equation system is now complete as equations (58), (59), (72) and (73). This system must be solved in concert with the definition of the potential flow as obtained by solution of either equations (21), (25), (30) or (32). All boundary conditions have been identified for the representative solution domains. Appropriate initial-value character has been noted and means proposed to initialize required distributions in terms of readily available information or data. The system thus developed appears complete. It now remains to establish the numerical solution algorithm for these equation systems.

FINITE ELEMENT SOLUTION ALGORITHM

The desired forms of the partial differential equation systems governing subsonic aerodynamic flows of interest have been presented. Each member of the system is a special case of the general, second-order non-linear elliptic boundary value partial differential equation

$$L(q) = \frac{\partial}{\partial x_\ell}\left[K\frac{\partial q}{\partial x_\ell}\right] + f_1\left(q, \frac{\partial q}{\partial x_\ell}, p, x_i\right) + f_2\left(\tilde{u}_1, \frac{\partial q}{\partial x_1}\right) = 0 \tag{74}$$

Herein, q is the generalized dependent variable, the tensor indices range $2 \leq k, \ell \leq 3$ and $1 \leq i \leq 3$, K is the diffusion coefficient, f_1 is a function of its argument that specifically includes three-dimensional convection, p is a generalized solution parameter, and f_2 is the initial-value operator. The boundary condition statements for each of the dependent variables can be concisely expressed in the form

$$\ell(q) = a^{(1)}q + a^{(2)}K\frac{\partial q}{\partial x_\ell}\hat{n}_\ell + a^{(3)} = 0 \tag{75}$$

i.e., the normal derivative of q is constrained by q and a parameter as determined by specification of the $a(i)$. An initial condition is required for q identified with each dependent variable as,

$$q(x_1(0),x_2,x_3) \equiv q_0(x_2,x_3) \tag{76}$$

The finite element solution algorithm is based upon the assumption that $L(q)$ is uniformly parabolic within a bounded open domain Ω ; that is, the lead term in equation (74) is uniformly elliptic within its domain R, with closure ∂R, where

$$\Omega \equiv R \times [\chi_0,\chi) \tag{77}$$

and $\chi_0 \leq \chi$. For the 3DPNS equations, χ is associated with the x_1 coordinate. Equation (75) expresses functional constraints on the closure of Ω, $\partial\Omega \equiv \partial R \times [\chi_0,\chi)$, and the initial-condition specification, equation (76), lies on $R \cup \partial R \times \chi_0$.

The concept of the finite element algorithm involves the assumption that each dependent variable is separable in the form

$$q^*(x_i) = q_1(x_1)q_2(x_2,x_3) \tag{78}$$

The functional dependence in $q_2(x_2,x_3)$ is represented by a polynomial in x_ℓ . The expansion coefficients q_1 can be most conveniently expressed in terms of the value of $q^*(x_i)$ at the nodes of the finite element discretization of R. Then, equation (78) takes the form

$$\begin{aligned} q_m^*(x_i) &= \phi_1(x_\ell)Q_1(x_1) + \phi_2(x_\ell)Q_2(x_1) + \phi_3(x_\ell)Q_3(x_1) \\ &\equiv \left\{\phi(x_\ell)\right\}^T\left\{Q(x_1)\right\}_m \end{aligned} \tag{79}$$

where the polynomials $\phi(x_\ell)$ are known functions of x_2 and x_3. Since they are known, they can be differentiated analytically, e.g.,

$$\frac{\partial q_m^*}{\partial x_2} = \frac{\partial}{\partial x_2}\left[\{\phi(x_\ell)\}^T\right]\{Q(x_1)\}_m \tag{80}$$

Hence, there is no need to establish difference formulae to approximate the differentiated terms in $L(q)$.

The finite element solution algorithm is established for the equation system (74)-(76) using the method of weighted residuals (MWR) formulated on a local basis. Since equation (74) is valid throughout Ω, it is valid within disjoint interior subdomains Ω_m described by $(x_i,\chi)\varepsilon R_m\ [\chi_o\ \chi)$, called finite elements, wherein $\bigcup R_m = R$. The approximate solution for q within $R_m\ x[\chi_o\ \chi)$, called $q_m^*(x_i\ ,\ \chi)$, is given in equation (79). Therein, the functionals $\phi_k(x_\ell)$ are subsets of a function set that is complete on R. The expansion coefficients $Q_k\ (\chi)$ represent the unknown χ- dependent values of $q_m^*\ (x_i,\chi)$ at specific locations interior to R_m and on the closure ∂R_m, called nodes of the finite element discretization of R.

To establish the values taken by these expansion coefficients, require the local error in the approximate solution to both the differential equation $L(q_m^*)$ and the boundary condition statement $\ell(q_m^*)$ for $\partial R_m \cap \partial R \neq 0$, be rendered orthogonal to the space of the approximation functions. Employing an algebraic multiplier λ, the resultant equation sets can be combined as

$$\underset{m}{S}\left[\int_{R_m}\{\phi(x_\ell)\}\ L(q_m^*)d\tau\ -\ \lambda\int_{\partial R_m\cap\partial R}\{\phi(x_\ell)\}\ell(q_m^*)d\tau\right]\ \equiv\ \{0\} \tag{81}$$

where $\underset{m}{S}$ is the mapping function from the finite element subspace R_m to the global domain R, commonly termed the assembly operator. The number of equations (81) prior to assembly is identical with the number of node points of the finite element R_m.

Equation (81) forms the basic operation of the finite element solution algorithm and of the COMOC computer program to be described. The lead term can be rearranged, and λ determined by means of a Green-Gauss theorem:

$$\int_{R_m}\{\phi(x_\ell)\}\ \frac{\partial}{\partial x_\ell}\left[K\ \frac{\partial q^*}{\partial x_\ell}\right]d\tau = \oint_{\partial R_m}\{\phi(x_\ell)\}\ K\frac{\partial q^*}{\partial x_\ell}\hat{n}_\ell\ d\tau$$

$$-\int_{R_m}\frac{\partial}{\partial x_\ell}\{\phi(x_\ell)\}\ K\frac{\partial q^*}{\partial x_\ell}d\tau \tag{82}$$

For $\partial R \cap \partial R_m$ nonvanishing in equation (82), the corresponding segment of the closed-surface integral will cancel the boundary condition contribution equation (81) by identifying $\lambda a^{(2)}$ with K, equation (74). The contributions to the closed-surface integral, equation (82) whereat $\partial R_m \cap \partial R = 0$, can also be made to vanish. The globally assembled finite-element solution algorithm for the representative partial differential equation system then becomes

$$\underset{m}{S}\left[-\int_{R_m}\frac{\partial}{\partial x_\ell}\{\phi\}\,K\frac{\partial q^*}{\partial x_\ell}\,d\tau+\int_{R_m}\{\phi\}\,(f_1^*+f_2^*)\,d\tau\right.$$
$$\left.-\int_{\partial R_m\cap\partial R}\{\phi\}\left[a^{(1)}q^*+a^{(3)}\right]d\tau\right]\equiv\{0\} \tag{83}$$

The rank of the global equation system (83) is identical with the total number of node points on $R \cup \partial R$ for which the dependent variable requires solution. For f_2 non-vanishing, equation (83) is a first-order, ordinary differential equation. Solution of this system is obtained by COMOC using a predictor-corrector finite-difference numerical integration algorithm. For f_2 vanishing identically, equation (83) is large order algebraic, and the matrix structure is sparse and banded. Solution of this system is obtained in COMOC using a banded Cholesky equation solver. Solution is also required for the continuity equation (72), which is retained for boundary-layer flows. Since it exists in standard form as an ordinary differential equation, direct numerical integration yields the required solution at node points of the discretization.

COMOC COMPUTER PROGRAM

The finite element solution algorithm is utilized, as observed in the previous section, to cast the original initial-boundary value problem descriptions into large-order systems of purely initial-value or algebraic equations. The COMOC computer program system is being developed to transmit the rapid theoretical progress in finite element solution methodology into a viable numerical solution capability. COMOC integrates or equation solves the discretized equivalent of the governing equation systems. Initial distributions of all dependent variables may be appropriately specified or computed, and boundary constraints for each dependent variable can be specified on arbitrarily disjoint segments of the solution domain closure. The solutions for each dependent variable, and all computed parameters, are established at node points lying on a specifiable nonregular computational lattice, formed by plane triangulation of the elliptic portion of the solution domain Ω, i.e., $R \cup \partial R$.

Detailed discussion on the functional design of COMOC is presented elsewhere (ref. 23). The COMOC system is built upon the macrostructure illustrated in Figure 2. The main executive routine allocates core, using a variable dimensioning scheme, based upon the total degrees of freedom of the global problem statement. The size of the largest problem that can be solved is thus limited (only) by the available core of the computer in use. The precise mix between dependent variables and parameters, and fineness of the discretization, is user-specifiable and widely variable. The Input module serves its standard function for all arrays of dependent variables, parameters, and geometric coordinates. The Discretization module forms the finite-element discretization of the elliptic solution domain and evaluates all required finite-element nonstandard matrices and standard-matrix multipliers. The Initialization module computes the remaining initial parametric data required to start the solution. The Integration module constitutes the primary execution sequence of problem solution, and utilizes a highly stable, predictor-corrector integration algorithm for the column vector of unknowns of the solution. Calls to auxiliary routines for parameter evaluation (effective viscosity, Prandtl number, source terms, etc.) as specified functions of dependent and/or independent variables, as well as calls for equation solving algebraic systems, are governed by the Integration module. The Output module is similarly addressed from the integration sequence and serves its standard function via a highly automated array display algorithm. COMOC can execute distinct problems in sequence, and contains an automatic restart capability to continue solutions.

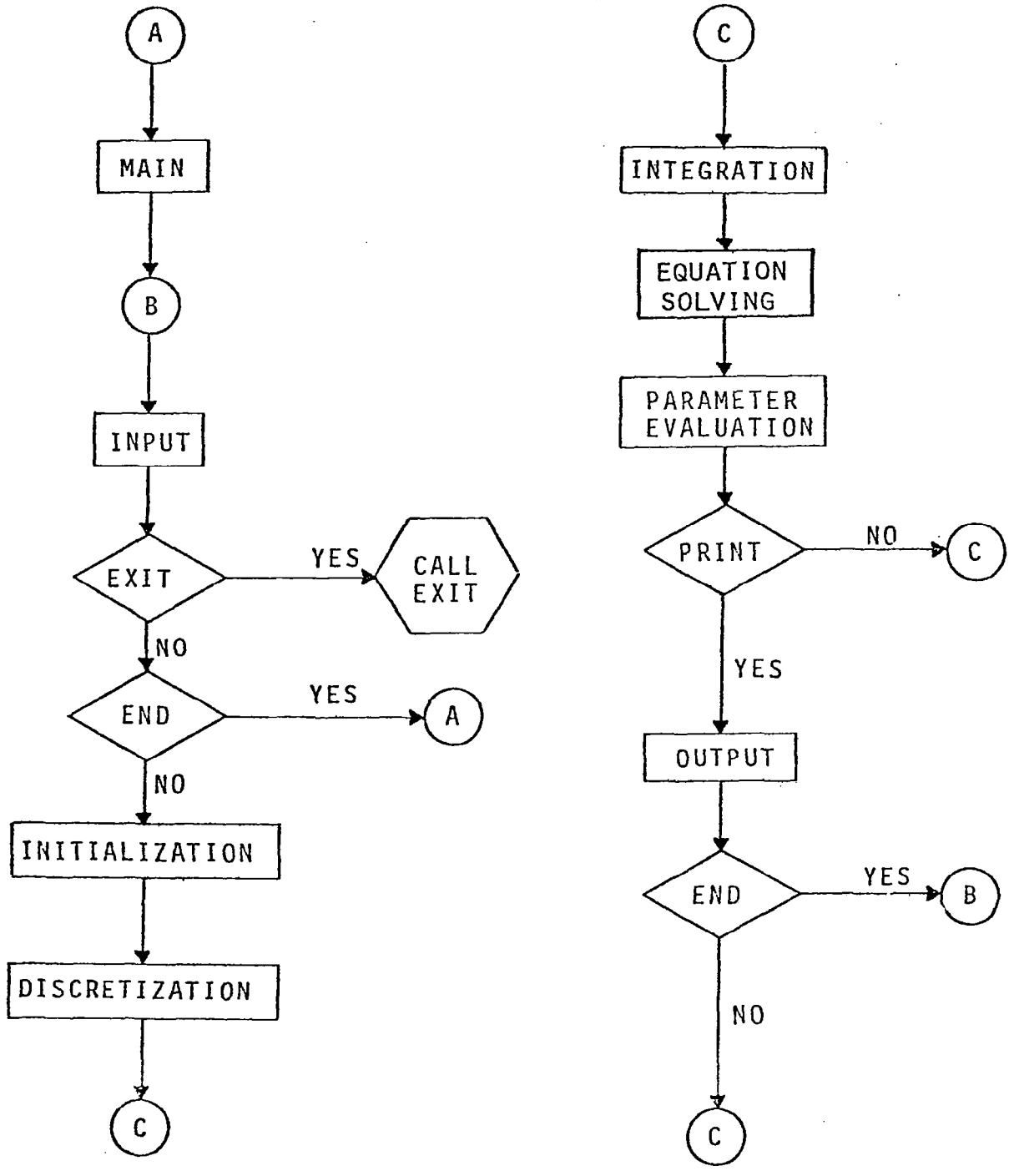

Figure 2. COMOC Macro-structure.

A key feature of the developing COMOC system is automated discretization and subsequent refinement using the concept of a finite element "super element." A geometrically complex two-(and potentially three-) dimensional solution domain is resolved into a number of sub-domains, the number and shape of which is rather arbitrary. The main purpose is to describe the geometry of the complete problem as the union of many elementary geometries, each of which can be adequately described by a few (six or eight) geometric coordinate pairs. This is shown in Figure 3 for a three- and four-sided super-element shape. These coordinate pairs are then assumed to describe quadratic surface curvature (hence, no inflection point allowed), the basis of which is employed to determine a new curvilinear coordinate system wherein the super element is a regular straight-sided polygon. This transformed shape is then divided into equal size sub-domains according to an integer input by the user. The coordinate pairs of the sub-domain discretization are then transformed to the physical plane via the inverse transformation. The program automatically determines inter-element connectivities, and numbers the resultant node points to minimize matrix bandwidth. The net result is automated generation of a finite element computational discretization in the physical plane. The discretization can be made non-uniform according to a smooth progression by placement of non-vertex coordinate pairs of the super element description nearer the desired vertex node. Figure 4 illustrates the super element and resultant finite element discretizations for an isolated airfoil of 12 elements and 648 finite elements respectively. Refinement of the discretization is accomplished at the super element input level by merely requesting a larger number of finite elements to be generated in the transform plane. It must be mentioned that the procedure is not absolutely foolproof since the inverse coordinate transformation is not unique. In particular, placement of non-vertex super element coordinate pairs too near a vertex pair can induce an inverse mapping that is non-planar, i.e., the generated discretization overlaps upon itself. A computer plot of the generated discretization can be of considerable usefulness in this regard. A detailed discussion on the theoretical aspects of this feature is included in the Appendix.

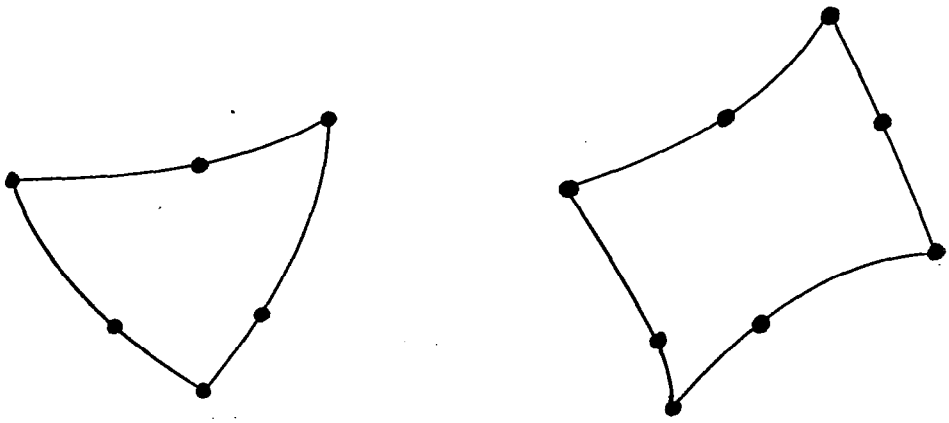

Fig. 3. Three and Four-Sided Super Element Domains

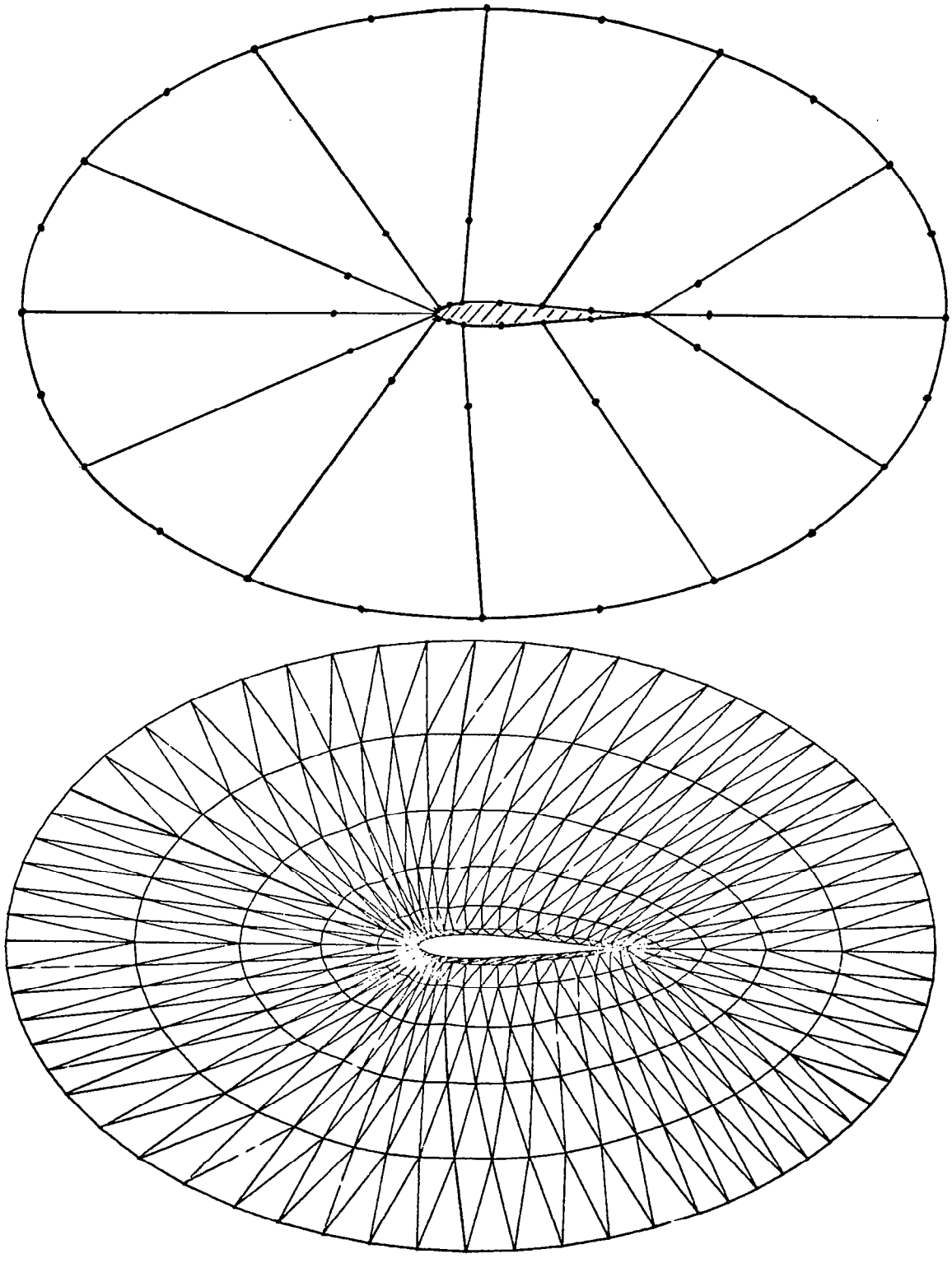

Fig. 4. Super Element and Finite Element Discretizations For Isolated Elementary Airfoil

NUMERICAL RESULTS

The goal of the numerical evaluations is to verify finite element solution methodology applied to the components of a weak interaction solution of subsonic two-dimensional aerodynamic flow over an isolated airfoil. Since the finite element algorithm, equation (81), is fundamentally independent of the dimension of the problem space, lower dimensional results can usefully verify inherent capabilities and limitations. The numerical test cases, the results of which are presented and discussed herein, evaluate solution accuracy, convergence with discretization refinement, and the use of non-uniform finite element discretizations to enhance both. Accuracy of potential flow about both a NACA 4-digit and a Joukowski airfoil is documented, including computational application of the Kutta trailing edge condition. Solution of turbulent and non-equilibrium boundary layer flows, including adverse pressure gradient, documents computational accuracy as well as use of first and second order turbulence closure. Results for wake flow solutions document merging of dissimilar viscous and turbulent flows downstream of a sharp trailing edge. The final section indicates iteration among these various flows for a representative weak-iteration solution.

Aerodynamic Potential Flow

Two accuracy measures (norms) are required to be evaluated. From the mathematics viewpoint, for a linear, elliptic boundary value problem, such as equations (28) and (32), the accuracy of the numerical solution is intrinsicly measured in an energy norm, $E(\ ,\ )$

$$E(\phi^*,\phi^*) \equiv \frac{1}{2}\int_R \frac{\partial\phi^*}{\partial x_\ell}\frac{\partial\phi^*}{\partial x_\ell}d\tau = \frac{1}{2}\sum_{m=1}^{M}\int_{R_m}\frac{\partial\phi_m^*}{\partial x_\ell}\frac{\partial\phi_m^*}{\partial x_\ell}d\tau \qquad (84)$$

Since the finite element mesh is non-overlapping on R, the second form of equation (84) demonstrates the integrals are performed on R_m and summed over all M. Further note that equation (84) indeed measures kinetic energy per unit mass, see equation (24). Denoting h as a presentative finite element dimension, the accuracy of the finite element solution will converge to the analytical solution as (cf., ref. 24).

$$E(\phi-\phi^*,\phi-\phi^*) \le C\frac{h^p}{\alpha}\max|\phi''|^2 \qquad (85)$$

In equation (85), ϕ is the exact solution, ϕ'' is its extremum second derivative, C is a constant, and p is an integer dependent upon the degree of the finite element approximation function, $\{\phi(x_\ell)\}$, equation (79). The coefficient α is a measure of discretization skewness, and can

be interpreted as the extremum ratio of radii of inscribed and circumscribed circles about each (triangular) finite element. Numerical solutions allow determination of the actual value of p. If close to its theoretical value, one can estimate with accuracy the improvement in the solution that will result from refinement of the discretization.

The second and more practically important accuracy measure is pressure coefficient C_p, equations (33)-(36), since its distribution drives the weak-interaction solution. The finite element solution computes $\phi(s)$ directly, since $a^{(3)}$ is non-vanishing on the airfoil surface, see equation (83). The fundamental evaluation is then accuracy of the computed tangential derivative of ϕ for a curvilinear coordinate s, knowing n discrete values of ϕ at non-uniform displacements Δs. This is a classic problem in interpolation theory, and cubic splines as well as difference methods were evaluated. For the former, $\partial\phi/\partial s$ is determined at the finite element gridpoints on the airfoil by interpolation of $\phi(s)$ assuming a spline approximation. The increments Δs are evaluated using Simpson's rule to integrate the differential equation for arc length,

$$\frac{ds}{dx_1} = \left[1 - \left(\frac{\partial x_2}{\partial x_1}\right)^2\right]^{\frac{1}{2}} \tag{86}$$

In turn, the tangent slope required in equation (86) is obtained from a cubic spline interpolation of the discrete coordinate pairs defining the airfoil surface.

The first requirement is to confirm order of accuracy, i.e., the exponent p in equation (85), and to evaluate absolute accuracy of the finite element prediction of $\phi(s)$. The only factor driving the solution for ϕ, equation (32), is the gradient boundary condition enforcing flow tangency, equation (28). This in turn is a function only of the resolution of the surface normal distribution, $\hat{n}_i$, and the manner in which the finite element algorithm extremizes solution energy E, equation (84), subject to this type constraint. To maintain simplicity, all computations were performed using triangular, two-dimensional finite elements spanned by simplex functionals. Hence, the theoretical value for convergence rate p, equation (85), is two. The problem selected is flow over a slender parabolic-arc airfoil with sharp leading and trailing edges. The airfoil is simulated as a symmetric sine wave with thickness ratio $\varepsilon\lambda^{-1}$, where λ is the period and ε the amplitude of the contour. Since the problem possesses quadrant symmetry, only a quarter-domain numerical solution is required. Figure 5 displays the boundary condition constraints for this domain, the basic "super-element" discretization, and a representative uniform finite element discretization as generated by COMOC. For the slender body approximation, wherein the zero normal-wash boundary constraint can be applied on the mean chord (which is the x_1 axis), an analytical solution exists as (eg., ref. 25)

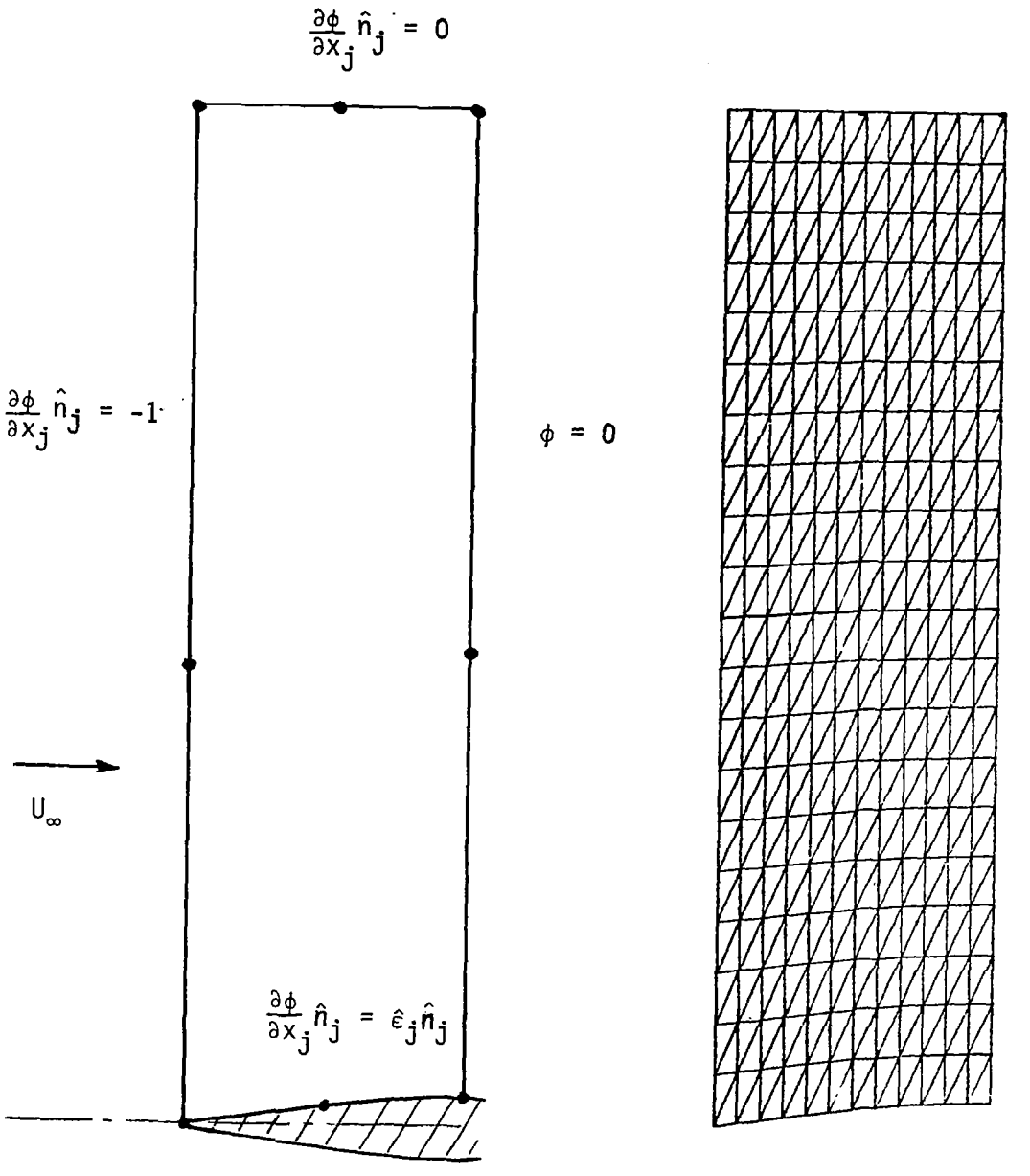

Fig. 5. Super Element and Finite Element Discretizations For Flow Over Parabolic Arc Airfoil

$$\phi(x_\ell) = \varepsilon \cos 2\pi x_1 \lambda^{-1} \exp(-2\pi x_2 \lambda^{-1}) \qquad (87)$$

Therefore, for this simplification, both accuracy and convergence can be measured exactly.

Convergence for COMOC-generated solutions has been determined for three-levels of discretization refinement for $32 \leq M \leq 512$, where M is the number of triangular finite elements spanning R. Shown in Figure 6 is the plot of finite element solution energy E, equation (84), as a function of discretization. Shown for comparison is a line denoting exact quadratic convergence, p = 2, equation (85). As observed, the convergence rate in energy closely approximates quadratic for the refined grid. Interestingly (cf., ref. 24), the convergence is from above, i.e.,

$$E(\phi-\phi^*,\phi-\phi^*) \geq 0 \qquad (88)$$

Hence, for perturbation potential function, solution energy appears extremized by the finite element procedure according to a complementary energy principle.

Solution accuracy responds favorably to the use of non-uniform discretizations. Shown also in Figure 6 is a computed solution energy for the fine grid case, obtained with a discretization scaled as non-uniform to enhance resolution in regions where gradients in ϕ were largest. As observed, a non-uniform discretization can provide a given level of solution accuracy (in E) using fewer finite elements. Conversely, for a given number of elements, greater accuracy can be acheived using non-uniform grids. This can be of particular economic importance for flowfield determination about actual airfoil contours.

The accuracy of the algorithm for determination of C_p, was evaluated for a parabolic arc airfoil of chord, C = ¶. Shown in Table 2, as a function of distance from the leading edge, is a comparison between the analytical solution C_p, and numerical determinations using the computed finite element distributions of $\phi(s)$ for 13 and 25 nodes placed on the airfoil surface. Two cases are shown for each discretization, corresponding to spline and (second-order accurate) finite difference evaluation of $\partial\phi/\partial s$, respectively. The maximum error is less than 1% throughout. Interestingly, the finite difference evaluations evidence convergence with discretization refinement (maximum error decreases from 0.6 to 0.2%), while the spline results are essentially unaffected. Shown in Table 3 is a detailed comparison between exact and computed values of each of the three terms comprising C_p, see equation (36) for the coarser grid finite element solution. The major error is observed to be evaluation of the dominant second term. Note that the third term, usually discarded for linearized theory, contributes up to about 8% of the total C_p at mid-chord. Hence, there appears no apriori reason to drop

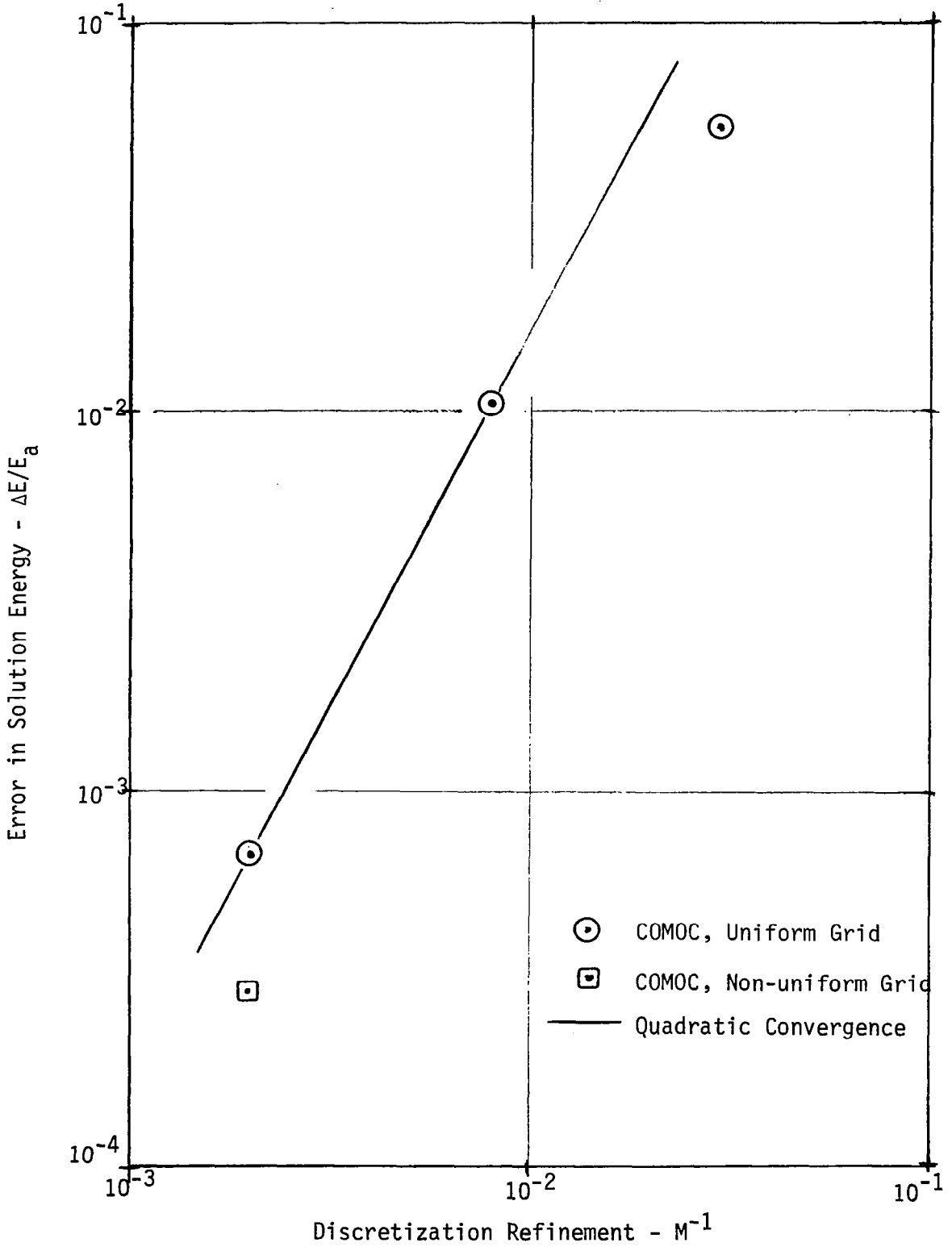

Fig. 6 Convergence of Finite Element Solution In Energy Norm for Aerodynamic Flow Over Parabolic Arc Airfoil

TABLE 2

Pressure Coefficient Distribution for

Parabolic Arc Airfoil, $\varepsilon/\lambda = 0.025$

Coordinate x/C	Pressure Coefficient - C_p				
	Analytical	Numerical, n = 13		Numerical, n = 25	
		Spline	F.D.	Spline	F.D.
0.0	-.0247	-----	-----	-----	-----
0.0417	-.0657	-.0652	-----	-.0651	-.0657
0.0833	-.1060	-.1049	-.1062	-.1049	-.1060
0.125	-.1449	-.1434	-.1453	-.1434	-.1449
0.1667	-.1818	-.1799	-.1823	-.1799	-.1818
0.2083	-.2159	-.2139	-.2167	-.2138	-.2160
0.25	-.2468	-.2447	-.2478	-.2447	-.2470
0.2917	-.2739	-.2719	-.2752	-.2719	-.2741
0.3333	-.2967	-.2950	-.2982	-.2950	-.2970
0.375	-.3149	-.3135	-.3166	-.3135	-.3153
0.4167	-.3281	-.3272	-.3300	-.3272	-.3286
0.4583	-.3361	-.3356	-.3382	-.3357	-.3367
0.5	-.3388	-.3388	-.3409	-.3388	-.3394

TABLE 3

Accuracy of Individual Terms in

The Pressure Coefficient Algorithm, Equation (36)

Coordinate x/C	Analytical Solution			Finite Element Solution		
	1 *	2	3	1	2	3
0.0	.0241	-.0482	-.0006	-----	-----	-----
0.0417	.0237	-.0874	-.0020	.0237	-.0870	-.0019
0.0833	.0225	-.1245	-.0040	.0225	-.1236	-.0039
0.125	.0206	-.1590	-.0065	.0206	-.1577	-.0063
0.1667	.0182	-.1906	-.0092	.0182	-.1890	-.0091
0.2003	.0153	-.2189	-.0122	.0153	-.2172	-.0120
0.25	.0122	-.2438	-.0150	.0122	-.2421	-.0148
0.2917	.0091	-.2651	-.0177	.0091	-.2634	-.0175
0.3333	.0061	-.2827	-.0201	.0061	-.2812	-.0199
0.375	.0036	-.2964	-.0220	.0036	-.2952	-.0219
0.4167	.0017	-.3063	-.0235	.0016	-.3054	-.0234
0.4583	.0004	-.3122	-.0244	.0004	-.3117	-.0243
0.5	.0	-.3142	-.0247	.0	-.3142	-.0247

* Terms 1,2,3 correspond to order of terms in equation (36)

the term since its evaluation is straightforward using the developed algorithm.

Determination of accuracy of computed distribution of C_p was accomplished by prediction of flow over a Joukowski airfoil for several thickness ratios and angles of attack. Initial computations utilized total potential function Φ, commonly employed as documented in the finite element literature. This approach was rapidly discarded, however, as numerical results indicated that C_p solution accuracy was highly sensitive to local variations in discretization uniformity including inclination of the element diagonals. This results directly from use of the vanishing gradient boundary condition, equation (23), over which no direct control can be exerted. Solutions using perturbation potential function have been much more successful. Following detailed numerical evaluations, it was determined that the "infinity" boundary condition, equation (27), should be placed at least one chord length (C) away from the airfoil, except in the leading edge region where it should lie 1.5C upstream. Therefore, a computational solution domain, lying 1.5C to 2.0C from the airfoil was selected. The airfoil contour was encircled by a super-element discretization employing perturbed ellipse boundaries. This generates a non-uniform discretization, concentrating small finite element domains in regions of high surface curvature and/or large field gradients, and provides smooth transition from fine to coarse grids. Shown in Figure 7 is the established super element discretization, and the corresponding finite element discretization as generated by COMOC. The illustrated discretization contains 648 triangular elements.

For pure potential flow about a symmetric airfoil at zero angle of attack, the solution domain represented in Figure 7 is multiply-connected. Numerical solution for this case verified that the finite element procedure will imbed an effective branch cut from the trailing edge downwind, and will accurately compute a planar wake trajectory. For all other cases, the Kutta condition must be invoked at the trailing edge and at angle of attack, a jump in ϕ occurs everywhere across the wake trajectory. Hence, the solution domain becomes effectively simply-connected as will always occur upon addition of viscous flow effects. The specification of boundary conditions reflects these constraints; they are also noted in Figure 7. The vanishing normal gradient of ϕ is enforced uniformly on the "infinity" closure, while everywhere on the airfoil surface, the normal derivative is constrained by orientation and angle of attack, see equation (28). The nodes located downstream of the trailing edge included-angle bisector are double-numbered and a vanishing normal derivative applied on both sides of the wake trajectory. The distributions of the (+ and -) outward pointing normals for the wake trajectory are assumed to vary quadratically Thus, wake curvature induces smooth transition from the trailing edge to angle of attack at 1.5C downstream. The arbitrary constant value of ϕ is set (only) at the extremum upstream node. Therefore, circulation, lift, stagnation point and C_p are all direct output variables and under no direct user constraint.

Perturbation potential function distributions were computed for flow over a symmetric, 12% thick Joukowski airfoil at five angles of attack, $0^o \leq \alpha \leq 8^o$. Angle of attack specification was accomplished through rotation of the freestream in the gradient boundary condition statement as discussed.

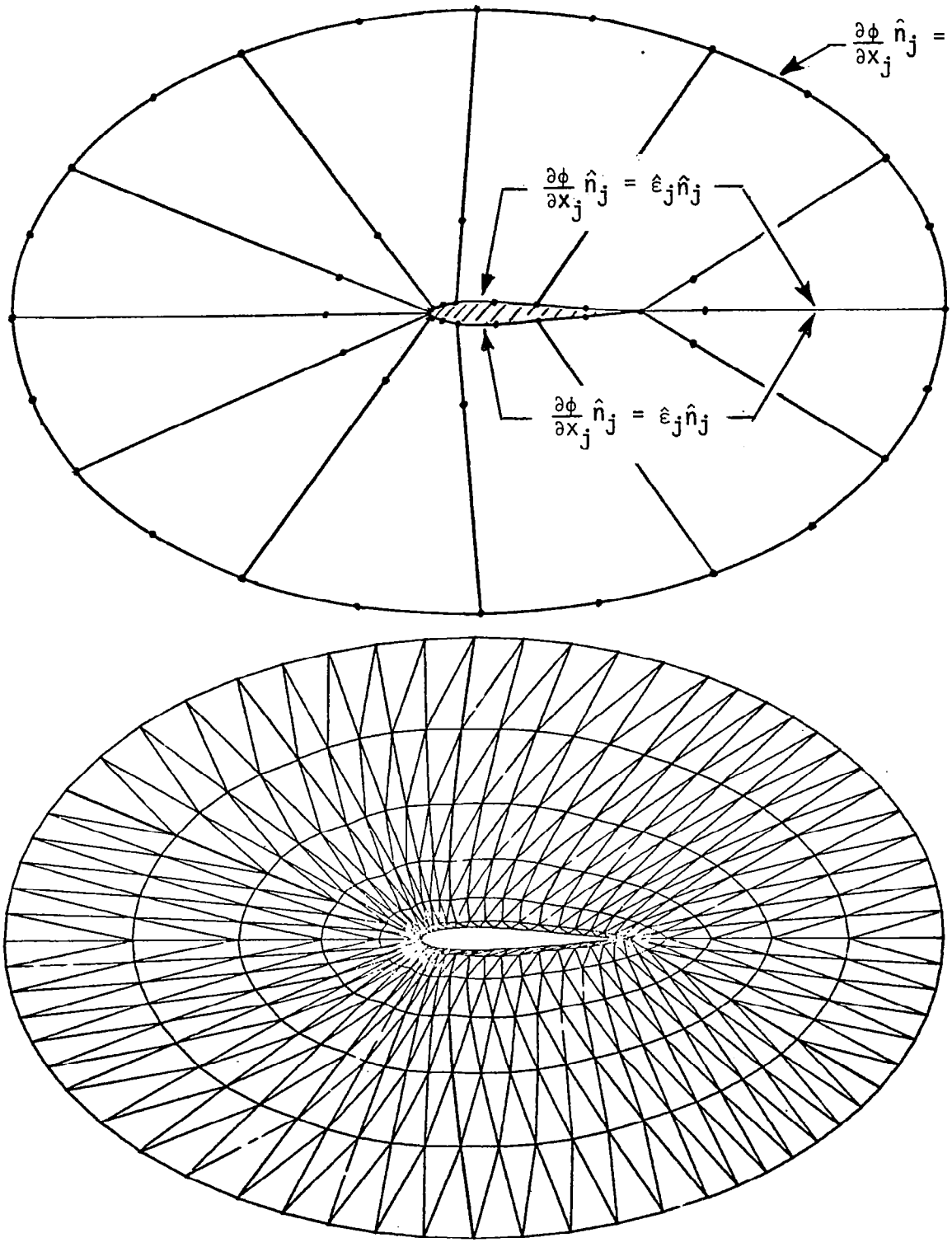

Fig. 7. Super Element and Finite Element Discretizations For Flow Over Symmetric Joukowski Airfoil

Computer-generated isobar distributions for the finite element solutions are shown in Figure 8. Note the near exact symmetry for zero angle of attack, even though the discretization is not symmetric, see Figure 7. This was not the case for use of total potential function. The solution extremum is centered on the stagnation point for $\alpha = 0^{\circ}$ and 2°. As angle of attack is further increased, the extremum moves into the entire lower half plane and becomes distributed along the trailing edge branch cut. The increase in the jump of ϕ across the wake trajectory is also graphically evident as α increases. For all cases, note the fidelity with which the solution approximates the vanishing normal gradient around the freestream boundary. Relative magnitude of perturbation velocity levels are readily discerned since equal increments in ϕ are plotted in each case.

The aerodynamic lift is strictly a function of circulation, Γ, which is related in an elementary manner to the jump in ϕ at the trailing edge. Shown in Table 4 is the lift coefficient, C_L, computed from the finite element solutions of ϕ, $0^{\circ} \leq \alpha \leq 8^{\circ}$. Agreement with the exact values is good, with a nominal error of 3% essentially independent of α. The non-zero computed lift for zero angle of attack is one measure of the numerical error induced by the non-symmetric discretization. Its value is certainly nominal.

The aerodynamic parameter of primary impact for the weak interaction solution is surface pressure distribution, from which can be determined pressure coefficient as well as form drag and pitching moment. Shown in Fig. 9 is a composite plot of C_p versus α, as determined by use of the finite element computed distribution of $\phi(s)$ within the C_p algorithm, equation (36) and using the cubic spline technique. Agreement with the analytical solution is generally good over this range of angle of attack, regarding prediction of extrema, stagnation point and in the general overall shape of the curves (which have not been smoothed). The extremum low pressure on the upper surface is universally underpredicted, as one would expect, (since the ϕ solution is basically interpolatory), but the surrounding curve shape is good. The same holds for prediction of stagnation point. The finite element bound on stagnation point location, defined as the half-domain span surrounding the computed maximum C_p, agrees well with the exact solution, as shown in Table 4.

The stability of the weak-interaction solution algorithm is fundamentally a function of phenomena in the immediate vicinity of the trailing edge of the isolated airfoil. It is within this region that slope discontinuities occur in C_p. Shown in Figure 10 is an expanded scale plot of computed C_p for $\alpha = 6^{\circ}$ including prediction on the trailing edge wake centerline. General agreement with data is good, although detailed differences and discrepancies are noted. The computed values of lower and upper surface C_p at the trailing edge are not equal. However, the curves do cross immediately downstream of the trailing edge. Since the ϕ domain is singly-connected, and since prediction of C_p starts at the leading edge (even at angle of attack) as an initial-value determination, there is no mechanism present to

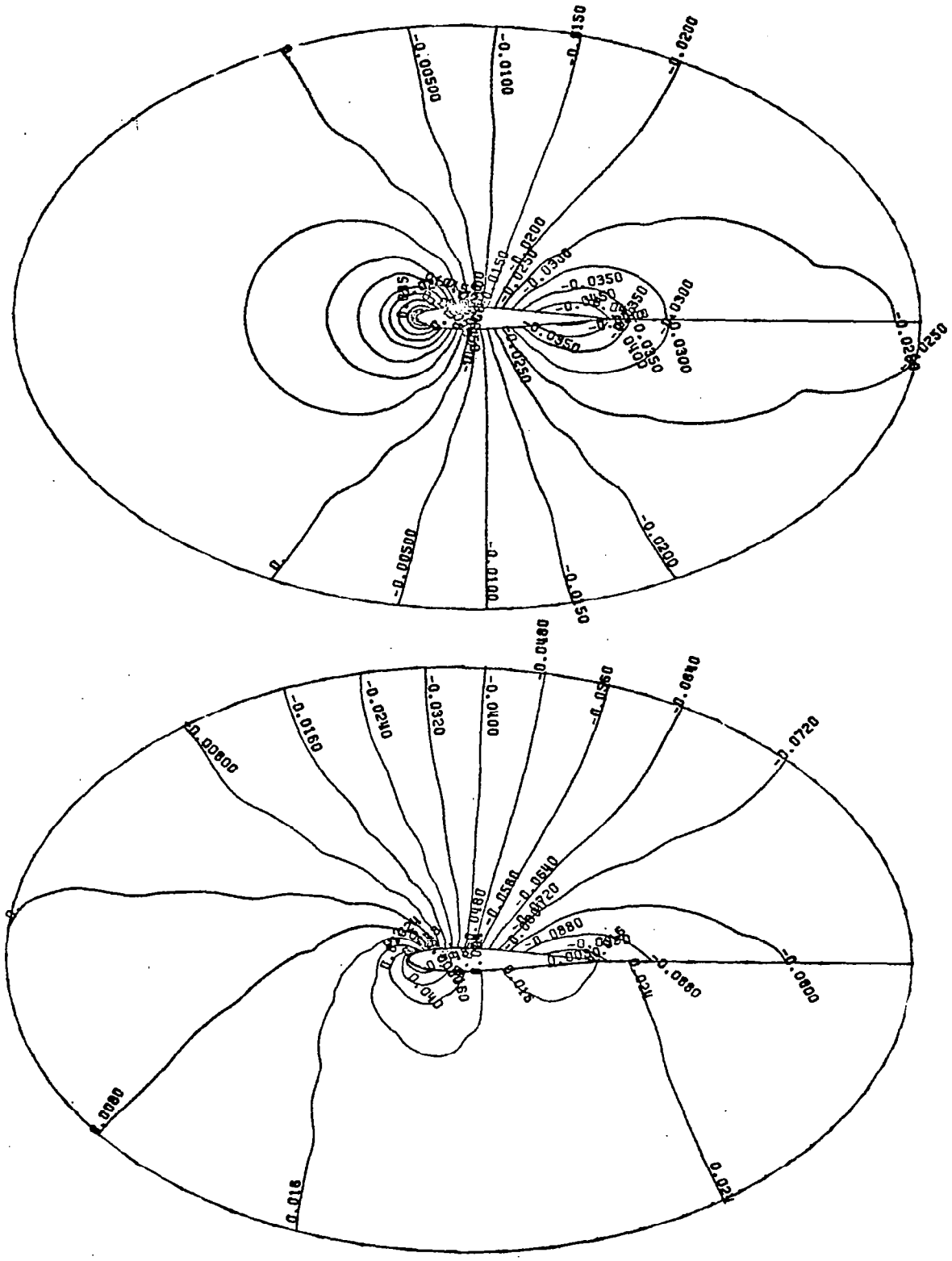

Fig. 8. Computed Potential Distributions for Joukowski Airfoil, t/C = 0.12, a) $\alpha = 0^{o}$, b) $\alpha = 2^{o}$

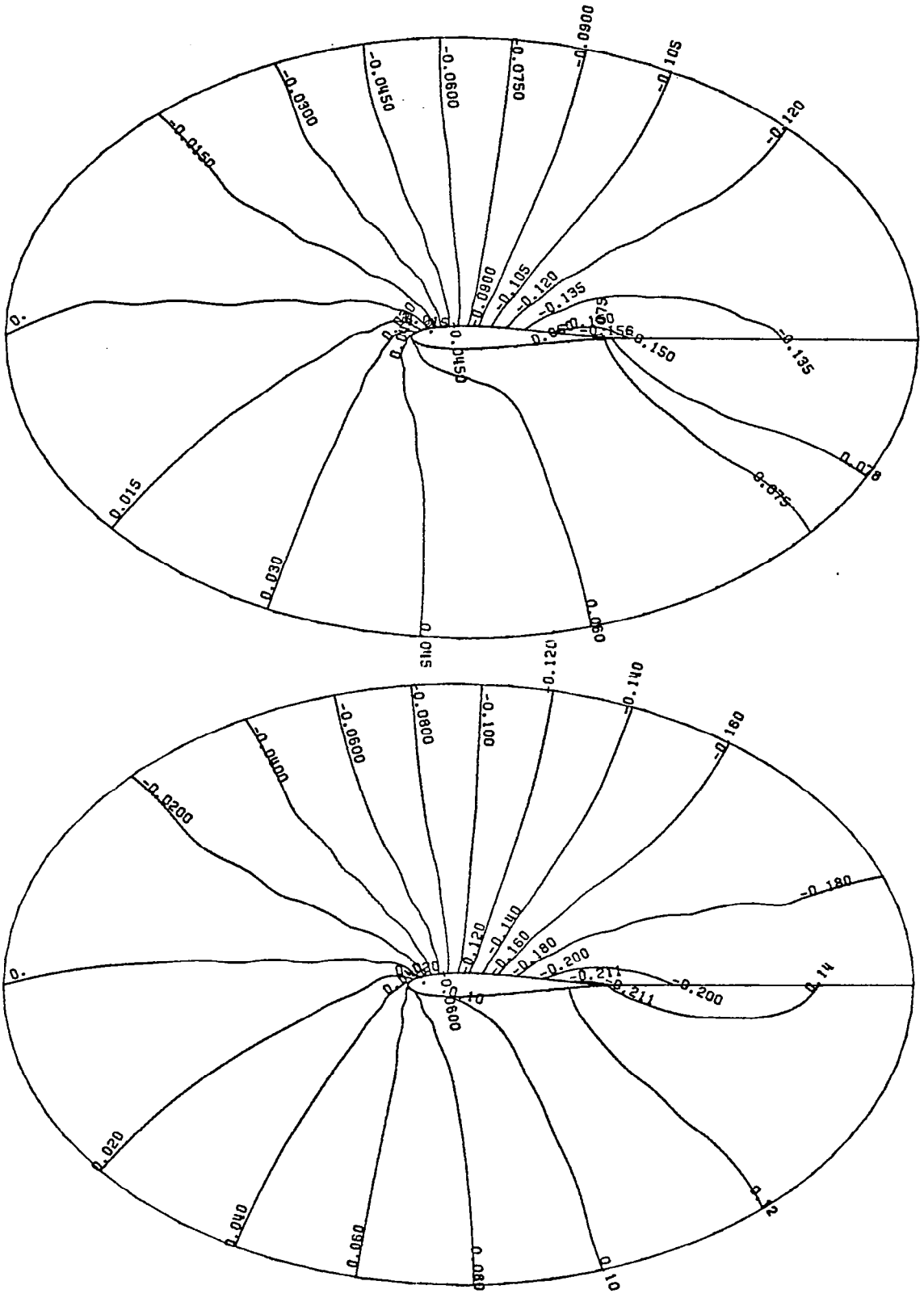

Fig. 8 (cont'd) Computed Potential Distributions for Joukowski Airfoil, c) $\alpha = 4^{\circ}$, d) $\alpha = 6^{\circ}$

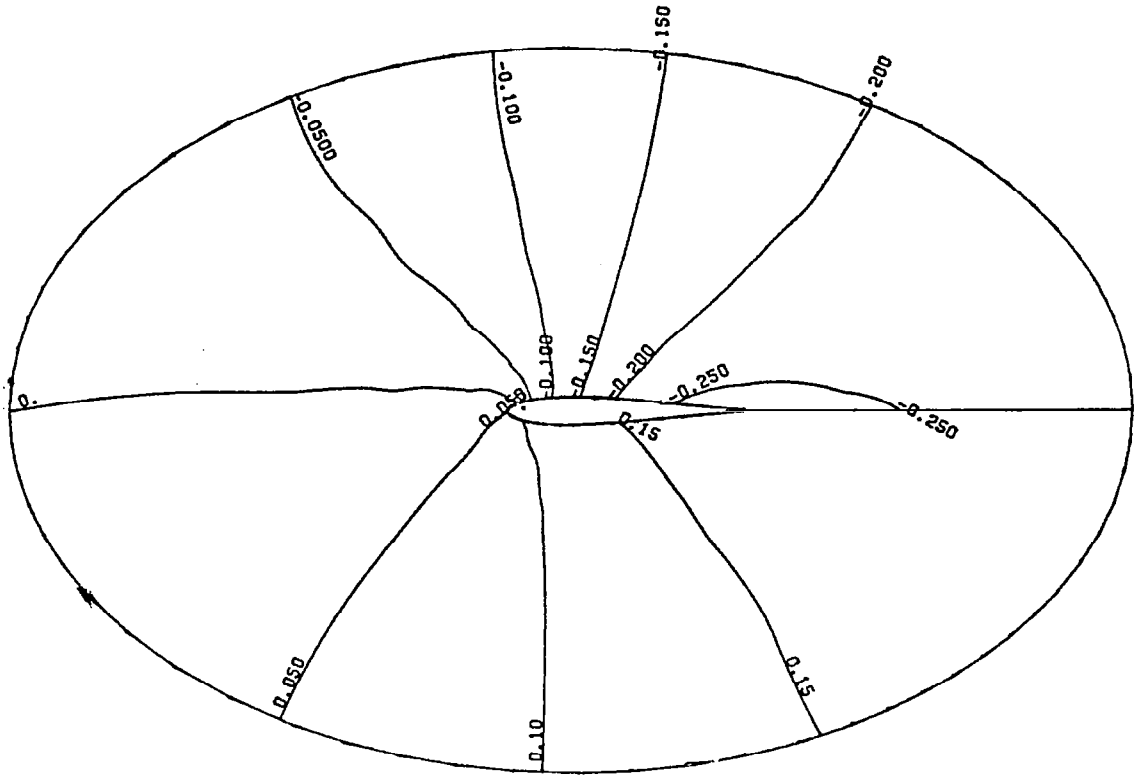

Fig. 8 (cont'd) Computed Potential Distributions for Joukowski Airfoil, e) $\alpha = 8^{o}$.

TABLE 4

Aerodynamic Parameters for Joukowski Airfoil

Angle of Attack, α	Lift Coefficient C_L Finite Element	Exact	Stagnation Point - C_L Finite Element	Exact
0.	0.001	0.0	.000	0.0
2.	0.232	0.237	.0000 –.00117	0.0011
4.	0.462	0.478	.00117–.00779	0.0042
6.	0.694	0.716	.00779–.01987	0.0094
8.	0.924	0.954	.00779–.01987	0.0167

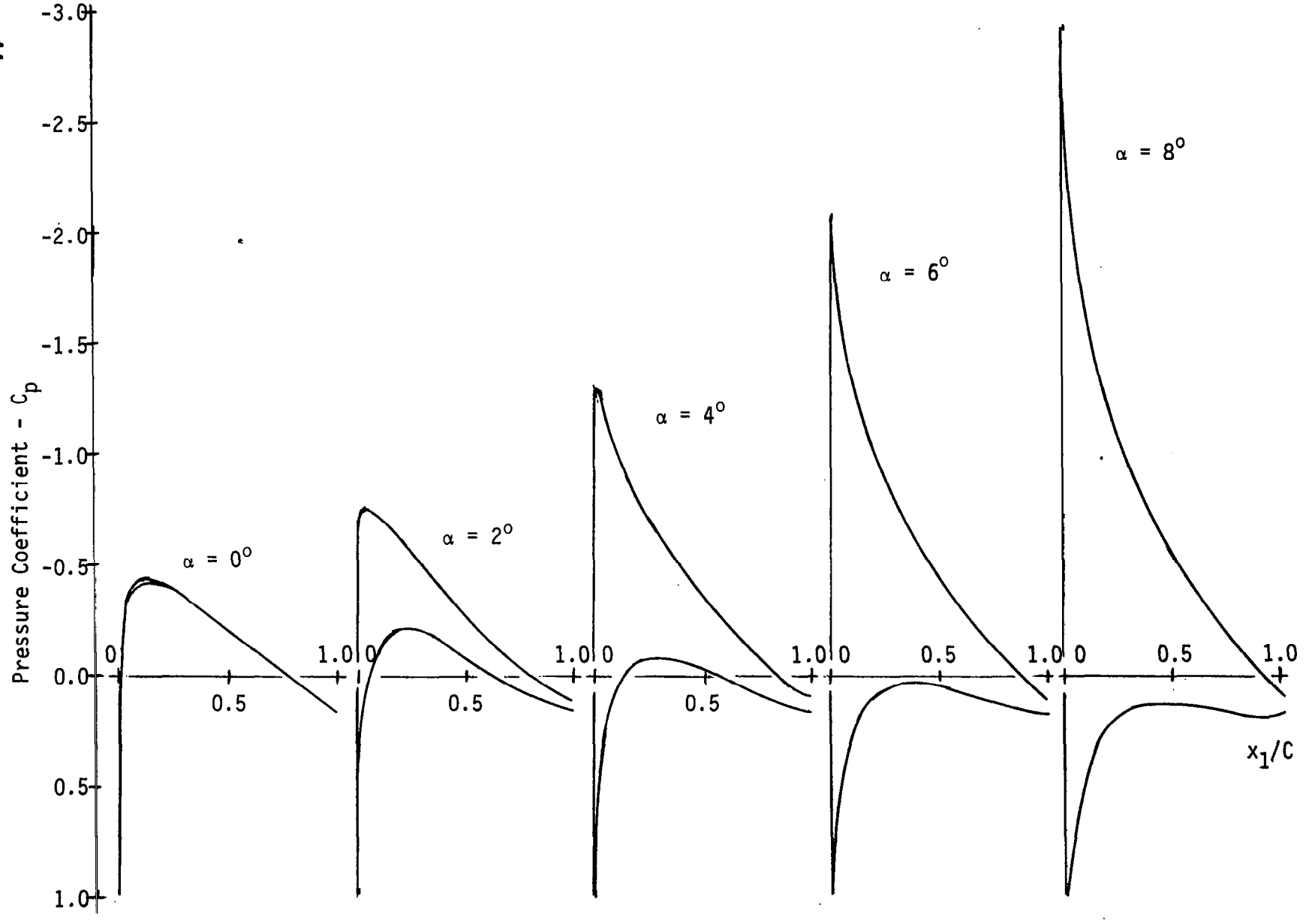

Fig. 9 Computed Pressure Coefficient Distributions on Joukowski Airfoil, t/C=0.12, $0° \leq \alpha \leq 8°$

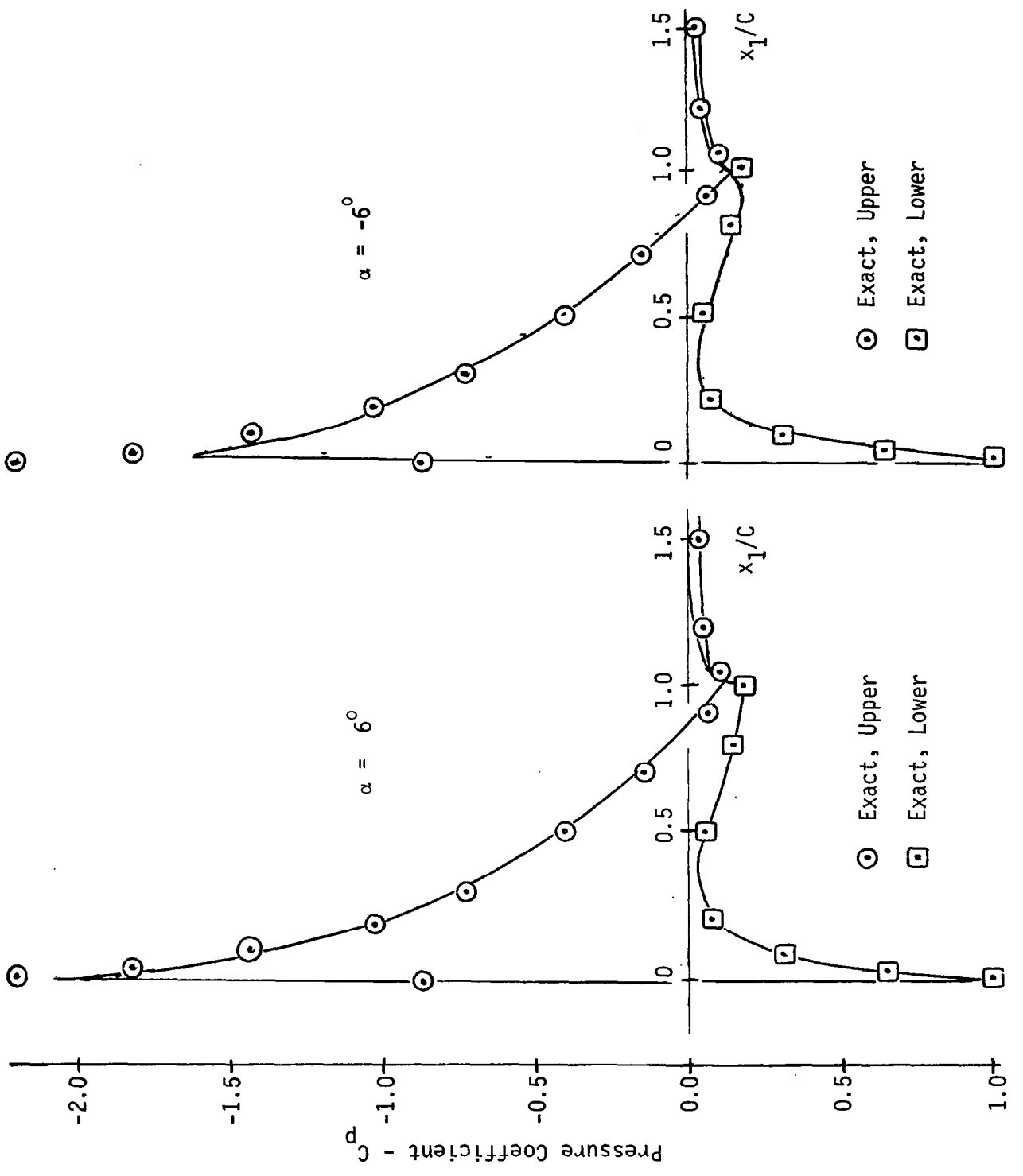

Fig. 10 Pressure Coefficient Distribution on Joukowski Airfoil and Trailing Edge Wake, $\alpha = 6^{\circ}$

enforce uniqueness at the trailing edge. Shown in Table 5 is the computed difference in C_p at the trailing edge node location as a function of α .

Table 5

Pressure Coefficient Difference at Trailing Edge

Of Joukowski Airfoil

Angle of Attack α	Pressure Coefficient, C_p		
	Upper	Lower	Difference
0	0.1166	0.1516	-0.035
2	0.1094	0.1587	-0.049
4	0.08915	0.1664	-0.077
6	0.1039	0.1700	-0.066
8	0.0876	0.1680	-0.080

Note that, even though the finite element solution for ϕ was symmetric to C_L = 0.001 for zero angle of attack, that accumulated error in determina- of C_p produced a trailing edge difference of 0.035. This could be attributable to the difference in diagonal orientation within the discretization, see Figure 7, since "averaging" solutions obtained with the given discretization, and one with the opposite diagonal orientation, would obviously eliminate the C_p difference. Alternatively, it could be accumulated round-off error in the C_p spline algorithm, since upper and lower surface normal vectors are of opposite sign and no advantage has been taken of the intrinsic problem symmetry. Finally, it could be associated with the Joukowski cusped trailing edge, which is only approximately modeled for any discretization. From Table 5, the computed trailing edge difference appears essentially insensitive to angle of attack.

The remaining difference may be attributed to the influence of the assumed wake trajectory curvature on the solution. An airfoil itself provides ample evidence that flow curvature can support a pressure gradient. The exact solution, obtained using conformal mapping does not "possess" a wake, and therefore is insensitive to the manner in which the velocity vector at

the trailing edge is rotated to freestream orientation. However, in the present boundary value solution, the wake trajectory is as much an impervious surface as is the airfoil itself. Since the distribution of the normal to the wake is assumed quadratic, the wake trajectory itself is cubic. The constraints on the cubic curve are known slope at each end (Kutta condition and freestream), known trailing edge intercept, and the assumed quadratic variation of $\hat{n}_k$. Several other trailing edge orientations were evaluated for the 6^o angle of attack case, including a straight wake trajectory at the Kutta angle and at the freestream angle, and a linear average of these. In all cases, the pressure difference computed at the trailing edge exceeded the present case by a factor of up to four. Therefore, the quadratic normal distribution appears to best simulate the experience with exact solutions.

Considerable additional numerical experimentation could certainly be conducted. The developed spline C_p algorithm may not be optimal, especially since it did not clearly demonstrate convergence under grid refinement for the parabolic arc airfoil test case. Refined grid potential flow solutions should be generated to allow measurement of convergence in the energy norm. This development study could be readily conducted using the COMOC computer program.

One additional point warrants comment. The design trend is to progressively thicker airfoils. As the thickness increases, the placing of flow tangency boundary conditions on the actual surface (instead of the mean chord) becomes additionally important. The finite element concept retains all the required flexibility. For example, shown in Figure 11 are finite element discretizations for solution of 24% thick Joukowski airfoil, accounting for and neglecting the influence of thickness. Figure 12 compares the computed C_p distributions, as obtained by applying identical boundary condition constraints, equation (28), on the surface and on the mean chord. The differences are most pronounced as expected in the region of maximum thickness. In the same manner as produced the "flat plate" Joukowski airfoil approximation, the discretizer in COMOC can readily establish an arbitrary nonsymmetric airfoil shape including camber.

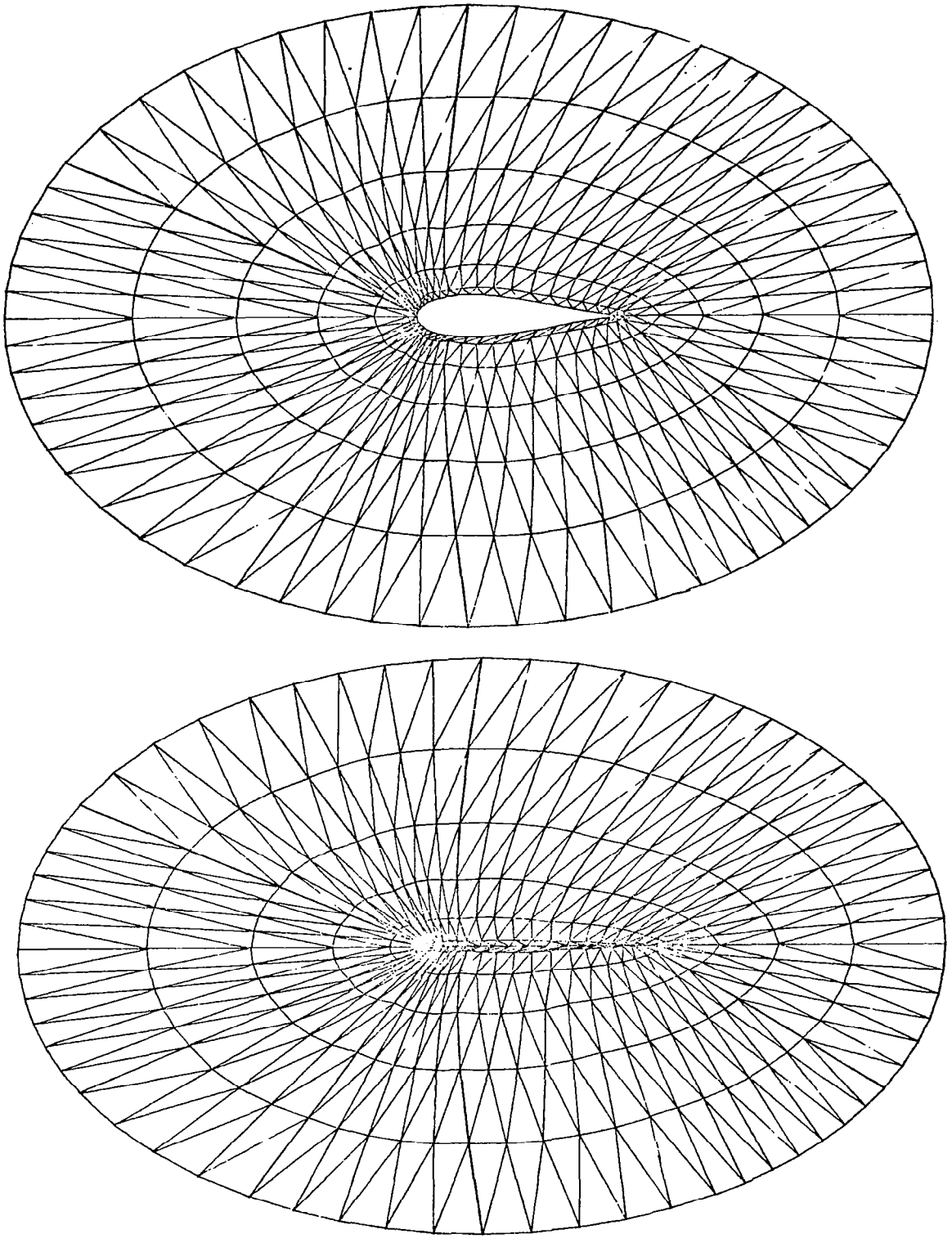

Fig. 11. Finite Element Discretizations for Joukowski Airfoil, t/C = 0.24 and t/C = 0.0

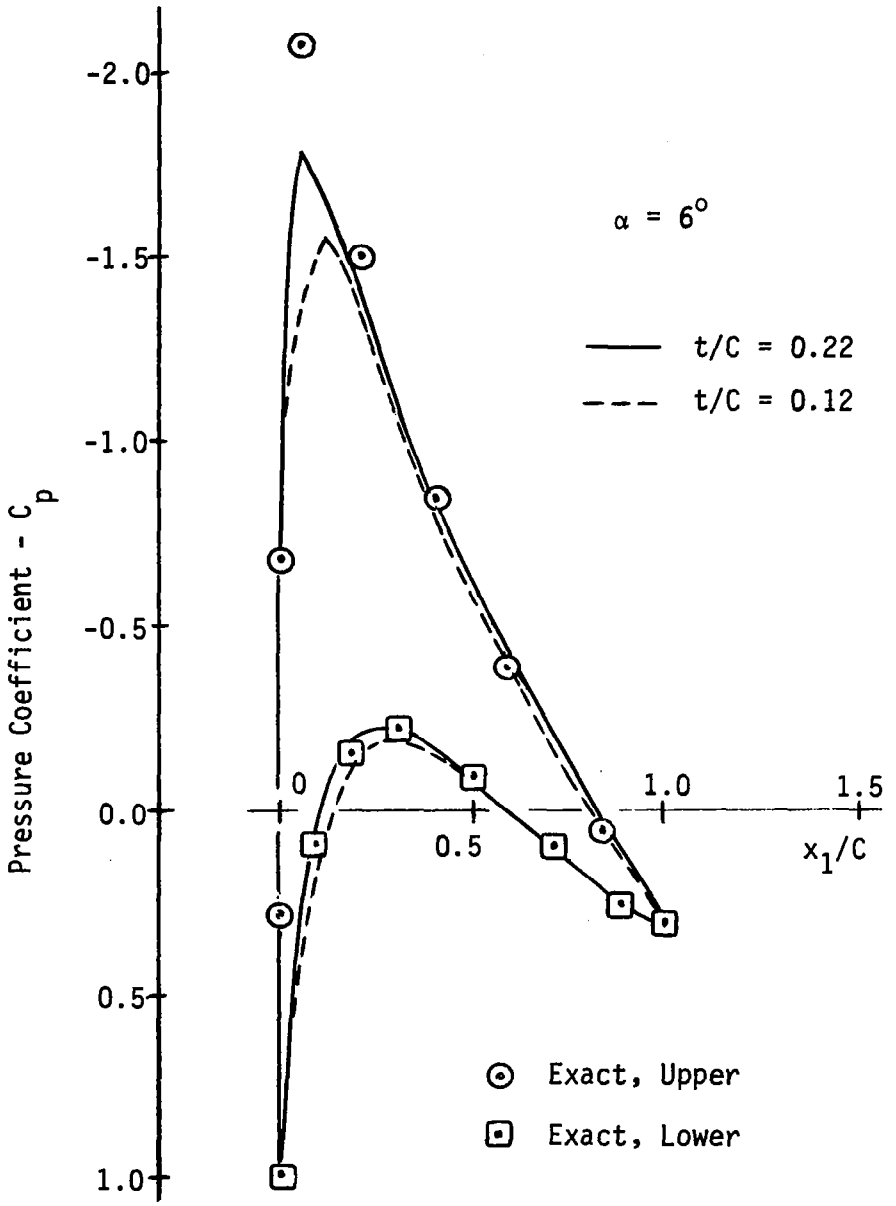

Fig. 12. Computed Pressure Coefficient Distributions on Joukowski Airfoil, t/C = 0.22 Nominal

Boundary Layer Flow

A numerical test program was employed to ascertain the accuracy and convergence character of finite element prediction of turbulent two-dimensional boundary layer flows using the 2DBL option in the COMOC computer program. Emphasis was placed on assessing the influence on accuracy and computer cost of finite element discretization and refinement, turbulence closure modeling, and initialization procedures for required data profiles. The comparison bases were computed mean flow longitudinal velocity ($\tilde{u}_1$) profiles, the familiar boundary layer integral parameters of displacement thickness (δ^*) and momentum thickness (θ), and the point norms of shape factor (H), boundary layer thickness (δ), and skin friction (C_f). For reference, these definitions are

$$\delta^* \equiv \int_{\delta} [1 - \tilde{u}_1 u_e^{-1}] dx_2 \tag{87}$$

$$\theta \equiv \int_{\delta} \tilde{u}_1 u_e^{-1} [1 - \tilde{u}_1 u_e^{-1}] dx_2 \tag{88}$$

$$H \equiv \delta^* \theta^{-1} \tag{89}$$

$$\delta \equiv \{x_2 | \forall x_2 \ , \ \tilde{u}_1 u_e^{-1} = 0.991\} \tag{90}$$

$$C_f \equiv \tau_w \left(\tfrac{1}{2} \rho_e u_e^2\right)^{-1} \tag{91}$$

where x_2 is the coordinate normal to the aerodynamic surface, u_e is the local freestream velocity, and τ_w is the wall shear stress. Each of the defined parameters is a function of x_1, the longitudinal (streamwise) coordinate. Furthermore, for three-dimensional parabolic or boundary layer flows, each also depends upon the lateral coordinate x_3. The Ludweig-Tillman formula (ref. 6) for C_f is valid for laminar, transitional and turbulent flows, and is determined from θ and H as

$$C_f = 0.246(10)^{-0.678H} Re_\theta^{-0.268} \tag{92}$$

In equation ('92), Re_θ is the momentum thickness Reynolds number

$$Re_\theta \equiv \frac{u_e \theta}{\nu_e} \tag{93}$$

Four test cases were selected to facilitate the study. The turbulent flow test cases were taken from data sets published in the Stanford conference proceedings (ref.26). The Wieghardt flat plate flow (IDENT 1400) corresponds to equilibrium turbulent boundary layer development at zero pressure gradient. Constant freestream velocity ($U_\infty = u_e$) was 33 m/s, the flow was tripped at the blunt leading edge by a trip wire, wind tunnel turbulence level was 0.25%, and the average unit Reynolds number was 2.19×10^6 per meter. The Bradshaw relaxing flow (IDENT 2400) corresponds to evolution of a non-equilibrium boundary layer, induced by abrupt removal of a moderate adverse pressure gradient from an initially equilibrium flow. Nominal freestream velocity (U_∞) was 33.5 m/s, wind tunnel turbulence was less than 0.1%, and the reference unit Reynolds number was 2.38×10^7 m^{-1}. The Newman adverse pressure gradient flow (IDENT 3500) corresponds to turbulent boundary layer flow approaching separation on the upper surface of an airfoil at angle of attack. Nominal reference velocity (U_∞) was 36 m/s, wind tunnel turbulence level was approximately 1%, and the reference unit Reynolds number was 2.5×10^6 m^{-1}. Finally, the zero pressure gradient, laminar incompressible (Blasius) similarity solution (ref. 6) was employed to assess absolute accuracy and validate numerical convergence for the finite element discretizations determined economically accurate for turbulent flow prediction.

The two-dimensional boundary layer equation system solved by the 2DBL option in COMOC is established in a transformed coordinate system. Coordinate stretching in the x_2 direction can efficiently compensate for bounday layer thickness growth. Referring to Figure 13 , the selected transformation is

$$\eta \equiv \frac{x_2 - f_1(x_1)}{(f_2(x_1) - f_1(x_1))/f} \tag{94}$$

where η is the normalized coordinate lying between (at least) piecewise continuous surfaces, $f_1(x_1)$ and $f_2(x_1) > f_1$, that bound the elliptic solution domain R, see equation (77), and f is a normalizing factor. For the presented results, f_1 corresponds to the plate surface and is a constant, while f_2 is appropriately specified for each case. (Note that for the Blasius case, $f_2(x_1) = C\sqrt{x_1}$ would exactly scale the finite element-spanned domain to that of the similarity solution. However in COMOC, f_2 is retained in complete generality as piecewise linear interpolation between input data points, or as an input functional.)

The boundary layer equations are a sub-set of the parabolic Navier-Stokes system, equations (72)-(73). For two-dimensional flows, $\tilde{u}_2$ is determined from equation (72) and $\tilde{u}_1$ is solved from equation (73) for $i = 1$, $1 \leq j \leq 2$ and $\ell = 2$. Equations (58)-(59) are solved for the TKE closure modeling (if used) over the same index range. In expanded form in the

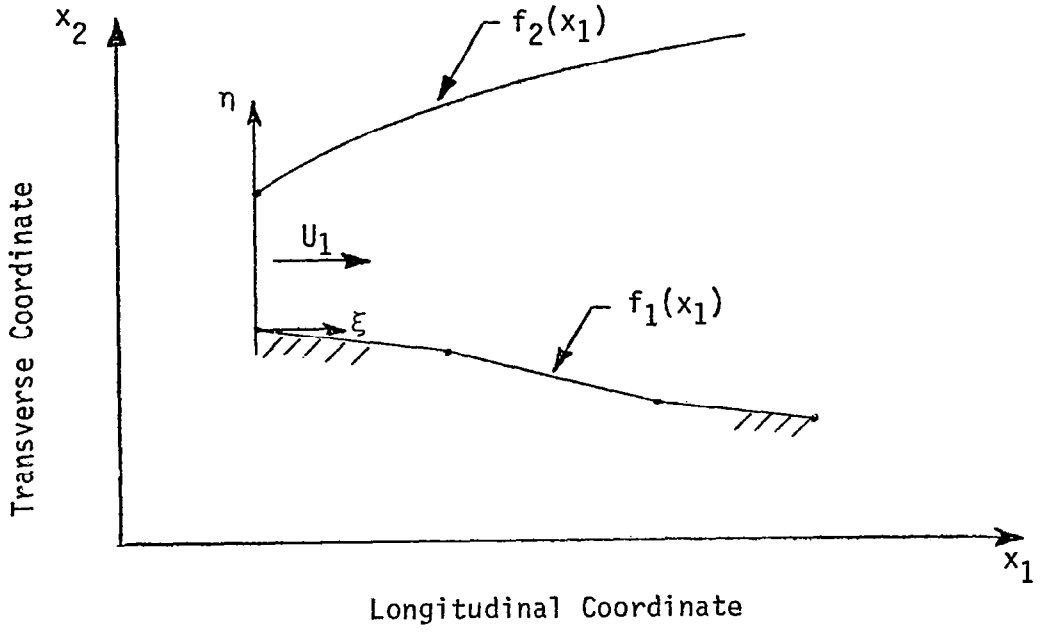

Fig. 13. Transformed Coordinate System

(ξ,n) coordinate system, and applying the incompressible boundary layer order of magnitude simplification, the equations solved are

$$L(\tilde{u}_2) = \left[\frac{\partial}{\partial\xi} - (h_2 + \eta h_3)\frac{\partial}{\partial\eta}\right]\tilde{u}_1 + \frac{\partial\tilde{u}_2}{\partial\eta} = 0 \tag{95}$$

$$L(\tilde{u}_1) = \tilde{u}_1\left[\frac{\partial}{\partial\xi} - (h_2 + \eta h_3)\frac{\partial}{\partial\eta}\right]\tilde{u}_1 + \tilde{u}_2\frac{\partial\tilde{u}_1}{\partial\eta} \tag{96}$$

$$- \frac{\partial}{\partial\eta}\left[\nu^e h_1\frac{\partial\tilde{u}_1}{\partial\eta}\right] - \frac{1}{\bar{\rho}}\frac{dp_e}{d\xi} = 0$$

$$L(k) = \tilde{u}_1\left[\frac{\partial}{\partial\xi} - (h_2 + \eta h_3)\frac{\partial}{\partial\eta}\right]k + \tilde{u}_2\frac{\partial k}{\partial\eta} \tag{97}$$

$$- \frac{\partial}{\partial\eta}\left[\frac{\nu^e h_1}{Pr_k}\frac{\partial k}{\partial\eta}\right] - \nu^e\left(\frac{\partial\tilde{u}_1}{\partial\eta}\right)^2 + \varepsilon = 0$$

$$L(\varepsilon) = \tilde{u}_1\left[\frac{\partial}{\partial\xi} - (h_2 + \eta h_3)\frac{\partial}{\partial\eta}\right]\varepsilon + \tilde{u}_2\frac{\partial\varepsilon}{\partial\eta} \tag{98}$$

$$- \frac{\partial}{\partial\eta}\left[\frac{\nu^e h_1}{Pr_\varepsilon}\frac{\partial\varepsilon}{\partial\eta}\right] - C_\varepsilon^1\varepsilon k^{-1}\nu^e\left(\frac{\partial\tilde{u}_1}{\partial\eta}\right)^2 + C_\varepsilon^2\varepsilon^2 k^{-1} = 0$$

The functions h_i, $1 \leqslant i \leqslant 3$, are the metric coefficients which result from differentiation in the curvilinear coordinate system defined in equation (94). Members of the set are defined as

$$h_i \equiv \begin{Bmatrix} f(f_2 - f_1)^{-1} \\ f_1' h_1 \\ h_1(f_2' - f_1')f^{-1} \end{Bmatrix} \tag{99}$$

The superscript prime denotes ordinary differentiation with respect to ξ. The effective kinematic diffusion coefficient is (see equation 70).

$$\nu^e = Re^{-1}\nu + \nu_t \tag{100}$$

where

$$\nu_t \equiv \begin{cases} \omega^2 \ell^2 \left| \frac{\partial \tilde{u}_1}{\partial x_2} \right| & \text{(MLT)} \\ C_\nu k^2 \varepsilon^{-1} & \text{(TKE)} \end{cases} \qquad (101)$$

and ν is the kinematic molecular viscosity. For the MLT closure, ℓ is the mixing length and ω is the Van Driest damping coefficient (ref. 17), see equations (61)-(62).

As the key feature of turbulent flow computations, it is mandatory to employ a highly non-uniform (finite element) discretization of R to obtain satisfactory computational efficiency in concert with acceptable solution accuracy. Following extensive numerical tests, it was determined that solution speed and accuracy were enhanced in concert by using a finite element discretization that increased in sequential span according to a geometric progression. For two-dimensional parabolic flows, the finite element domain R_m is a line segment of measure (length) L_m. If $\eta_{m=1}$ represents the extremum nodal coordinate of R_m, i.e., the $m^{\underline{th}}$ finite element domain spans

$$L_m \equiv \eta_{m+1} - \eta_m \qquad (102)$$

then a geometric progression of η_{m+1} (hence span of R_m) is obtained by the recursion relation

$$\eta_{m+1} = \eta_1 + s \sum_{j=2}^{m+1} \rho^{j-2} \qquad 1 \leq m \leq M \qquad (103)$$

In equation (103), η_1 is the coordinate of the first node of the discretization (typically zero, i.e., $x_2 = f_1(x_1)$, equation (94)) ρ is the progression ratio of the finite element span, s is a scale factor that allows imbedding a given number of elements within $f_2 - f_1$, equation (94), and M is the total number of finite elements spanning R, equation (77). Numerical experimentation was conducted for

$$10^{-3} \leq s/\delta \leq 10^{-1}$$
$$1 \leq \rho \leq 1.5$$

where δ is the boundary layer thickness. Note that $\rho = 1$ corresponds to a uniform discretization. Shown in Figure 14 are graphs of discretizations as established by equation (103) for several s/δ and ρ. Curves A, C and D illustrate various uniform discretizations of R; the header shows the corresponding number of finite elements M spanning δ and 3δ, whereat appropriate

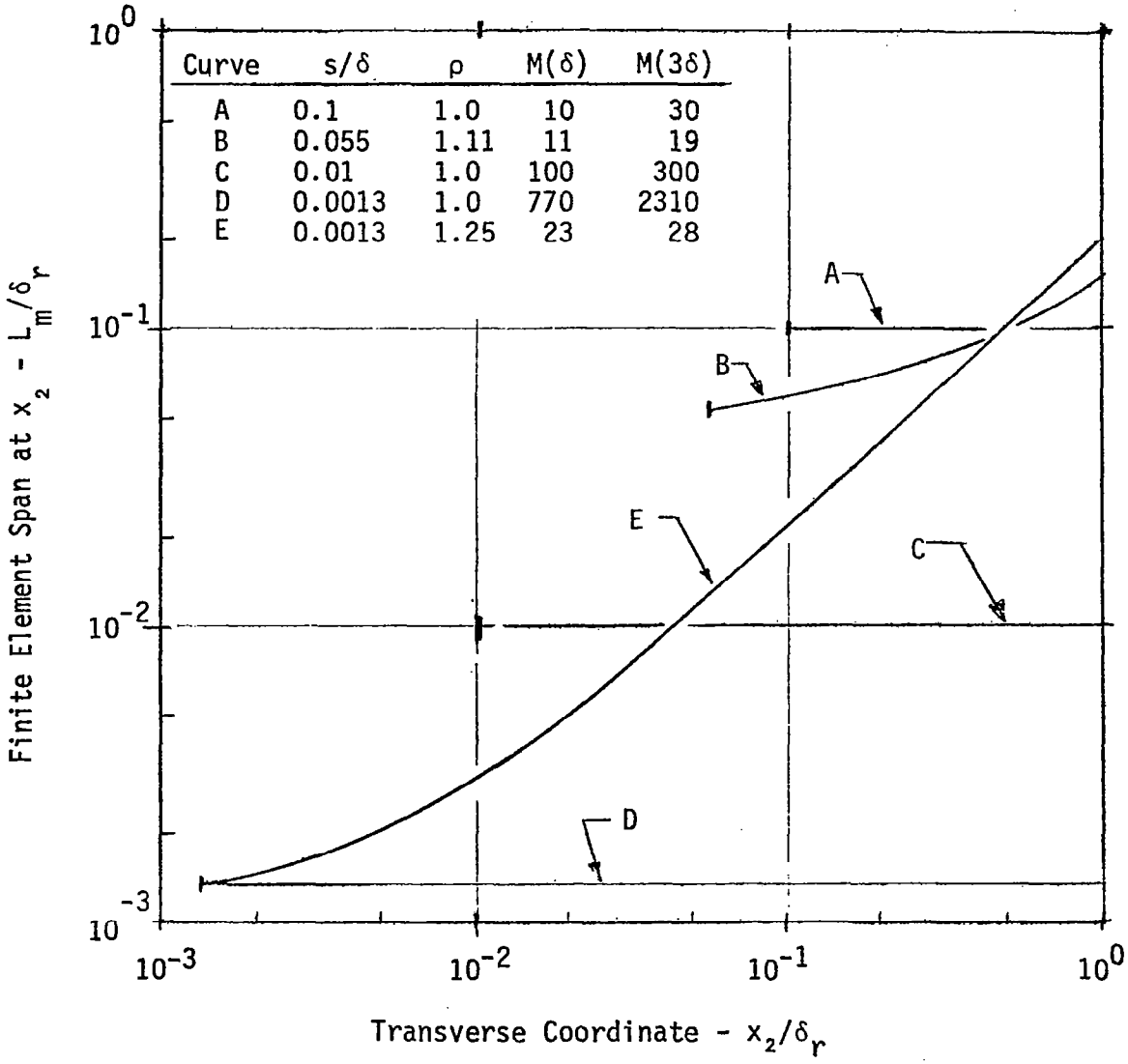

Fig. 14. Finite Element Boundary Layer Discretizations

freestream boundary conditions for each computed variable were applied. Curve B illustrates a modestly non-uniform grid, suitable for laminar flow predictions, obtained for $\rho = 1.11$. Compared to curve A, resolution at the wall is doubled, while only about two-thirds the number of elements is required to span the solution domain, $R = 3\delta$. Curve E depicts a typical finite element discretization determined by numerical experiment to yield good solution accuracy for turbulent flow predictions while requiring only minimal computer execution time. The finite element at the wall spans $\delta \times 10^{-3}$, yielding excellent resolution of near wall damping, yet only about 28 finite elements are needed to span $R = 3\delta$. Progression ratios $\rho > 1.25$ generally yielded a too sparse discretization in the freestream. Values of ρ appreciably less than 1.25 can place double the number of elements within 3δ. Barring the numerical round-off error associated with finite arithmetic, finer discretization always improves accuracy for a consistent algorithm. However, for the turbulent flows tested, the improvement in accuracy was typically inadequate to compensate for the doubling of computer CPU time. Hence, the following results were obtained using the discretization shown as curve E, Figure 14

The results for the Wieghardt data case (IDENT 1400) are presented in Figures 15-16. As shown in Figure 15 the computed $\tilde{u}_1$ velocity profiles are in excellent agreement with data at each of the first eight experimental stations. Closure for turbulence was accomplished using MLT, with the parameters κ and λ equated to their standard values of 0.435 and 0.09 respectively. For boundary conditions, both $\tilde{u}_1$ and $\tilde{u}_2$ vanished at the plate surface, while $\partial\tilde{u}_1/\partial x_2$ vanished at the freestream boundary, $x_2 = 3\delta$. Shown in Figure 16 are comparisons between data and the finite element predictions for the boundary layer parameters. Agreement is excellent throughout, except for skin friction C_f, where measureable disagreement is noted over $0 \leq x_1 \leq 0.25$m. However, within this range, the experimental data is extremely sparse; note the lowest symbol for $\tilde{u}_1$ on each data profile in Figure 15, corresponding in each case to the first measured value. Since C_f is basically the wall shear stress τ_w, its evaluation is highly sensitive to the employed interpolation formulae (see comments, ref. 26, Vol. II, p. 98).

The computed solution was initialized in a manner identical to experiment wherein a turbulence-free uniform flow was forced to impinge upon the plate leading edge. For the numerical solution, the initial value of $\tilde{u}_1$ at each node of the finite element discretization was thus uniformly U_∞, except for the node at the plate surface where $\tilde{u}_1 = 0$ throughout. Hence, the maximum attainable velocity gradient occurred at solution initiation; nevertheless, start-up by COMOC was smooth and devoid of oscillation. The initial values for $\tilde{u}_2$ were uniformly zero since $\partial\tilde{u}_1/\partial x_1 = 0$ upstream of the plate. This corresponds to what is termed a "slug-start," which is the method employed to initiate solutions in the absence of any preferable alternative. Since the turbulent Reynolds number of the Wieghardt case is initially small, transition from laminiar to turbulent flow occurs over a finite span of x_1, up to and including perhaps the first data station. The results of computational experiment with the switch from laminar to turbulent flow is shown in Figure 17

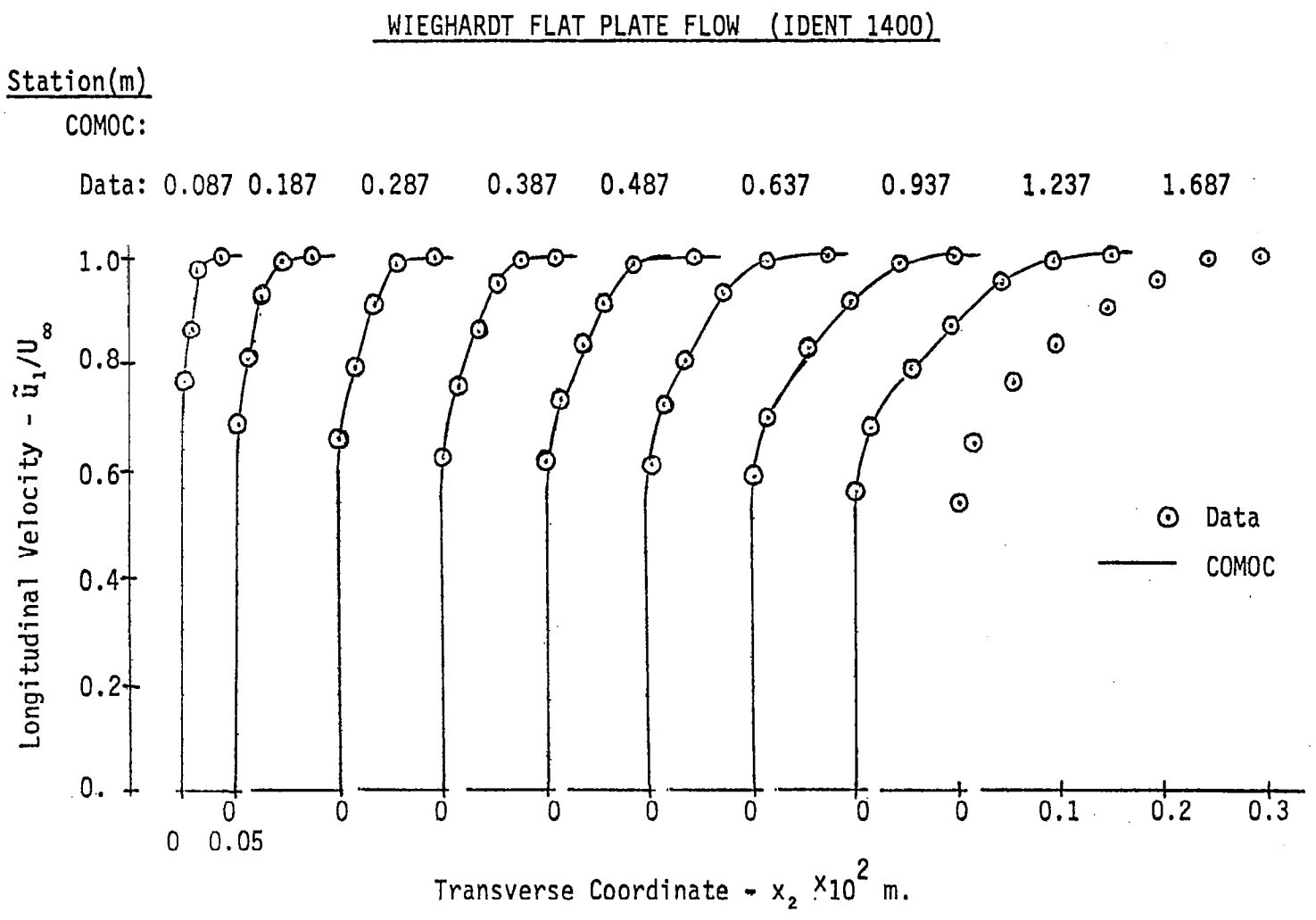

Fig. 15. Longitudinal Velocity Profiles, Wieghardt Flat Plate Flow, MLT.

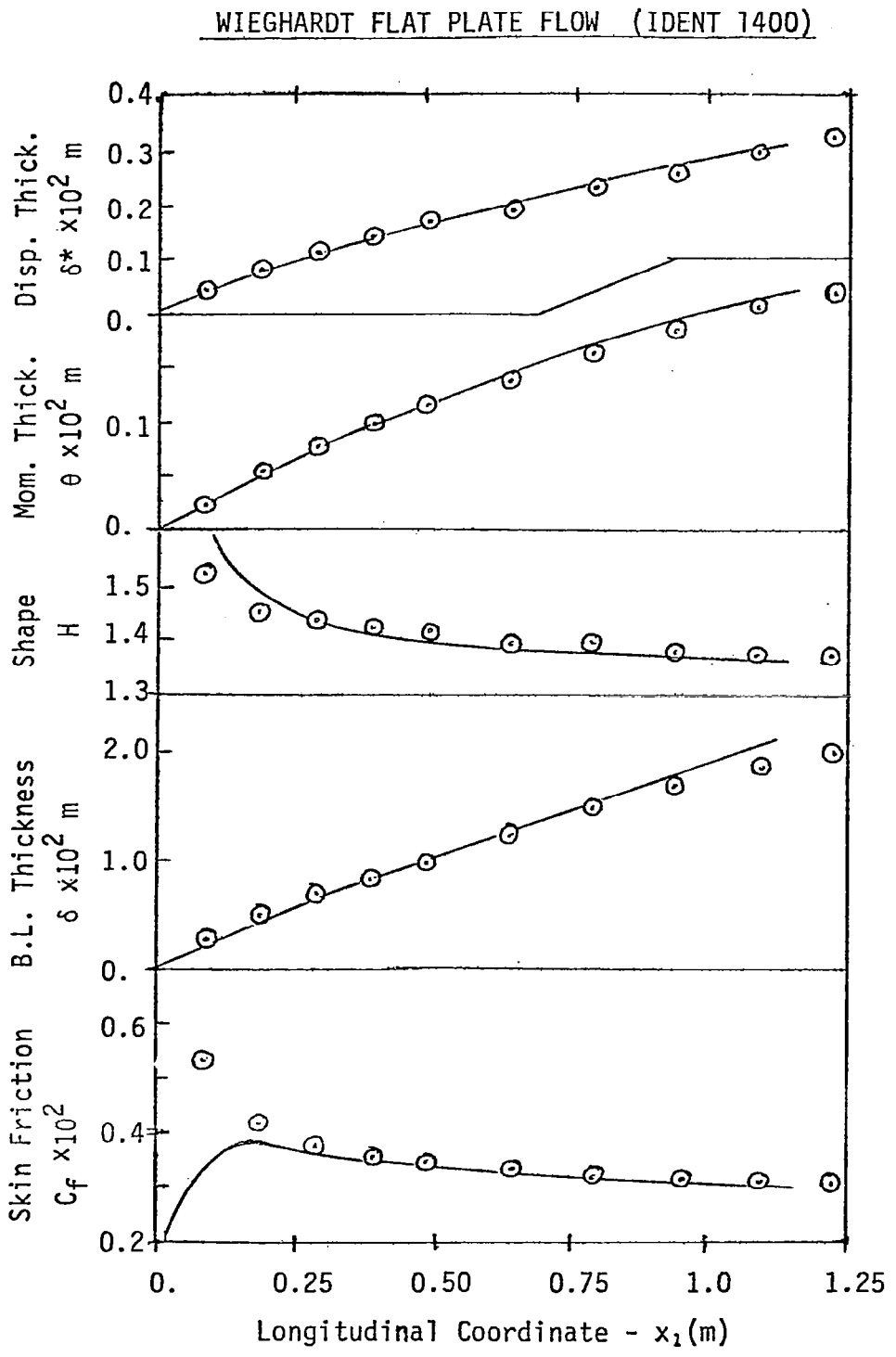

Fig. 16. Boundary Layer Parameters, Wieghardt Flat Plate Flow, MLT

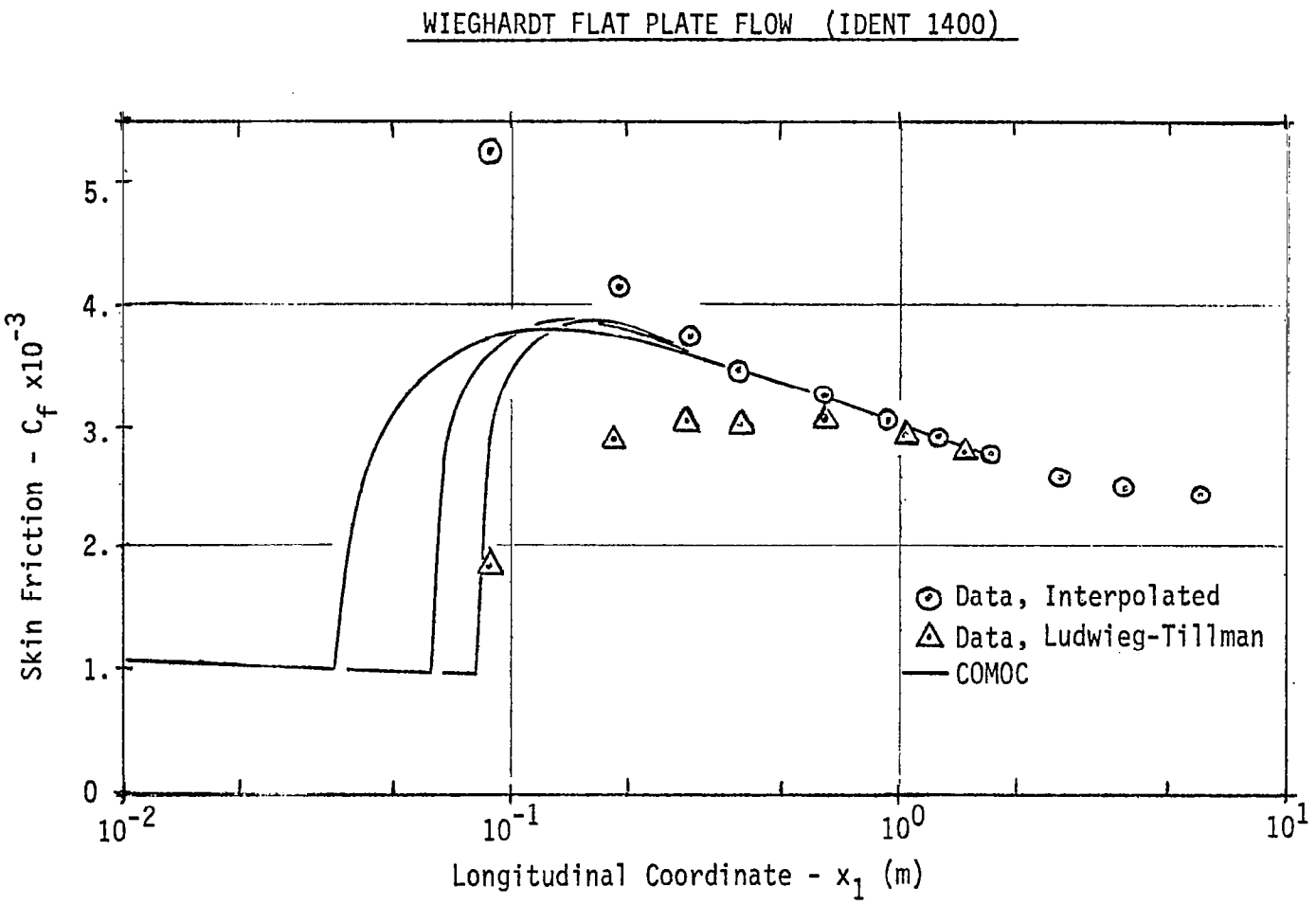

Fig. 17. Transition Location Influence on Skin Friction, Wieghardt Flat Plate Flow, MLT

The symbols correspond to C_f as established from Wieghardt data using both an interpolation procedure (ref. 26) and the Ludweig-Tillman formula, equation (A.6). The curves were determined from the $\tilde{u}_1$ profiles computed by COMOC using equation (A.6). In each case the flow was assumed laminar to the selected transition point after which computation of the MLT eddy viscosity was initiated and continued as the flow proceeded downstream. No transition model was employed to alter the intermediate profiles. The family of computed results are bracketed by the data, and by $x_1 = 0.6$m the various methods are in essential agreement. The velocity profiles shown in Figure 15 were taken from the run which predicted $\tilde{u}_1$ at $x_1 = 0.087$ m in agreement with the first experimental value ($\tilde{u}_1 U_\infty^{-1} \simeq 0.77$).

The second turbulent flow test case is considerably more demanding, since nonequilibrium phenomena are involved in the relaxation process. Turbulence generation and dissipation processes are not in balance at a point in the flow; hence, one expects MLT to be of marginal validity while the TKE closure should be more exact. Nevertheless, MLT with standard coefficient values proved remarkably capable as illustrated by the detailed $\tilde{u}_1$ velocity comparisons in Figure 18 These results were generated using a fixed coordinate system since boundary layer growth was rather modest for this case. Agreement with data is good, although diffusional processes within the flat mid-range appear too high as evidenced by the computed results uniformly exceeding the data. These differences diminish further downstream, but there is a corresponding trend for the computed results to under-predict the first knee in the curve. Shown in Figure 19 is comparison between prediction and data on the boundary layer parameter bases. As suggested in reference 26, match with the data has been enforced at the second station. Agreement in θ , H and δ is generally excellent. The correct trends and local extrema in δ^* are predicted; however, the overall level of the curve is high. In concert with the underprediction of C_f, these curves are in agreement with the computed low $\tilde{u}_1$ profiles near the wall. Note that the increasing wall shear in a uniform pressure field is a manifestation of the non-equilibrium processes. Turbulence levels for this case are high as well. For example, see equation (100), the computed extremum of ν^e/ν for the Wieghardt case was 150, while for Bradshaw it was 900. However, for both cases, the employed non-uniform discretization provided adequate resolution of the wall region while using only 29 elements to define the range of extremum turbulent viscosities encountered.

The Bradshaw case was employed to assess correct operation of the TKE closure model for turbulence in COMOC in concert with MLT to predict near wall effects. Several tests were run to evaluate an optimum y+ to apply fixed boundary conditions for solution of k and ε, equations (97)-(98), where y+ is the familiar Reynolds number based upon u_τ , equation (67), i.e.

$$y^+ \equiv \frac{u_\tau x_2}{\nu} \qquad (104)$$

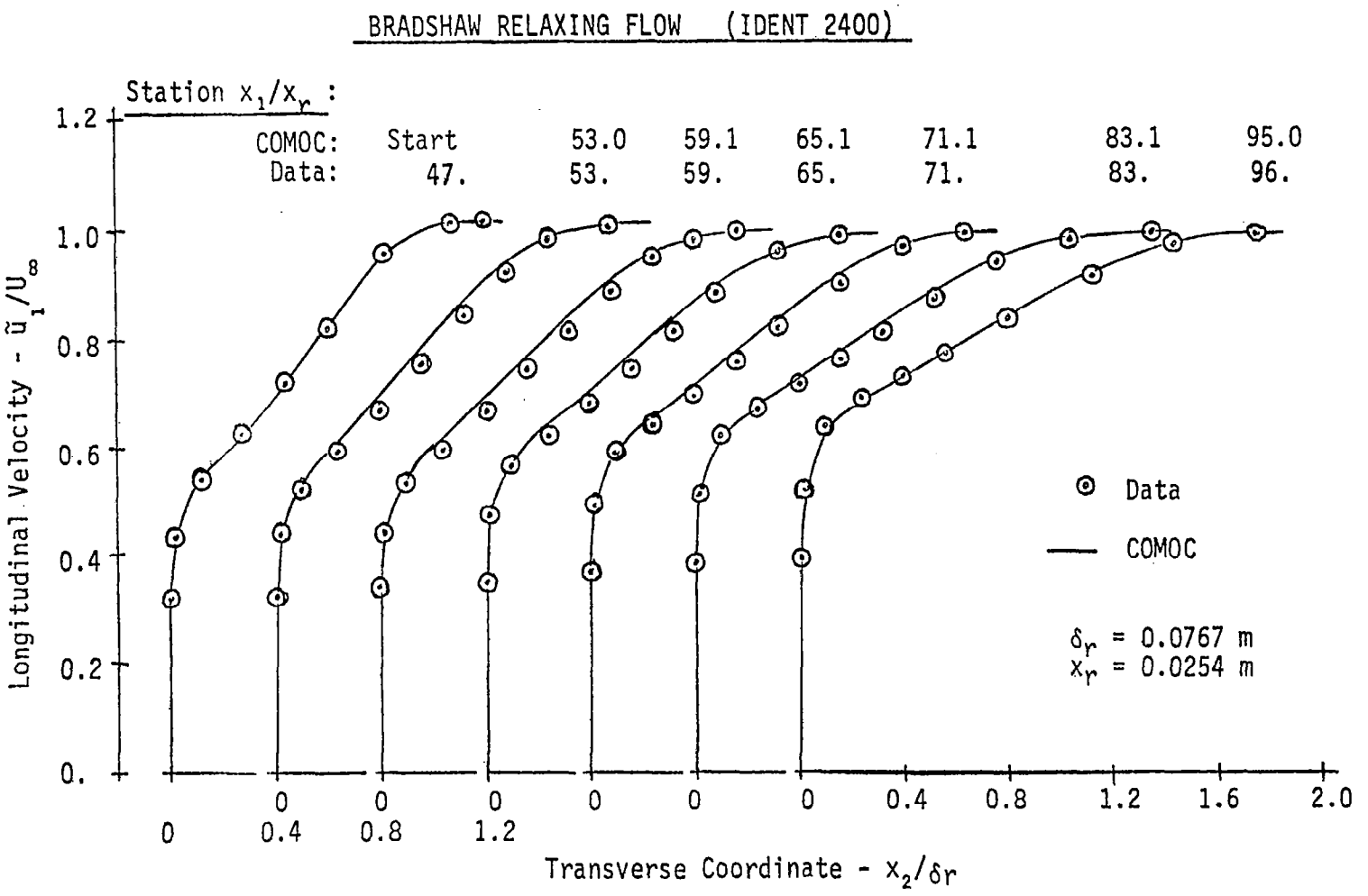

Fig. 18. Longitudinal Velocity Profiles, Bradshaw Relaxing Flow, MLT

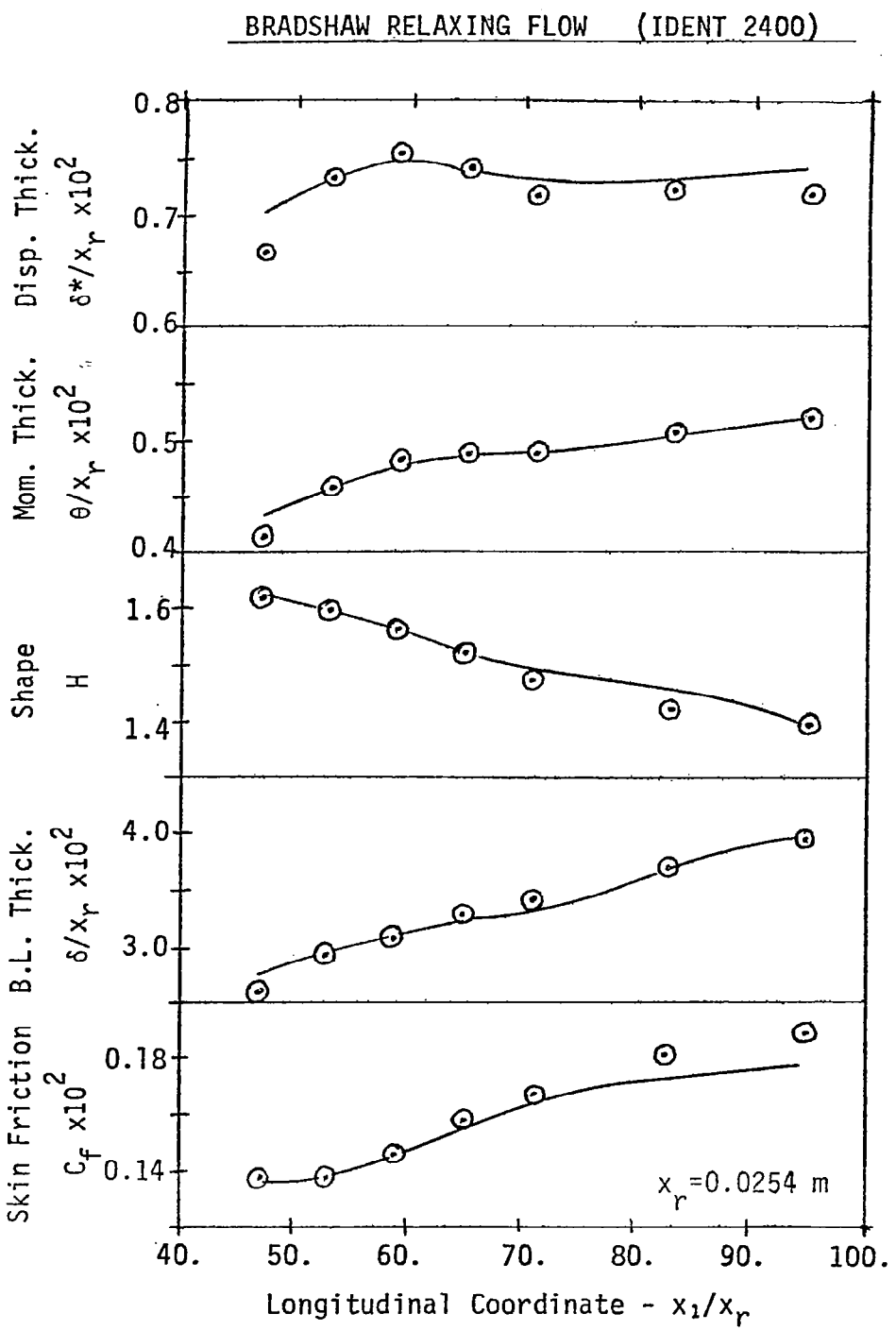

Fig. 19. Boundary Layer Parameters, Bradshaw Relaxing Flow, MLT

Initial profiles for k and ε, to start the solutions, were determined from the $\tilde{u}_1$ profiles using the dual definition of ν_t, equation (101), in concert with the definition of a dissipation length scale, ℓ_d.

$$\ell_d = k^{3/2}\varepsilon^{-1} \tag{105}$$

and the knowledge that ℓ_d can be interpolated quadratically between known wall and freestream values (0 and 0.09, respectively), and that $\partial\ell_d/\partial x_2$ at the wall is linear and known (e.g., see ref. 21). The range evaluated was $7 \leq y^+ \leq 50$, and best results for this case occurred for $30 \leq y^+ \leq 40$. Shown in Figure 20 are comparisons between computational results for $\tilde{u}_1$ and data; agreement is good and comparable to the MLT run. Figure 21 presents comparisons for the boundary layer parameters. Agreement of computed δ^* and θ with data is noticeably poorer for $x_1 > 71$, but otherwise in essential agreement with the trends noted for the MLT runs.

The evaluation of the Newman adverse pressure gradient case (IDENT 3500) indicates limitations of the boundary layer and mixing length concepts. This flow corresponds to upper surface boundary layer development on an airfoil at angle of attack sufficient to induce separation before the trailing edge. Using the standard values for the constants in MLT, $\kappa = 0.435$ and $\lambda = 0.09$, and the previously verified non-uniform discretization, numerical evaluation indicated that the computed eddy viscosity was excessively large, since the velocity profile shape near the wall was considerably less retarded than the experimental data. Retardation of the boundary layer at freestream was correctly computed. Since the adverse pressure gradient acts as a sink for momentum across the entire boundary layer, i.e., it is a uniform solution-insensitive non-homogeniety in the differential equation, the only means to under-decelerate the wall profile is for the high freestream momentum to cascade into the low momentum region. Since $\tilde{u}_2 \ll \tilde{u}_1$, the sole mechanism producing this phenomena is an excessively large diffusion coefficient, μ^e. Since some latitude exists for λ, a value near its lower bound (0.07) was evaluated. The results of this prediction are shown in Figure 22, which compare computed $\tilde{u}_1$ velocity profiles to data over a one meter span. Agreement is excellent up to the last two profiles; over diffusion progressively erodes this agreement thereafter and the separation imminent at the last data station is not captured. This results directly from excessive momentum diffusion to the wall. For example, shown for comparison as the dashed curve is one velocity profile computed for $\lambda = 0.09$. For this case, the extremum μ^e/μ was 820; for $\lambda = 0.07$ at the same station, maximum μ^e/μ was 650. However, this level increased to 850 by the last data station, resulting in the indicated poor agreement. The comparison of computed integral parameter distributions to data is shown in Figure 23. Agreement is excellent up to the imminent separation. Thereafter, only δ agrees well with data, indicative of correct simulation of the pressure gradient effects using the vanishing gradient freestream $\tilde{u}_1$ boundary condition. This type of boundary layer

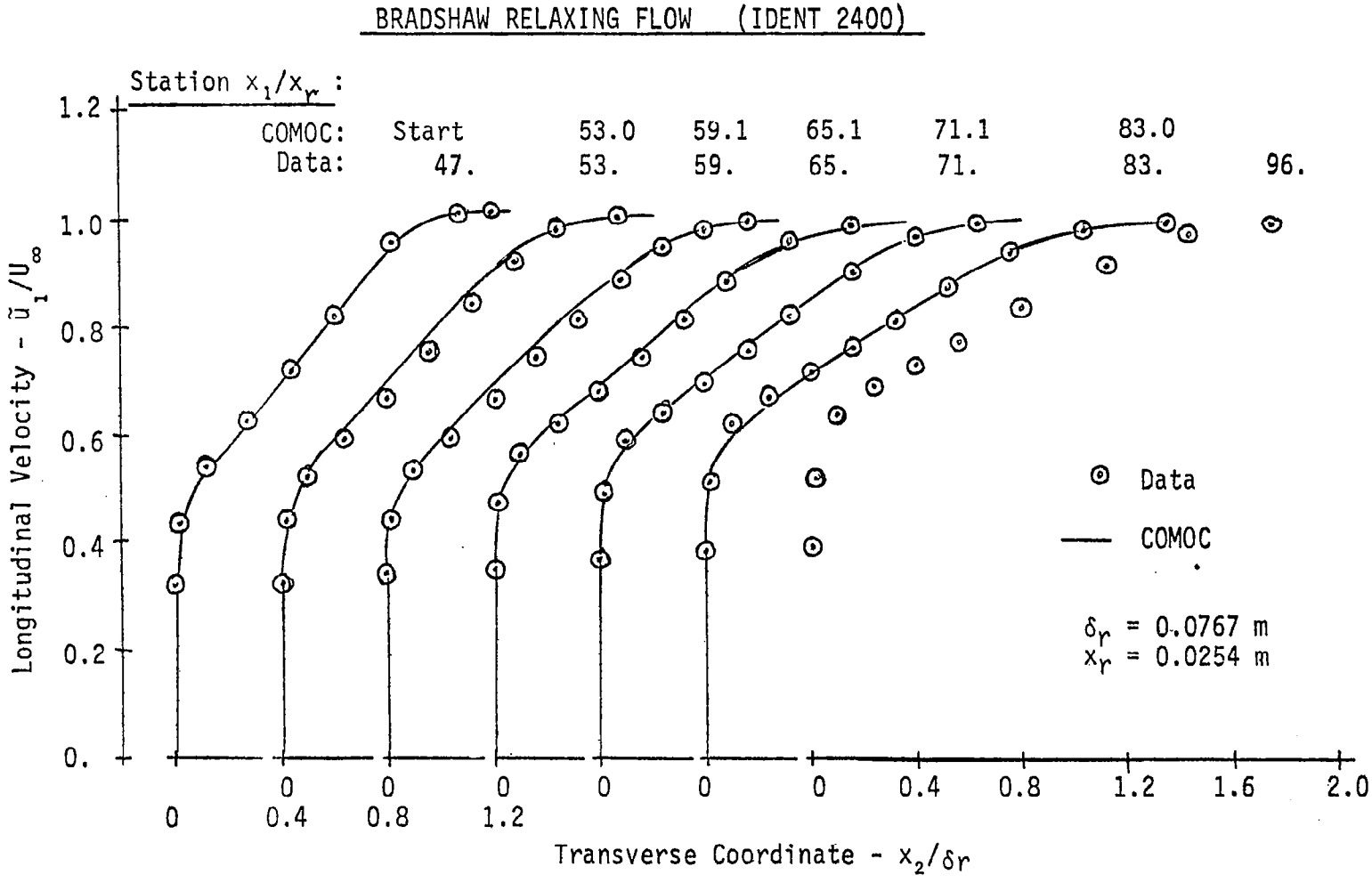

rig. 20. Longitudinal Velocity Profiles, Bradshaw Relaxing Flow, TKE

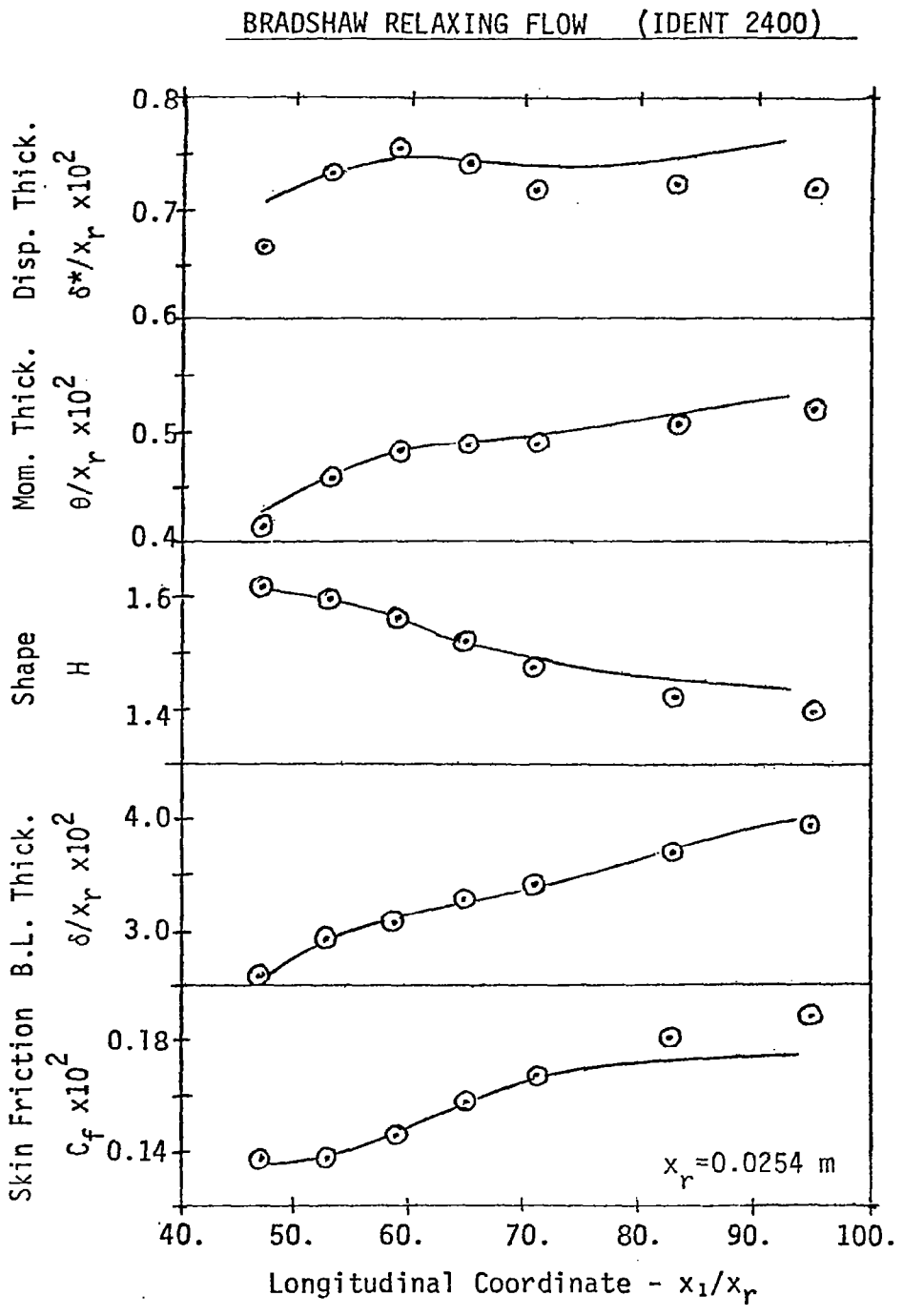

Fig. 21. Boundary Layer Parameters, Bradshaw Relaxing Flow, TKE

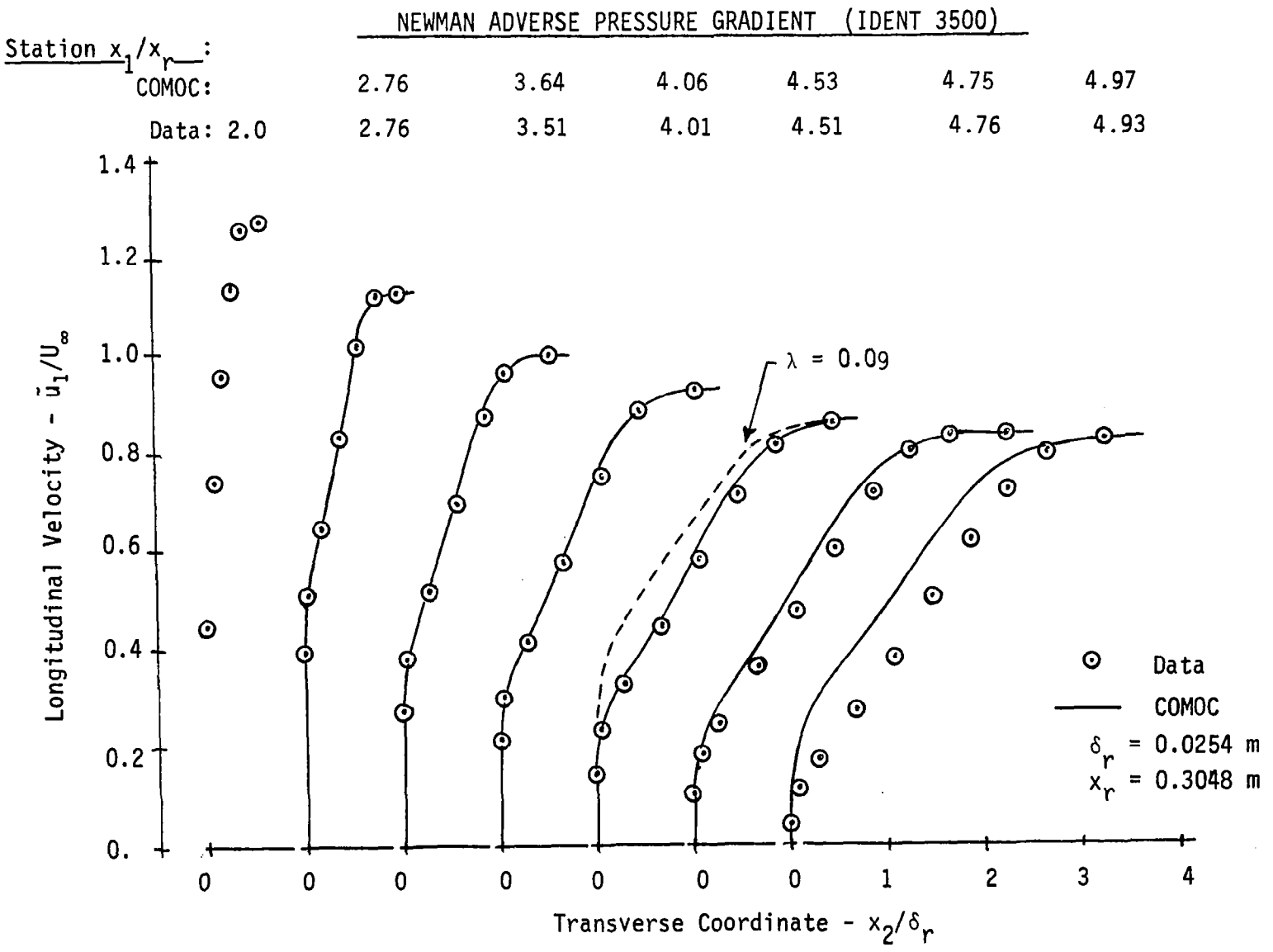

Fig. 22. Longitudinal Velocity Profiles, Newman Adverse Pressure Gradient Flow, MLT

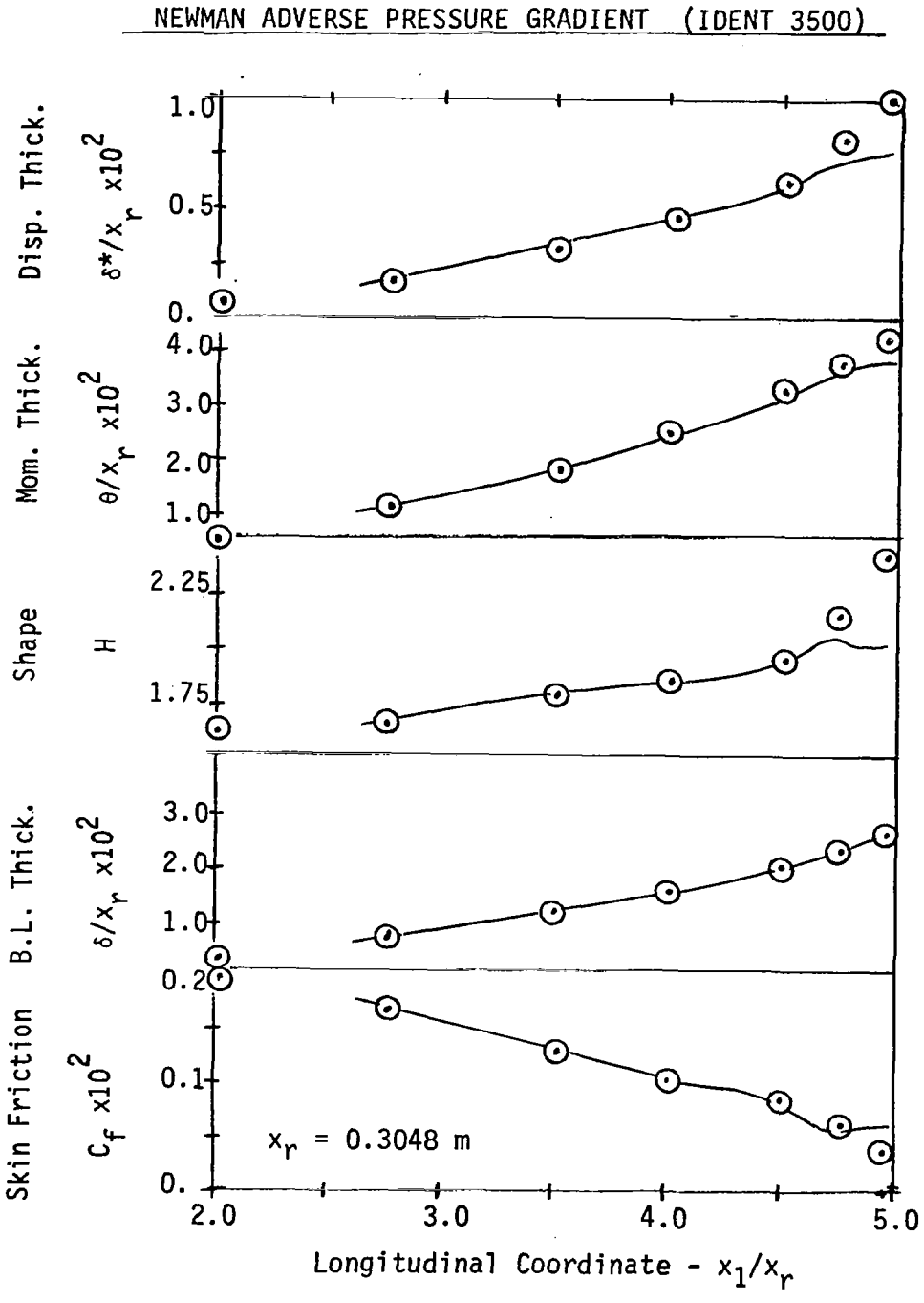

Fig. 23. Boundary Layer Parameters, Newman Adverse Pressure Gradient Flow, MLT

situation is always encountered near the trailing edge of practical airfoil flows. Careful attention to detail is therefore required, including perhaps use of a higher-order closure model for turbulence like TKE.

Absolute accuracy and convergence character of the finite element algorithm at this point can only be determined by computation of laminar flows. The Blasius solution (ref. 6) provides the required exact solution to equations (95)-(96) for ν equal to a constant. Use of a nominal 10 element uniform discretization, curve A of Fig. 14, produces a maximum error in $\tilde{u}_1$ of about 1.5%. The non-uniform discretization of the same number of elements, curve B, reduces this error by a factor of about four, as does a doubling of the uniform discretization to 20 elements. The latter results confirm that the linear functional finite element algorithm is of second-order accuracy. It is also noted that use of the variable stretched coordinate option, equation (94), degrades absolute accuracy for laminar flows by up to a factor of two. The culprit appears to be the continuity equation solution, which as a direct consequence of the transformation contains a term that is linear in η . Hence, it grows without bound as equation (95) is solved. Use of the Blasius solution for $\tilde{u}_2$, in concert with integration of equation (96) for $\tilde{u}_1$ is determined to remove the additional error. This phenomena appears of negligible influence for computation of turbulent boundary layers for the cited test cases, provided sufficient resolution of the region near freestream is retained. Recall that large finite elements are therein employed; use of coordinate stretching can induce a too coarse discretization near freestream for computations of sufficient length.

Turbulent Wake Flow

Prediction of the merging of dissimilar turbulent boundary layer profiles, downstream of the terminus of the airfoil, requires solution of the 2DPNS equation system closed with the TKE model. The primary requirement in this solution is to accurately predict the rapid reduction in boundary layer displacement thickness, defined now as the sum of the upper and lower surface contributions, as the viscous flows merge. In an interaction solution these data will reflect back into the potential flow solution as alteration of the effective inviscid shape of the airfoil and its wake. The equilibration process will occur very rapidly within about 0.1C downstream and will locally generate large levels of turbulence in the initial momentum—defect region. Within this span, the initially zero $\tilde{u}_1$ at the trailing edge will rapidly accelerate to 50 - 60% of U_∞ . As the flow proceeds further downstream, the momentum defect within the wake will continue to slowly diminish.

From the aerodynamics standpoint, the output of primary value for the wake flow is prediction of the drag due to friction. An analytical exact expression for drag can be derived from the integral momentum equation (cf., ref. 6). For an incompressible flow, the form is

$$\frac{1}{\theta}\frac{d\theta}{dx} = \frac{\tau_w}{\theta \rho_e \tilde{u}_{1e}} - (2+H)\frac{d}{dx}\left(\ell n \frac{\tilde{u}_{1e}}{U_\infty}\right) \qquad (106)$$

where θ and H are parameters defined in equations (88)-(89). In the absence of a wall, this equation is formally integrable by parts, yielding

$$\theta_\infty = \theta \left[\frac{\tilde{u}_1}{U_\infty}\right]^{H+2} \exp\left[\int^{H} \ell n \frac{U_\infty}{\tilde{u}_{1e}} \, dH\right] \tag{107}$$

where θ and H may be evaluated at any x_1 coordinate. The trailing edge has been chosen, typically, since most interaction solutions have available only the boundary layer parameters up to this location. Evaluation of equation (107) requires $\tilde{u}_{1e} = \tilde{u}_{1e}(H)$. In the Squire-Young approximation (cf., ref. 27), a linear relation in the logarithm is chosen. The resultant drag coefficient is

$$C_D = 2 \frac{\theta}{C} \left[\frac{\tilde{u}_1}{U_\infty}\right]^{1/2(H+5)} \Bigg|_{\text{upper + lower}} \tag{108}$$

where θ and H are evaluated at the trailing edge. The Squire-Young approximation is at best only marginally valid between the trailing edge and downstream infinity. However, its use may be of greater value if the transition from the trailing edge to some nearby downstream station could be more accurately predicted, i.e., numerically. Then equation (108) could be employed to complete the computation of C_D for the remainder of the wake.

The basic requirement, therefore, is to use the 2DPNS solution to compute the near wake. The Joukowski airfoil test case was employed since experimental data base exists (ref. 28). The measured $\tilde{u}_1$ boundary layer profiles were interpolated to provide an initial condition for the 2DPNS equations. Starting at $x_1/C = 0.98$, the 2DBL option in COMOC was run using MLT, then the TKE closure to equilibrate the $\tilde{u}_1$ and computed $\tilde{u}_2$ profiles with the imposed C_p. At $x_1/C = 1.00$, a restart was used to switch to the 2DPNS option. This solution was then marched downstream to $x_1/C = 1.25$. Shown in Figure 24 is the comparison between $\tilde{u}_1$ distributions and $\tilde{u}_2$ distributions computed by the finite element 2DPNS. Agreement is excellent to $x/C = 1.10$; thereafter, the upper profile is progressively underdiffused. Note that the wake is modestly curved, as defined by the trajectory of $\tilde{u}_1$ minimum. While the velocity differences are only a few percent, the impact on integral parameters is pronounced as shown in Fig. 25 for the upper profiles at $x_1/C \geq 1.1$. The lower profile integral parameter solution is in good agreement with data as are both shape factor contours and the acceleration of the $\tilde{u}_1$ minimum. Shown in Fig. 26 are computed wake distributions of turbulence kinetic energy and dissipation. Assuming the validity of equation (47), the TKE profiles correspond to pressure variation across the boundary wake. The initial levels are modest with a double peak. They coalesce into a significant extremum, immediately downstream of the trailing edge, with higher levels maintained thereafter, coincident with a gradual broadening of the base. These results verify the fundamental capability of the finite element solution of the 2DPNS equations to accurately predict the merging of dissimilar turbulent boundary layer profiles within the wake downstream of a sharp trailing edge. The results are applicable to both establishment of a weak-interaction solution algorithm as well as prediction of viscous drag.

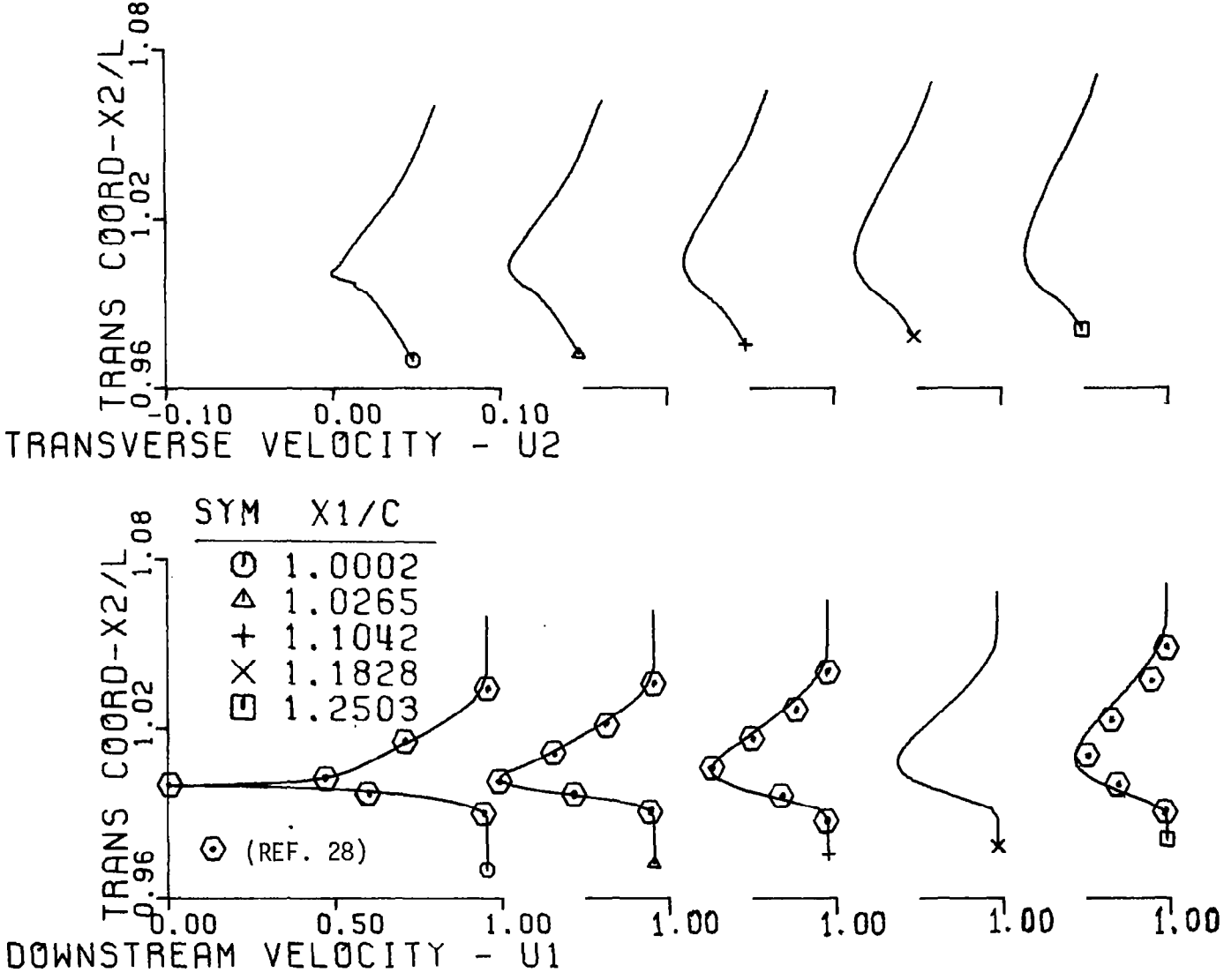

Fig. 24. Longitudinal and Transverse Mean Flow Velocity Profiles in Wake Downstream of Joukowski Airfoil, $\alpha = 6^{o}$

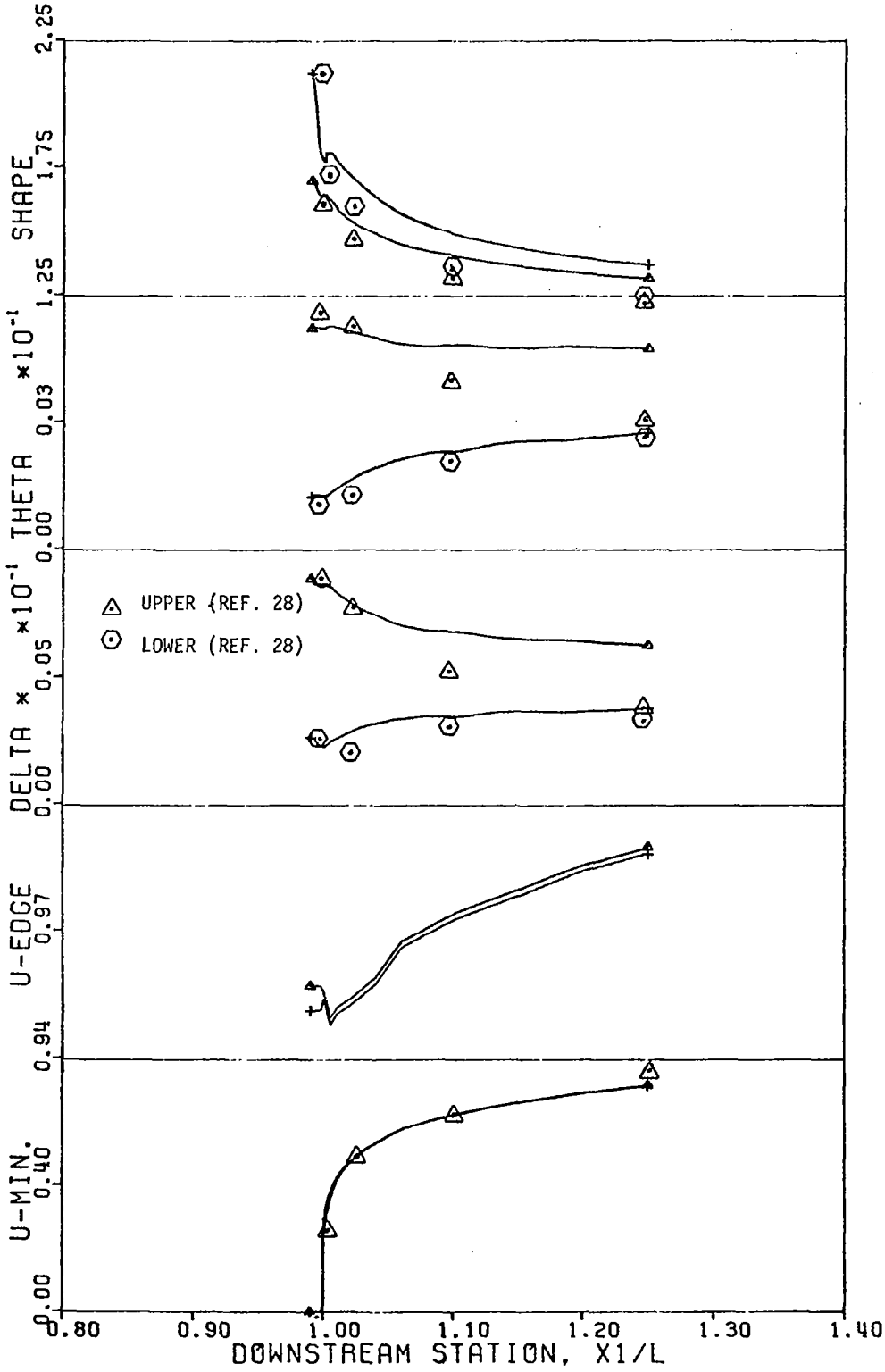

Fig. 25. Integral Parameter Distributions in Wake Downstream of Joukowski Airfoil, $\alpha = 6^{\circ}$.

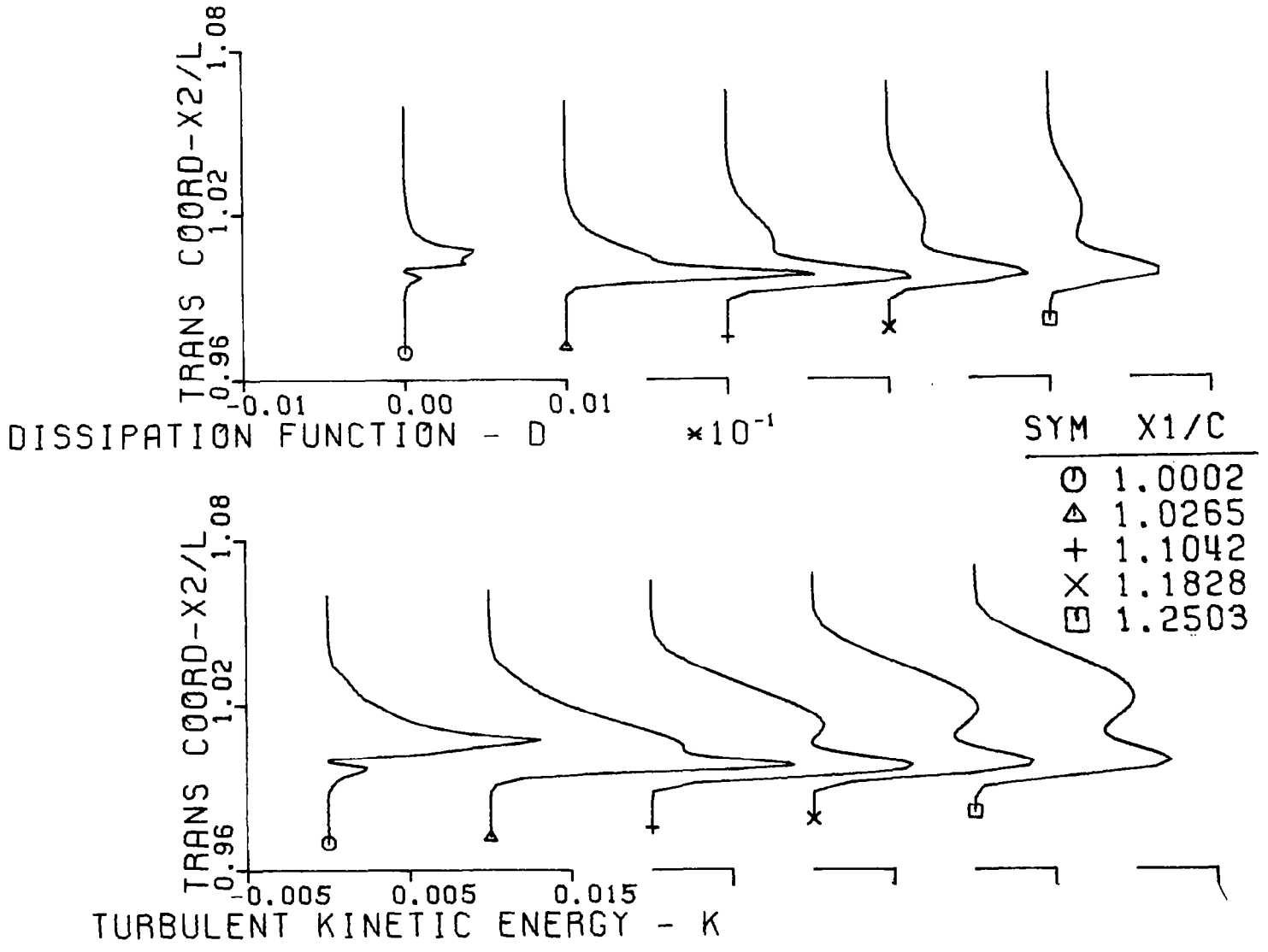

Fig. 26. Turbulence Kinetic Energy and Dissipation Profiles in Wake Downstream of Joukowski Airfoil, $\alpha = 6^{\circ}$.

An Interaction Solution

The finite element solution of the fundamental building blocks of a weak-interaction algorithm for subsonic aerodynamic flows has been documented. An evaluation of these capabilities for a complete flow solution has been completed. In this case, the airfoil contour was a modified NACA 0015, for which experimental data are available (ref. 29). Shown in Fig. 27 is the COMOC-computed C_p distribution for this airfoil at $\alpha = 8^\circ$. The computational results are in good agreement with the exact solution, including the trailing edge, where $\Delta C_p = 0.01$ between lower and upper surface. In distinction to the Joukowski, the NACA 0015 has a finite thickness trailing edge. Use of the original finite element solution-domain diagonal orientation, Fig. 7, for this case is thus observed to produce excellent results.

COMOC contains a subroutine to integrate the integral momentum form of the boundary layer equations. This solution is quite inexpensive and can yield adequately accurate determination of θ and δ^* up to the immediate vicinity of the trailing edge, i.e., $x_1/C \leq 0.9$. The upper and lower surface C_p distributions computed by COMOC for the basic airfoil were employed to compute the initial estimate of δ^* distributions. The trailing edge values were then faired into a representative freestream decay, and the potential flow determination repeated for this viscous-augmented shape. This C_p distribution is also shown in Fig. 27, denoted "augmented (0)," ie., the zeroth iteration. Note the pronounced blunt base introduced at the airfoil trailing edge by the viscous effects, with an attendant sharp slope discontinuity in proceeding into the wake.

Also shown in Fig. 27 is the δ^* distribution computed from the initial (inviscid) computed C_p and that of the first iteration. The results at the trailing edge differ remarkably, with the upper surface peak in δ^* moving upstream from the airfoil terminus. The iterative cycle between viscous-augmented potential flow and integral boundary layer and wake was continued until convergence was achieved, defined as $\Delta C_p \leq 1\%$ of the maximum C_p. The final results for C_p and δ^* computed consistent are also shown in Fig. 27. The latter curve is in essential agreement with experimental data (ref. 29).

This converged C_p distribution is then employed to drive a 2DBL and 2DPNS solution from upstream of the trailing edge on into the turbulent wake. Computations are continued to $x_1/C \simeq 1.15$, whereafter δ^* and θ can be assumed to vary only slowly to the end of the computational domain. The computed modifications to δ^* within the interval $0.9 \leq x_1/C \leq 1.15$ are then employed to modify the effective inviscid airfoil shape. The finite element determination of potential flow may then be repeated if sufficient difference is computed for δ^* from the more exact solutions. The 2DPNS wake flow solution is also used to evaluate drag, equation (107).

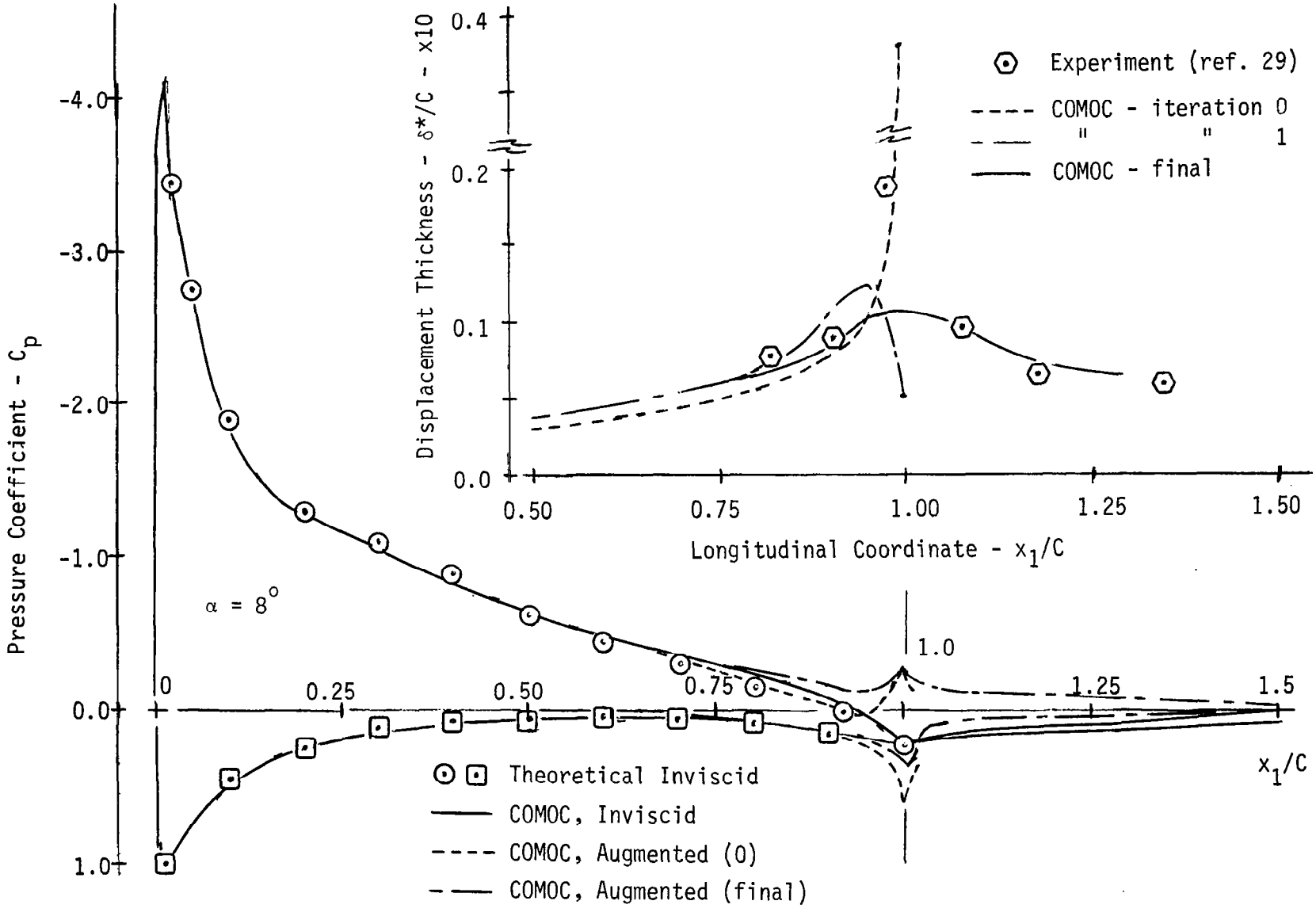

Fig. 27. Computed Pressure Coefficient Distribution on Modified NACA 0015 Airfoil

CONCLUDING REMARKS

The results of the reported comprehensive numerical experimentation document the basic capabilities of finite element solution of the differential equation systems constituting two-dimensional weak-interaction theory in aerodynamics. Factors affecting solution accuracy for potential flow determination about an isolated elementary airfoil have been evaluated. An algorithm for accurate computation of pressure coefficient is established. A highly non-uniform discretization has been determined to allow economically-accurate prediction of two-dimensional turbulent boundary layer flows with pressure gradient. Comparisons have been made with experimental data using both MLT and TKE closure for turbulence. The prediction of turbulent merging of dissimilar turbulent boundary layer profiles has been accomplished in the wake downstream of a sharp airfoil trailing edge. The ability to combine these analyses into a weak interaction solution for the complete flow about an isolated elementary airfoil has been documented.

These results confirm for the first time the fundamental capability of finite element solution methodology applied to the complete aerodynamics problem. There is ample room for improvement as well as extention to more complex airfoil systems and higher dimensional space. A systematic numerical experimental project should be persued to evaluate under close control the factors affecting accuracy of computed potential function and derived pressure coefficient. A higher-order, curved-sided finite element might prove economically useful to more accurately model airfoil surface and wake curvature. The accuracy of the turbulent boundary layer and merged wake flow solutions could be enhanced through turbulence model refinement as well as use of higher order accurate finite element functionals and initial-value integration procedures. Each of these areas could and should be addressed to render tangible the potential usefulness of the finite element solution in subsonic aerodynamic system design.

APPENDIX

Automatic Discretization Refinement

Combined viscous-inviscid flowfield iterative solutions impose the requirement for automatic redistribution of the potential flowfield grid points to accomodate the inviscid boundary shift at each solution iteration. The finite element size along the boundary must remain relatively constant, however, to maintain solution accuracy, hence, the entire flowfield grid must be shifted to conform to each new boundary shape. For the infinite variety of airfoil, boundary layer and viscous wake shapes encountered in aerodynamics, a method is required which is unrestricted in its ability to model general geometric shapes.

The COMOC discretizer has this capability. By subdividing the flow domain into a few shapes having quadratic variation along the boundaries, virtually any closed domain can be accurately modeled and discretized to conform to solution requirements. The method is graphically presented in Figure A.1 for a single element two-dimensional airfoil in an infinite domain. In Figure A.1a the flowfield has been divided into twelve sub-domains consisting of eight quadrilateral and four triangular shapes. The gridpoints represent the data required to specify the sub-domain boundaries. Note that all boundaries are of degree 2 or less. The side gridpoints serve to describe the curved surface shapes and their location relative to adjacent verticies determines the spacial distribution of the generated grid. Figure A.1b illustrates a 648 element grid generated from the subdomain description in Figure A.1a. Note that the refined grid around the airfoil surface and toward the leading and trailing edges is due to the off center placement of the subdomain side gridpoints. Variations on refinement type and number of elements is readily accomplished from a single set of subdomain data by simply moving side gridpoints and respecifying the number of elements for each subdomain.

The grid refinement algorithm proceeds by looping over the subdomain and generating gridpoint and finite element correction data. For each of the quadrilateral and triangular subdomain shapes, a coordinate transformation exists which maps a local natural coordinate system onto the physical plane. The general form of the required transformation for all space is:

$$x_i = Q_j\{x_j\} \quad j = 1, n \tag{A.1}$$

where n is the total number of specified grid points on each subdomain boundary and summing over repeated indices is observed. The scalar x_i consists of the gridpoint physical values of the coordinates at the i^{th} generated node. The quantity Q_j is called the shape function and contains functions of ε and η which satisfy the transformation illustrated in Figure A.2 for ε and η of the $\{x_j\}$. Equation (A.1) is valid over one-, two-, and three-dimensional cartesion space and shape factors may be derived for a variety of geometric shapes and polynomial degrees. Since the derivation procedures are well

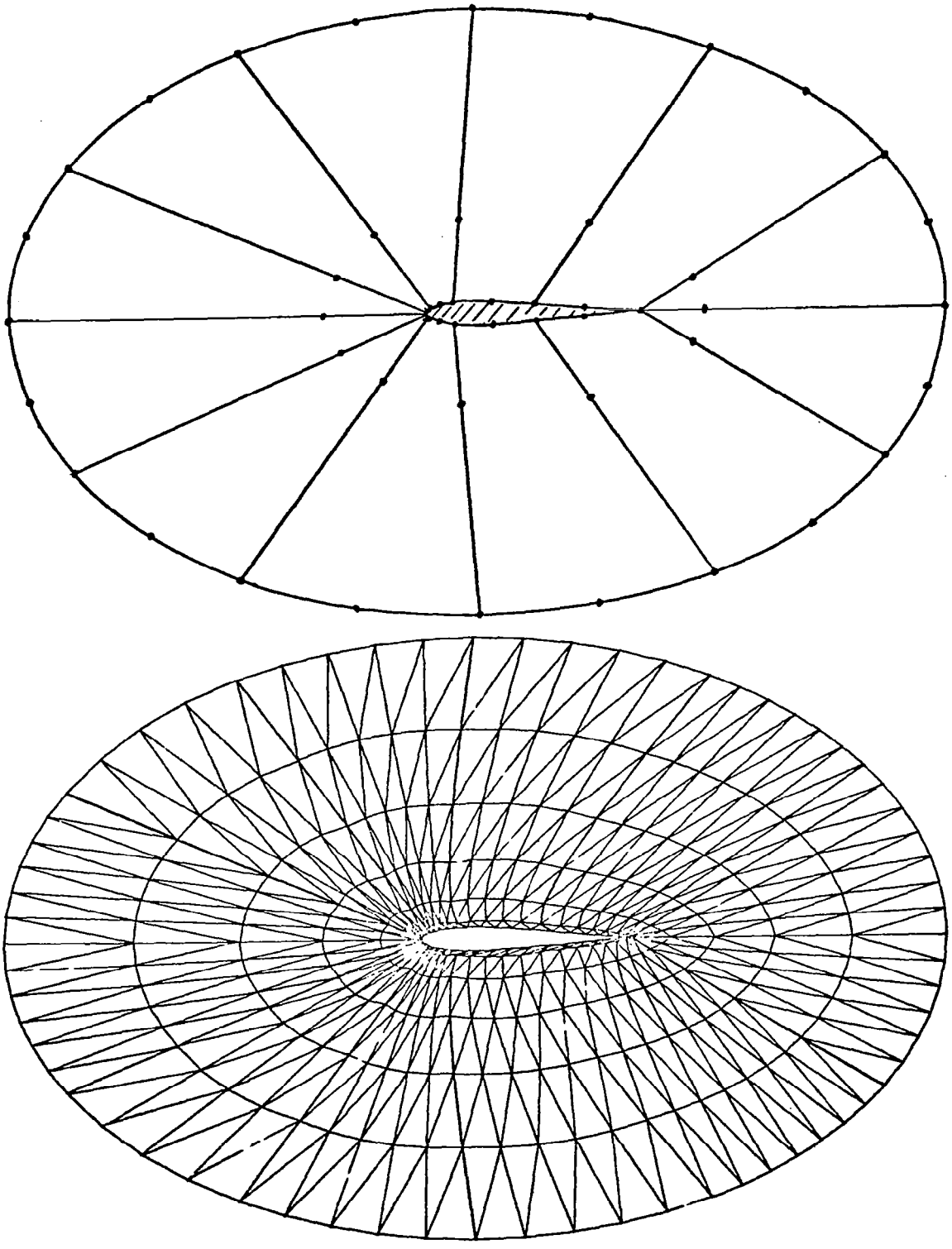

Fig. A.1. Super Element and Finite Element Discretizations For Isolated Two-Dimensional Airfoil

documented (ref. 8), the two-dimensional quadrilateral having a biquadratic (8 coef.) interpolation function will be focused upon with the understanding that other shape functions may be directly substituted. The quadrilateral shape function therefore is:

$$Q_j = \left\{ \begin{array}{l} \tfrac{1}{4}(1-\varepsilon)(1-\eta)(-\varepsilon-\eta-1) \\ \tfrac{1}{4}(1+\varepsilon)(1-\varepsilon)(\varepsilon-\eta-1) \\ \tfrac{1}{4}(1+\varepsilon)(1+\eta)(\varepsilon+\eta-1) \\ \tfrac{1}{4}(1-\varepsilon)(1+\eta)(-\varepsilon+\eta-1) \\ \tfrac{1}{2}(1-\varepsilon^2)(1-\eta) \\ \tfrac{1}{2}(1+\varepsilon)(1-\eta^2) \\ \tfrac{1}{2}(1-\varepsilon^2)(1+\eta) \\ \tfrac{1}{2}(1-\varepsilon)(1-\eta^2) \end{array} \right\}^T \qquad \text{(A. 2)}$$

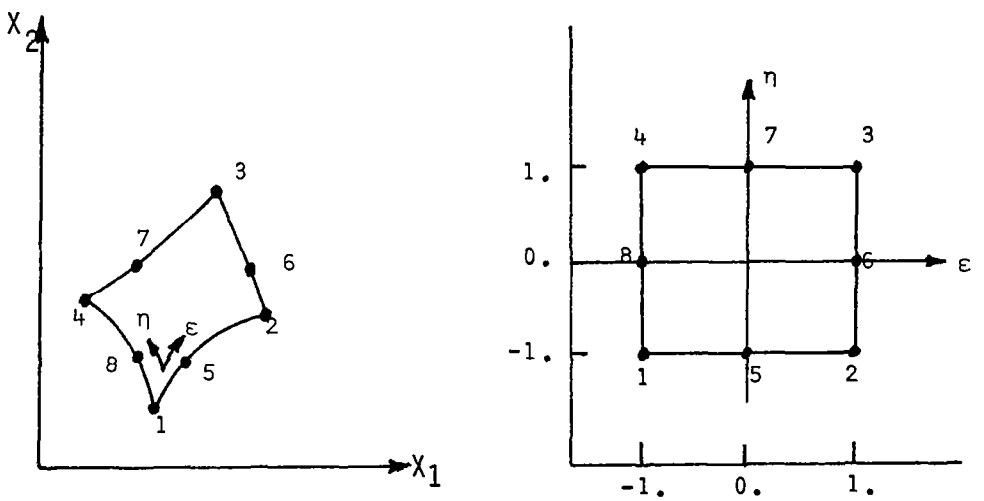

A.2a Physical Plane A.2b Transformed Plane

Fig. A.2 Mapping of a Quadrilateral Onto a Natural Coordinate Plane (ε η)

where the ε, η axis bisects the quadrilateral and the equations are ordered according to the gridpoint numbering noted in Figure A.2. Substitution of equation A.2 into A.1 for a specific set of $\{x_j\}$ and evaluating the equation over the limits of ε and η (-1 to 1) yields a biquadratic approximation to x over the subdomain. Accuracy of the values of x_j are dependent upon the ability of the shape functions to approximate the physical geometry. A curvature which is exactly biquadratic,for instance, will be interpolated exactly using equation A.2. Note in Figure A.2b that the side located grid points lie at exactly midside, by definition. The side nodes in Figure A.2a, however, need not be at exactly mid-side since it is not required in the definition of {Q}. Movement of the specification of the side nodes in the physical plane, therefore, allows for a smoothly varying distribution of generated data over the subdomain as illustrated in Figure A.1. The coordinate transformation is of the serendipity family and can yield non-unique distributions if excessive skewing of the mid-side node is attempted; therefore, care must be taken when applying the method as in Figure A.1, where regions of highly refined grid are necessary along the airfoil surface.

Each of the subdomains of which the entire solution domain is composed may be treated independently if the data generated along subdomain boundaries is identical for each subdomain. This requires that inter-subdomain boundaries share the same gridpoints and that (ε,η) be independent along the subdomain interfaces. To illustrate that this is indeed the case, consider the two coincident subdomains of Fig. A.3

Along the common boundary $(3,4,7)_1$ and $(4,1,8)_2$

$$\eta_1 = C = 1.0$$

$$\varepsilon_2 = c = -1.0$$

and evaluating equation (2) with these constraints yields:

$$Q = L\tfrac{1}{2}(\varepsilon + \varepsilon^2),\ \tfrac{1}{2}(-\varepsilon + \varepsilon^2),\ (1 - \varepsilon^2) \qquad \text{(A. 3)}$$

$$Q = L\tfrac{1}{2}(-\eta + \eta^2),\ \tfrac{1}{2}(\eta + \eta^2),\ (1 - \eta^2) \qquad \text{(A. 4)}$$

And since $\varepsilon_1 = -\eta_2$ along the boundary, equation (A.3) becomes

$$Q = L\tfrac{1}{2}(-\eta + \eta^2),\ \tfrac{1}{2}(\eta + \eta^2),\ (1 - \eta^2) \qquad \text{(A. 5)}$$

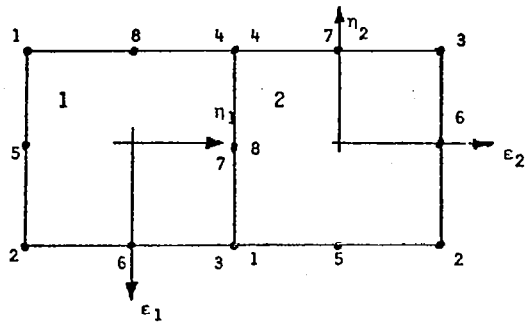

Fig. A.3 Two adjacent subdomains

which is identical to equation (A.4). Other boundary combinations and the triangular shaped subdomain can be shown to yield similar results. Three-dimensional subdomains have surface interfaces and similar equations can be derived as above where the equivalent of equation (A.5) contains functional expressions for a planar surface. This demonstrated generality, therefore, completely eliminates any requirements for specifying the subdomains in a particular order and numbering may begin at any vertex.

It is impossible to encompass the entire spectrum of geometric shape and refinement requirements within a few subdomain types. The completeness of a data refinement scheme, therefore, requires that addition to its geometric flexibility be open ended. Utilizing the subdomain method, special subdomain functions may be developed and inserted directly into the system. An example of this is a telescoping quadrilateral having quadratic interpolation. The purpose of this special function is to provide a means for increasing or decreasing the number of generated triangular elements when progressing from one end of a subdomain to another. Fig. A.4 illustrates the effect for a quadrilateral expanding from three elements per side to six elements per side. This subdomain has proven very useful for flows having small areas of high velocity gradient where a very fine mesh is required relative to the overall flowfield mesh size, and windowing-in is not practical. Fig. A.5 illustrates such a case where vortex generation at a wing tip is to be computed. Very high velocity gradients occur in the immediate area of the tip and decay rapidly. Utilizing the telescoping subdomain, the grid size is reduced from six elements per side in the tip region to two elements per side where an infinite boundary condition was applied and 64 elements were eliminated from the computational domain.

The interpolation functions described above are used to distribute the gridpoint data over each subdomain. Combining the subdomains to form the complete discretization, however, poses the problem of having duplicate sets of data along the interconnecting boundaries. Removal of the duplication is accomplished through the construction of a subdomain connection table from the specified data and interrogating it from an algorithm which operates over the subdomain boundaries. Table A.1 illustrates the connection table for the first four sub-domains of Fig. A.1. The storage requirements for the table are 2Σ(no. of subdomain sides).

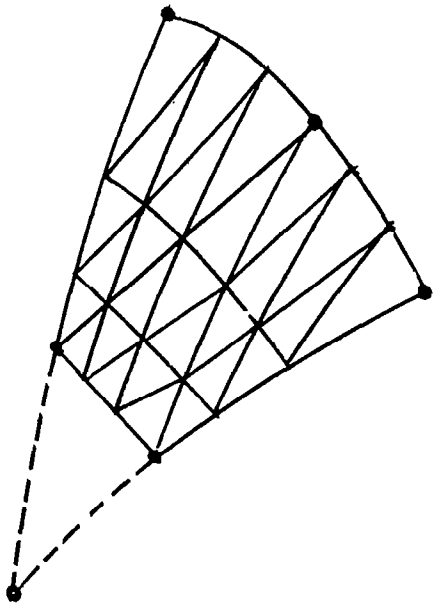

Fig. A.4 Telescoping subdomain

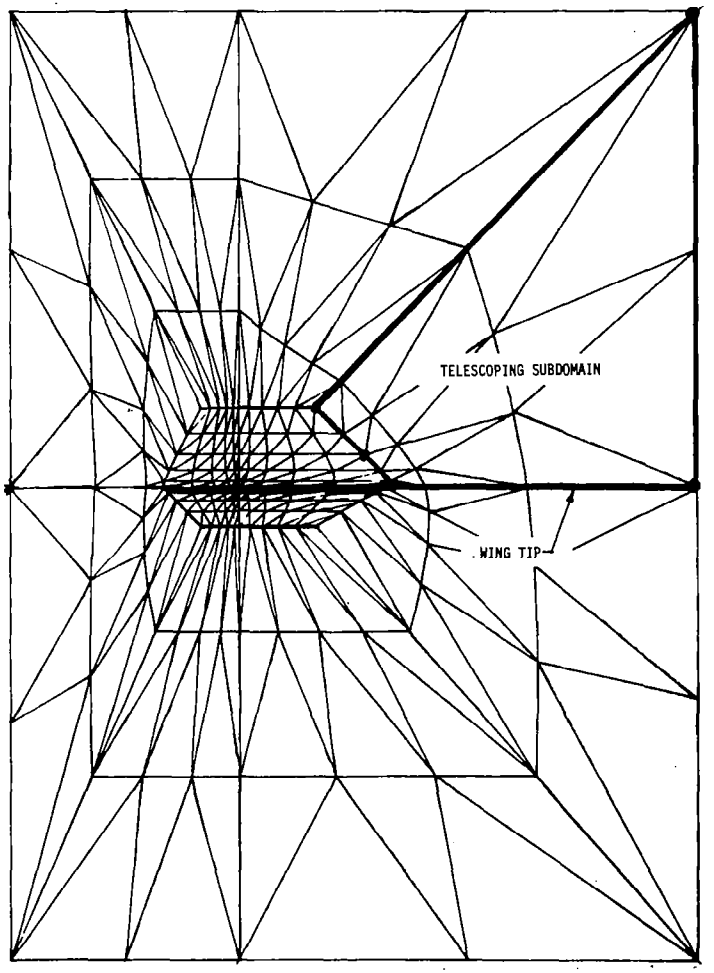

Fig. A.5 Wing tip discretization using telescoping subdomain

TABLE A.1 Subdomain Connection Table for Joukowski Airfoil. (First 4 Subdomains)

Subdomain	Side	Subdomain	Side
1	1	10	3
1	2	0	0
1	3	2	1
1	4	0	0
2	1	1	3
2	2	0	0
2	3	3	1
2	4	0	0
3	1	2	3
3	2	0	0
3	3	4	1
3	4	0	0
4	1	3	3
4	2	0	0
4	3	5	1
4	4	0	0

Note that the first two columns need not be stored since they are sequential. For the solution domain of Fig. A.1, therefore, only eighty words of storage are required to administrate boundary duplication elimination. The algorithm proceeds subdomain by subdomain, first generating a sequence of local (dummy) node numbers, then interrogating the connection table to determine if any sides are connected to any other subdomain. Upon finding one which is of lower number it retrieves the local boundary node numbers for that subdomain and substitutes them for the coincident set into the proper locations. Simultaneously, the duplicate generated variable set at the boundary is eliminated. The finite element connection table is subsequently formed for all generated elements in the subdomain and sequential global node numbering is substituted in a simple loop at the end. The connection table is also useful for locating external boundaries since they appear as zeros in the table. Note in the above scheme that only the sub-domain data was manipulated to sequence the generated data thus maintaining higher efficiency of the algorithm. Also, storage requirements are minimized by requiring operation on not more than two subdomains simultaneously, hence the data for a large problem could be generated interactively on a minicomputer or small time sharing system utilizing disk or tape intermediate storage. An especially useful feature of such a method when combined with a graphics package and a video (CRT) terminal is ability to interactively modify and debug data decks. The above scheme is very efficient and generated data for 24 variables over 10 nodes/CPU sec on an IBM 360-65.

The methodology described above requires a problem description made up of gridpoint coordinate and parametric data and also a list of gridpoint numbers on each subdomain. It has been found useful in aerodynamics to further automate data specification due to the overall similarity of the airfoil flow domains encountered. The flow domain of interest for single element airfoils is generally as shown in Fig. A.1 with variations in shape of the boundary which is small compared to the overall flow domain size. The subdomain data, therefore, is program set except for specification of airfoil and wake

coordinates. These coordinates are input in the form of a user supplied subroutine and interpolated using cubic splines to obtain coordinates at the subregion vertices The side nodes between the airfoil and in infinite boundary are automatically relocated as a function of the airfoil thickness to provide a consistant element size along the airfoil surface. Where the subroutine can be made sufficiently general to include coordinates as a function of maximum thickness ratio, etc., such as for the Karmann-Trefftz series, a wide range of shapes may be analyzed by simply respecifying the key parameters such as thickness ratio, camber, trailing edge thickness, etc. Iterative viscous-inviscid solutions are achieved by automatically adding the boundary layer and wake thickness from the viscous solution to the basic airfoil shape and proceeding through a new C_p solution. Details on using the discretizer are given in the computer program users' manual (ref. 23).

REFERENCES

1. Karemcheti, K., Principles of Ideal-Fluid Aerodynamics, John Wiley, New York, 1966.

2. Chapman, D.R., Mark, H., and Pirtle, M.W., "Computers vs. Wind Tunnels," AIAA A/A., 1975, pp. 22-30.

3. Hess, J.L. and Smith, A.M.O., "Calculation of Potential Flow About Arbitrary Bodies," in Progress in Aero. Sciences, V.8, Pergamon Press, N.Y., 1966.

4. "Aerodynamic Analyses Requiring Advanced Computers," NASA SP-347, Parts I & II, 1975.

5. "Vortex Lattice Utilization," NASA SP-405, 1976.

6. Schlichting, H., Boundary-Layer Theory, McGraw-Hill, New York, 1968.

7. Stevens, W.A., Goradia, S.H., and Braden, J.A., "Mathematical Model for Two-Dimensional Multi-Component Airfoils in Viscous Flow," NASA CR-1843, 1971.

8. Zienkiewicz, O.C., The Finite Element Method in Engineering Science, McGraw Hill, London, 1971.

9. Zienkiewicz, O.C. and Cheung, Y.K., "Finite Elements in the Solution of Field Problems," The Engineer, 1965, p. 507-510.

10. deVries, G. and Norrie, D.A., "The Application of the Finite Element Technique to Potential Flow Problems," Trans. ASME, J. App. Mech., 1971, p. 798-802.

11. Meissner, Udo, "A Mixed Finite Element Model for Use in Potential Flow Problems." Int. J. Num. Mtd. Engr., V.6, p. 467-473, 1973.

12. Isaacs, Lewis T., "A Curved Cubic Triangular Finite Element for Potential Flow Problems," Int. J. Num. Mtd. Engr., V.7, p. 337-344, 1973.

13. Vooren, J.V.D. and Laburjere, Th. E., "Finite Element Solution of the Incompressible Flow Over an Airfoil in a Nonuniform Stream," Proceedings Int. Conf. on Num. Mtd. in Fluid Dynamics, Southampton England, Sept. 1973.

14. Hirsch, C. and Warzee, G., "A Finite Element Method for Flow Calculations in Turbo-Machines," Free University of Brussels Report V.U.B-Str-5, July 1974.

15. Bratanow, T. and Ecer, A., "On the Applications of the Finite Element Method in Unsteady Aerodynamics," AIAA J., 12, No. 4, p. 503-510, 1974.

16. Ballhaus, W.F., Bailey, F.R., and Frick, J., "Improved Computational Treatment of Transonic Flow About Swept Wings," NASA CP-2001, Vol. 4, pp. 1311-1320, 1976.

17. Cebeci, T. and Smith, A.M.O., Analysis of Turbulent Boundary Layers, Academic Press, New York, 1974.

18. Tennekes, H. and Lumley, J.L., A First Course in Turbulence, The MIT Press, Cambridge, USA, 1974.

19. Launder, B.E., Reece, G.J. and Rodi, W., "Progress in the Development of a Reynolds-Stress Turbulence Closure," J. Flu. Mech., Vol. 68, Pt. 3, pp. 537-566, 1975.

20. Hanjalic', K. and Launder, B.E., "A Reynolds Stress Model of Turbulence and its Application to Thin Shear Flows," J. Flu. Mech. Vol. 52, pp. 609-638, 1972.

21. Launder, B.E. and Spalding, D.B., Lectures in Mathematical Models of Turbulence, Academic Press, London, 1972.

22. Patankar, S.V. and Spalding, D.B., Heat and Mass Transfer in Boundary Layers, Second Ed., Intertext, London, 1970.

23. Manhardt, P.D., Orzechowski, J.A., and Baker, A.J., "COMOC II: Two-Dimensional Aerodynamics Sequence, Computer Program User's Guide," NASA CR-145165, 1977.

24. Strang, G., Fix, G.J., An Analysis of the Finite Element Method, Prentice Hall, New Jersey, 1973.

25. Shames, Irving H., Mechanics of Fluids, McGraw Hill, New York, 1962.

26. Proceedings, AFOSR-IFP-Stanford Conference on Computation of Turbulent Boundary Layers - 1968, Vol. I., Eds. S.J. Kline, G. Sovran, M.V. Morkovan, D.J. Cockrell, Vol. II, Eds. D.A. Coles, E.A. Hirst, pub. by Thermosciences Div., Dept. Mech. Engr., Stanford University 1969.

27. Smith, A.M.O., and Cebeci, T., "Remarks on Methods for Predicting Viscous Drag," AGARD-CP-124, 1973.

28. Preston, J.H. and Sweeting, N.E.,"The Experimental Determination of the Boundary Layer and Wake Characteristics of A Simple Joukowski Airfoil With Particular Reference to the Trailing Edge Region," Reports and Memoranda No. 1998, N.P.L., 1943

29. Goradia, S.H., and Lilley, D.E., "Theoretical and Experimental Study of A New Method for Prediction of Profile Drag of Airfoil Sections," NASA CR-2539, 1975.